Thèse de doctorat de l'Université DE STRASBOURG

Role of surfaces in magnetization dynamics and spin polarized transport: a spin wave study

Mohammad HAIDAR

Institut de Physique et Chimie des Matériaux de Strasbourg

Institut de Physique et Chimie des Matériaux de Strasbourg

Thèse de doctorat de l'Université DE STRASBOURG

Role of surfaces in magnetization dynamics and spin polarized transport: a spin wave study

par

MOHAMMAD HAIDAR

Soutenue publiquement le 16 Novembre 2012 devant le jury composé de :

Matthieu Bailleul	Directeur de thèse
Dirk Grundler	Examinateur
Ursula Ebels	Rapporteur
Michel Hehn	Rapporteur
Bernard Doudin	Président, rapporteur interne

To my parents
To my sisters
To my brothers

Acknowledgements

"A dream that becomes reality"

It is with great sense of honor and modesty I take this blessed moment to present this thesis, which is the outcome of exhaustive efforts made day and night over the past three years, for publishment. This thesis which would not have been possible without the enormous contributions of so many people to whom I hereby express my sincere regards for their great support and encouragement.

Foremost, I would like to extend my gratitude to Matthieu Bailleul for his great leadership, constructive daily discussions, recommendations, confidence and the unlimited support. I consider myself fortunate to have the opportunity to work with. Thank you so much for offering me this important subject and sharing with me your immense knowledge. Apart from the scientific guidance, I thank him for his embracement and help during my whole stay in Strasbourg, especially his contribution in learning the French language. Really, it was a great pleasure working under his supervision.

I would like to grab the opportunity here to pay my regards to Pierre Panissod who was my official supervisor for the first two years.

I am also very grateful to the members of the jury: Ursula Ebels, Michel Hehn and Dirk Grundler for reviewing and commenting on this manuscript. Special thanks to the president of the jury Bernard Doudin who was also my lecturer during the Masters degree where I have learnt the basics of the spin polarized transport in his spintronic course.

I take pride in recognizing support of all my colleagues in the DEMONS department. For me, it has been a rewarding and enlightening experience to work with all of them. In particular, I would like to thank Yves Henry for his significant advices, enthusiasm and willingness to assist. I would like also to thank Alain Carvalho for his assistance and dedication to work during the sample fabrication process and his valuable feedback in the e-beam lithography. I want also to recognize efforts and valuable contribution of Hicham Majjad and Sabine Siegwald in the clean room. Thanks also go to David Halley for his help in the X-ray diffraction measurements, and to Corinne Ulhaq-Bouillet for the nice TEM images. I also salute the commitment, admire the efforts and respect the dedication of all the technical staff at IPCMS. Thanks for your professional contribution which was honestly an added value to my thesis.

Special thanks to be addressed to Frédéric Ott for his gentle hospitality during my visit to the Laboratoire Leon Brillouin (LLB) and to Mikhail Kostylev for his great assistance in the micromagnetic simulation.

Thanks to Silviu Colis, Cécile Jollet and Sami Boukari. I have really enjoyed doing my teaching mission with them.

I will profit to express my appreciation and gratitude to my professors:

Haitham Zaraket from the Lebanese University and Joerg Baschnagel from Université de Strasbourg for their unforgettable lectures.

A word to say is that the strength and authenticity of this thesis would not have been in its current shape without the contribution of all of the above mentioned whom I find myself humbled by depth of their knowledge, practical experience and professional achievements.

From personal perspective, the most valuable experiences are associated with the people one gets to meet. Thanks to all my friends for the unforgettable moments we spent together in Strasburg: Jawad Ismael, Hassan Kesserwan, Ali Hallal, Fatima Ibrahim, Ali Jafaar, Mouhammad Mokadam, Mohamad Hamieh, Saber Gueddida, Wassim Jabber, Waked Srour, Iman Abdallah and Hakam Agha. I would like also to thank all my mates from IPCMS whom I will miss for sure.

Last but not least, I am deeply and forever indebted to my family for their love, support and encouragement throughout my entire life. Warm thanks to my parents Jamal and Ghada, my brothers Ali and Hussien, and my sisters Mona and Fatima. You were always the source of great inspiration and motivation to me. No words can convey my feelings and thoughts for their contributions. This thesis is dedicated for them.

To the new adventure...

Mohammad HAIDAR
STRASBOURG, 2012.

Contents

Introduction

The emergence of the electron spin in data storage devices has opened the door for a new generation of high technology applications. Although the spin of the electron is known for long time, it had not been used intensively to carry the information, until the discovery of the Giant magnetoresistance (GMR) in 1988. The GMR effect shows the interdependence between the magnetization configuration of the layers and the current. The industry interest for spintronics emerged when GMR heterostrucutres sensors have appeared in the read head of hard disc drives [20]. In parallel, the spin transfer torque (STT) phenomenon was discovered as a promising tool to manipulate the magnetization orientation of a magnetic layer with a DC current. The STT phenomenon was observed in a series of experiments: in current induced switching of the magnetization [1] [66], in spin transfer torque nano-oscillators [48][107], in current induced magnetic domain wall motion [116], and recently, in the current induced spin wave Doppler shift experiment [111].
J. Katine from Hitachi Global Storage Labs and E. Fullerton from Center of Magnetic Recording Research [91] have declared that the new generation of the magnetic memories will be based on the spin-torque devices in the near future. With this very fast multiplication of spintronics devices, a fundamental understanding of the spin polarized transport is required. The basic physics of spintronics is known since the beginning of the last century. Its cornerstone is the "two current model" proposed by Mott [79]. In this model, the majority and the minority electrons in ferromagnetic metals (Fe, Co, Ni) exhibit different conduction properties. Various sources of electron scattering (phonons, impurities [19], surfaces, grain boundaries [68]...) are likely to contribute to the resistivity of each band. A number of studies were carried out in the 1970's to describe the dominant scattering mechanism and to identify their contribution in each band. These studies consisted of resistivity measurements in binary and ternary alloys at different temperatures, which provide one indirectly with the spin-dependent resistivities associated to the impurities and to the phonons. However at the nanometer scale the surfaces are expected to play the major role in determining the characteristics of devices [85]. So far, the impact of the surface scattering on the spin polarized transport could not be addressed except in some GMR studies where the presence of several metal layers complicate the picture. The main difficulty was the lack of a suitable experiment to access directly the degree of spin polarization which measures the asymmetry between the current carried by the spin up and the spin down channels.
Recently, a new method based on the current induced spin wave Doppler shift [111], has been proposed by our group to measure directly the degree of the spin polarization of the electrical current in ferromagnetic thin films.

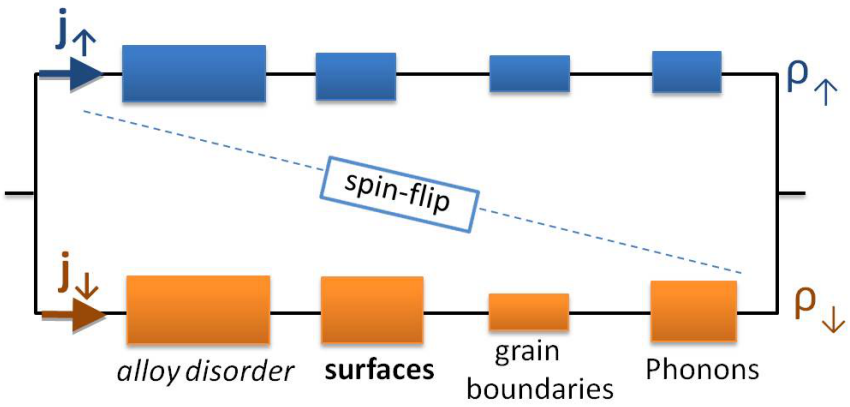

Figure 1: A possible scenario to describe the spin polarized transport in a ferromagnetic metal thin film.

Restoring to this new technique, we decided to probe the transport properties in ferromagnetic alloy thin films. The scenario we believe to account for the spin polarized transport in a ferromagnetic metal thin film is sketched in the figure-C.1 in the frame of an electrical circuit model. This scenario is based on the two current model and it considers that the electrons of each single channel are scattered by different sources including the impurities (alloy disorder), the phonons, the surfaces, and the grain boundaries. In this scenario spin flip processes are also possible (due to magnons or other sources) between the two channels. As a first step to validate / invalidate this scenario, a film thickness dependence study was performed in the frame of this thesis work in order to understand the role of the surfaces in the spin dependent transport and to identify the contribution of the surface scattering to the spin up and spin down resistivities.

This manuscript is divided into five chapters whose content is as follows:

In the first chapter, the general theoretical background describing the magnetization dynamics (uniform oscillations and spin waves) in ferromagnetic thin films is discussed. In addition a picture of the magnetization relaxation processes including recent works is presented.

In the second chapter, some basics of the spin polarized transport are presented. Three main parts are discussed there: the spin polarized transport, the surface scattering, and the spin transfer torque phenomena.

In the third chapter we start to discuss the experimental results. This chapter describes structural, electrical, and magnetic (static and dynamic) characterization of the permalloy thin films used for the spin wave studies.

In the fourth chapter, we discuss the propagating spin wave spectroscopy (PSWS) measurements in the absence of the DC current. The results of this

chapter are original in the sense that it is the first thickness dependence study performed for the propagating spin waves (typically such studies are performed on a single film thickness). The reflection signals of the PSWS are interpreted to provide us with the magnetic parameters which can be compared to those obtained by other characterization methods. The transmission signals are analyzed to understand qualitatively the spin wave propagation in the microstructures. At the end of this chapter, we discuss the non-reciprocity character of the magnetostatic surface waves.

In the fifth chapter, we present the results of the film thickness dependence of the current induced spin wave Doppler shift. These results are discussed within the two current model including surface electron scattering.

Chapter 1

Spin dynamics

This chapter describes the magnetization dynamics in ferromagnetic materials. It provides the theoretical background for the coming discussion in the next chapters. The discussion is focused on the uniform magnetic excitation ($k = 0$), i.e. the ferromagnetic resonance (FMR) and on the non-uniform excitation ($k \neq 0$), i.e. the spin waves, which are of particular interest in this thesis. At the end of the chapter, an overview for the magnetization relaxation in metallic ferromagnets is presented.

1.1 Ferromagnetism

In ferromagnets the magnetic moments are spontaneously aligned parallel to each other below a critical temperature, even in the absence of an external field. In 1907 Pierre Weiss attributed this spontaneous behavior to an internal molecular field which is strong enough to conserve a parallel alignment of the moments against the thermal fluctuations. Before starting the discussion of the dynamics in ferromagnets, we will describe the magnetic free energy of an ordered magnetic crystal.

1.1.1 Energy formulation

Consider a ferromagnetic sample placed in an external magnetic field H_{ext}, the magnetic moment will experience an effective field H_{eff}, defined as:

$$H_{eff} = -\frac{1}{\mu_0}\frac{\delta\varepsilon_{tot}}{\delta M}, \tag{1.1}$$

where the total magnetic energy ε_{tot} is a functional of $\overrightarrow{M}(r)$ defined as $\overrightarrow{M}(r) = M_s.\overrightarrow{m}(r)$ with $|| \overrightarrow{m} || = 1$, described as a sum of the different energies acting in the ferromagnet

$$\varepsilon_{tot} = \varepsilon_{zee} + \varepsilon_{dem} + \varepsilon_K + \varepsilon_{ex}. \tag{1.2}$$

ε_{zee} corresponds to the Zeeman interaction, ε_{dem} is the demagnetizing energy, ε_K is the energy of the anisotropy interaction and ε_{ex} is the exchange energy. The expression of the energy for each of these interactions is given below.

- **Zeeman energy**
  As a magnetic sample is placed in an external magnetic field H_{ext}, the magnetic moments favor a parallel alignment to H_{ext}. The Zeeman energy is expressed as [16]:

$$\varepsilon_{zee} = -\mu_0 \int \overrightarrow{H}_{ext}.\overrightarrow{M}dV. \tag{1.3}$$

- **Demagnetizing energy**
  When a magnetic field is applied to the sample the aligned magnetic moments will interact with each other via the dipole-dipole interaction. Magnetic poles are generated on the boundaries of the sample, which creates a demagnetizing field H_d opposite to the direction of the external field. The demagnetizing field depends on the distribution of the poles over the sample boundaries. It is expressed as

$$H_d = -\mu_0[N].\overrightarrow{M},$$

  with $[N]$ is a 3×3 dimensionless tensor, whose trace is equal to unity,

$$N_{xx} + N_{yy} + N_{zz} = 1.$$

  The energy associated with the demagnetizing field is called the demagnetizing energy, the magnetostatic energy, or the dipolar energy. It is written as:

$$\varepsilon_{dem} = -\frac{\mu_0}{2} \int_{sample} \overrightarrow{M}.\overrightarrow{H_d}dV. \tag{1.4}$$

  Of particular importance throughout this thesis is the case of thin films with the z-axis oriented perpendicular to the film plane, then the demagnetizing coefficients are ($N_{xx} = 0$, $N_{yy} = 0$, $N_{zz} = 1$). The associated demagnetizing energy in such films is written as:

$$\varepsilon_{dem} = +\frac{\mu_0 V}{2}(\overrightarrow{e}_z.\overrightarrow{M})^2. \tag{1.5}$$

- **Anisotropy energy**
  The magnetocrystalline anisotropy describes the dependence of the magnetic energy on the relative orientation between the magnetization and the crystal lattice. This dependence arises from the spin-orbit interaction, where the spin moments are coupled to the lattice via the orbital motion of the electrons. In an anisotropic lattice, the lattice is easily magnetized along a preferable crystallographical direction. This is known as a uniaxial anisotropy. The associated volume energy density is:

$$e_K = K_u sin^2\theta,$$

  where K_u is in J/m^3 and θ is the angle between the magnetization vector and the preferred crystallographical direction.
  Depending on the sign of K_u, the uniaxial direction will be either an easy axis for $K_u > 0$, or a hard axis for $K_u < 0$.

At the surface of the film, the reduced symmetry of the atomic orbital produces a surface anisotropy for the magnetization. The surface anisotropy energy density is defined as a function of the angle θ between the surface magnetization and the normal [49]:

$$e_s = -K_s \cos^2 \theta,$$

where K_s is in J/m^2. For $K_s > 0$ the normal of the surface is an easy axis.

1.2 Magnetization dynamics

The response of the magnetic moments to an external magnetic excitation such as a weak alternating field in the microwave range (several GHz) is obtained by solving the Landau-Lifshitz equation of motion. In this section, we will first describe the solution of the LL equation in a non-dissipative medium. Second, the effects of the anisotropy (shape, and surface anisotropy) on the uniform resonance will be considered.

1.2.1 Equation of motion of the magnetization

In a ferromagnetic material, the microscopic exchange interaction forces the spins of the system to be well aligned. A weak microwave excitation of the ferromagnet drives the magnetic moments away from their equilibrium position, but the spins remain aligned parallel over a small region. Accordingly, the magnetic moments in a continuum approximation are described with a classical magnetization vector ($\overrightarrow{M}$). In the presence of a static external magnetic field, the magnetization vector precesses around an effective field (H_{eff}) with a cone angle θ as shown in figure-1.1a. The equation of motion governing the precession is written [42]:

$$\frac{\partial \overrightarrow{M}}{\partial t} = -\gamma \mu_0 \overrightarrow{M} \times \overrightarrow{H}_{eff}, \tag{1.6}$$

where γ is the gyromagnetic ratio and μ_0 is the permeability of the vacuum. This is known as the Landau-Lifshitz (LL) equation. It relates the rate change of the magnetization to the torque exerted by the effective field H_{eff} on the magnetization.
In the equation of motion (1.6) the magnitude of the magnetization vector is conserved:

$$\frac{\partial}{\partial t} \overrightarrow{M}^2 = 0, \tag{1.7}$$

which indicates that the magnetization vector precesses on the surface of a sphere.

1.2.1.1 Solution of the equation of motion

Consider a ferromagnetic sample in a static magnetic field directed along the z-axis. The equilibrium magnetization is oriented parallel to the magnetic field. Assume that, the sample is excited by an alternating microwave field $\overrightarrow{h}(t)$ oriented along the xy plane. In ferromagnetic resonance experiments we assume

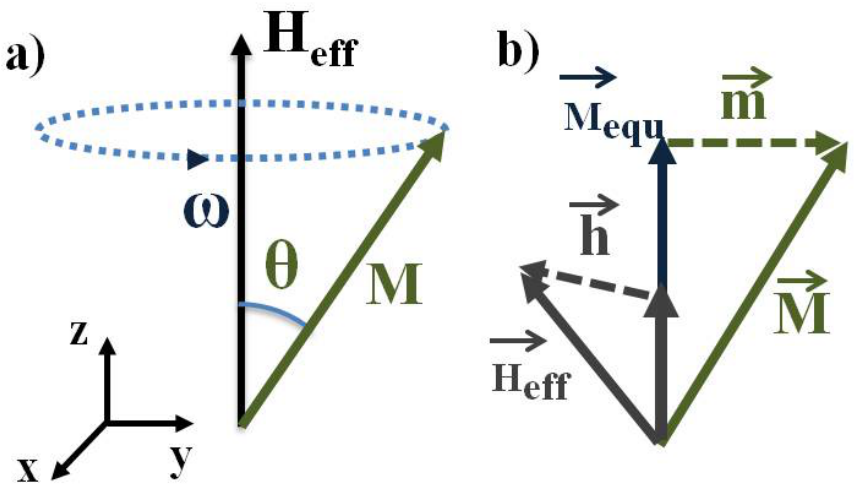

Figure 1.1: a) Sketch of the precession of the magnetization around an effective field oriented along the z-axis. The magnetization rotates in an anticlockwise direction. b) Notations and coordinates describing the magnetization and the field in the linearized LL-equation

the dynamical components of the field $\overrightarrow{h}(t)$ and the magnetization $\overrightarrow{m}(t)$ are very small compared to the static components. We write $\overrightarrow{H}$ and $\overrightarrow{M}$ as:

$$\overrightarrow{H} = \overrightarrow{H}_0 + \overrightarrow{h}(t) \qquad \overrightarrow{M} = \overrightarrow{M}_0 + \overrightarrow{m}(t).$$

Let us define the dynamical susceptibility $\bar{\chi}$ as the response of the dynamical magnetization $\overrightarrow{m}(t)$ at a given point to the microwave field at the same point:

$$\overrightarrow{m} = \bar{\chi}\,\overrightarrow{h}\,. \tag{1.8}$$

The susceptibility $\bar{\chi}$ is the 2×2 Polder tensor. To derive the Polder tensor $[\bar{\chi}]$, one should solve the LL-equation. First, the equation of motion-1.6 is written as follows:

$$\frac{\partial \overrightarrow{m}}{\partial t} = -\gamma\mu_0[\overrightarrow{M}_0 \times \overrightarrow{H}_0 + (\overrightarrow{m} \times \overrightarrow{H}_0) + (\overrightarrow{M}_0 \times \overrightarrow{h}) + \overrightarrow{m} \times \overrightarrow{h}]. \tag{1.9}$$

$\overrightarrow{M}_0 \times \overrightarrow{H}_0$ term is zero since the magnetization is aligned parallel to the applied static field. To the first order approximation, the product of the alternating parts $\overrightarrow{m} \times \overrightarrow{h}$ is neglected. Then the linearized equation (1.9) becomes:

$$\frac{\partial \overrightarrow{m}}{\partial t} = -\gamma\mu_0[\overrightarrow{m} \times \overrightarrow{H}_0 + \overrightarrow{M}_0 \times \overrightarrow{h}]. \tag{1.10}$$

Projecting equation-1.10 along the coordinates axes shown in figure-1.1b and assuming the time dependent oscillation is of the form $e^{i\omega t}$, the linearized equation is written as:

$$-i\omega\overrightarrow{m} = \hat{z} \times \left[+\omega_M \overrightarrow{h} - \omega_0 \overrightarrow{m}\right], \tag{1.11}$$

where we define $\omega_M = \gamma\mu_0 M_s$, and $\omega_0 = \gamma\mu_0 H_0$.
Solving the system of equation, and expressing h_x and h_y in terms of m_x and m_y, one obtains:

$$\begin{pmatrix} \mathbf{h_x} \\ \mathbf{h_y} \end{pmatrix} = \frac{1}{\omega_M} \begin{pmatrix} \omega_0 & i\omega \\ -i\omega & \omega_0 \end{pmatrix} \begin{pmatrix} \mathbf{m_x} \\ \mathbf{m_y} \end{pmatrix}. \tag{1.12}$$

Equation (1.12) is of the form $h = \chi^{-1} m$. To obtain the Polder susceptibility tensor, one should calculate the inverse of the matrix in equation (1.12)

$$\bar{\chi} = \begin{pmatrix} \chi & i\kappa \\ -i\kappa & \chi \end{pmatrix}, \tag{1.13}$$

with

$$\chi = \frac{\omega_0 \omega_M}{\omega_0^2 - \omega^2}, \qquad \kappa = \frac{\omega \omega_M}{\omega_0^2 - \omega^2}. \tag{1.14}$$

The Polder tensor is a non-diagonal and an antisymmetric tensor. The microwave field will not only produce a component of the dynamical magnetization parallel to it but also a perpendicular component with a $\pi/2$ shift. As ω approaches γH the components of Polder tensor diverge. It corresponds to the resonance condition of the sample in an unbounded medium. In a finite sample, the resonance frequency depends also on the sample geometry as we will discuss in the section-1.2.2.

1.2.2 Ferromagnetic resonance

1.2.2.1 Ferromagnetic resonance in an ellipsoid

In the previous section, the susceptibility tensor was derived assuming that the field is known at a given point. This assumption is oversimplified since the dipolar field depends on the distribution of the magnetization over the entire sample. In this section, we will solve the LL equation in an ellipsoid geometry, where the magnetization has a uniform distribution. The static directions of the field and of the magnetization are oriented along the z-axis. The same notation as in the section 1.2.1.1 is used for the magnetic field and the magnetization coordinates,

$$\overrightarrow{H} = \begin{pmatrix} h_x(t) \\ h_y(t) \\ H_z \end{pmatrix}, \qquad \overrightarrow{M} = \begin{pmatrix} m_x(t) \\ m_y(t) \\ M_z \end{pmatrix}. \tag{1.15}$$

The demagnetizing field arises from the accumulation of the poles on the surfaces of the ellipsoid. The axes of the ellipse coincides with the coordinate axes as shown in figure-1.2. Then the tensor $[N]$ will be symmetric and diagonal. The demagnetizing field H_d of an ellipsoid is expressed as:

$$H_{dem} = -\begin{pmatrix} N_{xx} & 0 & 0 \\ 0 & N_{yy} & 0 \\ 0 & 0 & N_{zz} \end{pmatrix} \begin{pmatrix} m_x \\ m_y \\ M_z \end{pmatrix}. \tag{1.16}$$

Then the effective field is the sum of the external and the demagnetizing fields:

$$H_{eff} = \begin{pmatrix} h_x - N_{xx} m_x \\ h_y - N_{yy} m_y \\ H_z - N_{zz} M_z \end{pmatrix}. \tag{1.17}$$

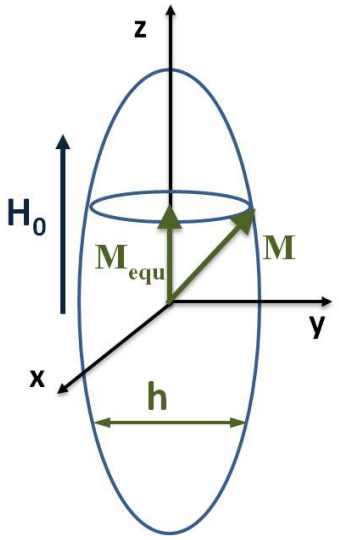

Figure 1.2: The system of coordinates used for describing the uniform resonance of an ellipsoid

Under the action of the effective field the LL equation is solved following the same procedure as in the last section-1.2.1.1 to derive the susceptibility. One obtains:

$$\overrightarrow{h} = \chi^{-1}\overrightarrow{m} = \frac{1}{w_M}\begin{pmatrix} \omega_x & i\omega \\ -i\omega & \omega_y \end{pmatrix}\overrightarrow{m}, \tag{1.18}$$

where ω_x and ω_y are defined as:

$$\omega_x = \omega_0 + N_{xx}\omega_M, \qquad \omega_y = \omega_0 + N_{yy}\omega_M.$$

One could deduce the resonance frequency by solving $det(\chi^{-1}) = 0$, which gives: $\omega_{res} = \sqrt{\omega_x\omega_y}$, or [42]:

$$\omega_{res} = \gamma\{[H_0 + (N_{xx} - N_{zz})M_0][H_0 + (N_{yy} - N_{zz})M_0]\}^{\frac{1}{2}}. \tag{1.19}$$

It is clear that the resonance frequency depends on the geometry of the sample through the demagnetizing factor. The equation (1.19) is known as the Kittel formula. Although the Kittel formula is derived for samples with an ellipsoidal shape it is also applied to other geometries with a uniform magnetization. Figure-1.3 shows magnetic field dependence of the resonance frequency for two particular cases of ellipsoid (film and sphere).

1.2.2.2 Including surface anisotropy

In this section, the LL equation is solved for a thin film in the presence of surface anisotropy. This is done using an alternative method known as Smit-Beljers formalism. In this formalism, the resonance frequency is derived from the total energy ε of the sample.

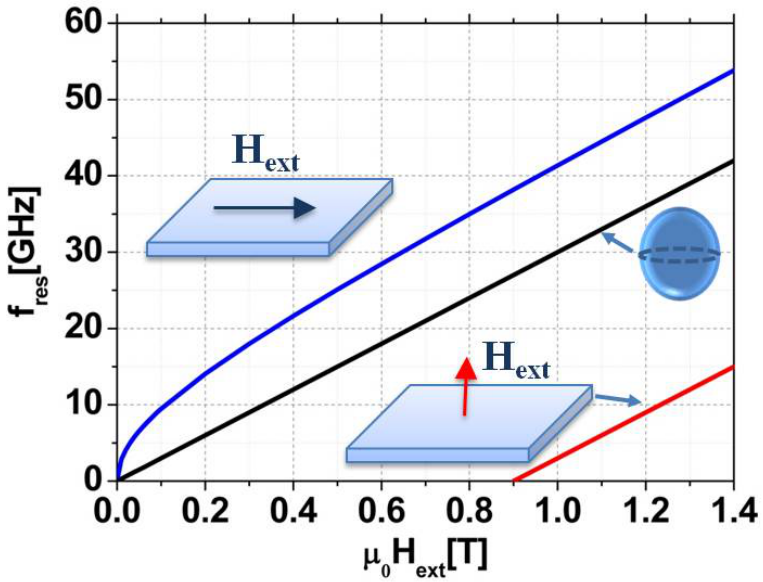

Figure 1.3: The dispersion relation for a thin film normally and tangentially magnetized, and for a sphere. ($\mu_0 M_0$=0.9 T and $\gamma/2\pi$=29 GHz/T).

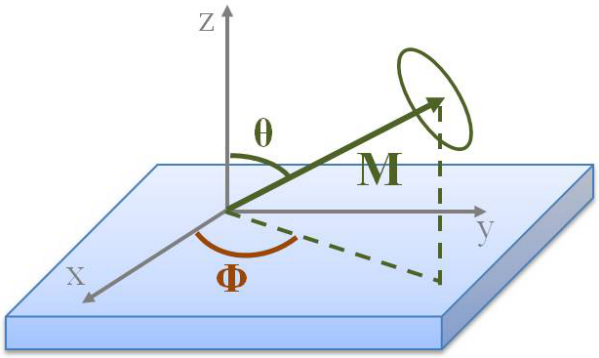

Figure 1.4: The geometry of the magnetization $\vec{M}$ in the cartesian coordinate axis xyz. θ is the angle between the magnetization and z-axis, ϕ is the projection angle of $\vec{M}$ on the xy-plane.

In this formalism spherical coordinate representation are used to express the equation of motion (1.6) as shown in the figure-1.4. In such coordinates the equation of motion of the magnetization writes:

$$\left\{ \begin{array}{lcl} \frac{\delta\phi}{\delta t} & = & -\frac{\gamma}{M\sin\theta}\frac{\delta\varepsilon}{\delta\theta} \\ \frac{\delta\theta}{\delta t} & = & \frac{\gamma}{M\sin\theta}\frac{\delta\varepsilon}{\delta\phi} \end{array} \right. \tag{1.20}$$

The equilibrium position of the magnetization is obtained when the free energy is minimum,

$$(\frac{\delta\varepsilon}{\delta\theta})_{\theta=\theta_0,\phi=\phi_0} = 0; \qquad (\frac{\delta\varepsilon}{\delta\phi})_{\theta=\theta_0,\phi=\phi_0} = 0 \tag{1.21}$$

where the angles θ_0 and ϕ_0 represent the equilibrium orientation of the magnetization. Assuming a small deviation of the magnetization from the equilibrium position, and solving the system of equation-1.20 one can derive the resonance frequency as [42]:

$$\omega^2 = \frac{\gamma^2}{(M\sin\theta)^2}(F_{\phi\phi}F_{\theta\theta} - F_{\phi\theta}^2), \tag{1.22}$$

where F_{ij} are the second derivatives of the energy with respect to the angles. This general condition is known as the Smit-Beljers formula. The resonance frequency is related to the curvature of the total energy evaluated at its minimum. Let us consider the case of a thin film, where the total free energy is the sum of the Zeeman, the dipolar, and the surface anisotropy energies. Writing each term in its spherical representation, one obtains the total energy as:

$$\begin{array}{rcl} \varepsilon & = & \underbrace{\frac{1}{2}\mu_0 M_s^2\cos^2\theta St}_{dipolar field} - \underbrace{K_s\cos^2\theta S}_{surface anisotropy} - \underbrace{\mu_0 M_s H_e[\cos\theta\cos\theta_H + \sin\theta\sin\theta_H\cos(\phi-\phi_H)]St}_{Zeeman interaction} \\ \varepsilon & = & \frac{1}{2}\mu_0 M_s\cos^2\theta St M_{eff} - \mu_0 M_s H_e[\cos\theta\cos\theta_H + \sin\theta\sin\theta_H\cos(\phi-\phi_H)]St \end{array} \tag{1.23}$$

where S and t are the surface and the thickness of the film respectively, and the effective magnetization M_{eff} is defined as

$$M_{eff} = M_s - H_K. \tag{1.24}$$

H_k is the anisotropy field which writes:

$$H_K = \frac{2K_s}{\mu_0 M_s t}. \tag{1.25}$$

The resonance formula allows us to derive the resonance frequency for an arbitrary angle of the anisotropy direction. Let us consider a case where the equilibrium magnetization is in the plane, the equilibrium angles are:

$$\phi = \phi_0 = 0, \qquad \theta = \theta_0 = \frac{\pi}{2}.$$

Evaluating the equation 1.22 at θ_0 and ϕ_0 one obtains the resonance frequency as:

$$\omega_{res} = \gamma\mu_0\sqrt{(H_0 + M_{eff})H_0}. \tag{1.26}$$

The surface anisotropy appears in the resonance frequency to modify the saturation magnetization of the film. From equations-1.24, 1.25, it is clear that we can have an access to the saturation magnetization and to the surface anisotropy by following the effective magnetization as a function of the film thickness. This will be used in the experimental part.

1.3 Spin waves

In 1930's Bloch introduced the concept of the low energy excitations in a ferromagnetic materials, the spin waves. These excitations are explained as slight deviations of the spins away from their parallel orientation. In contrast to the uniform precession already mentioned in section-1.2.2 where all the spins are precessing at the same frequency and the same phase, the spin waves are non-uniform excitations in which the spins are oscillating at the same frequency but with different phases as shown in figure-1.5. In this thesis our concern is focused

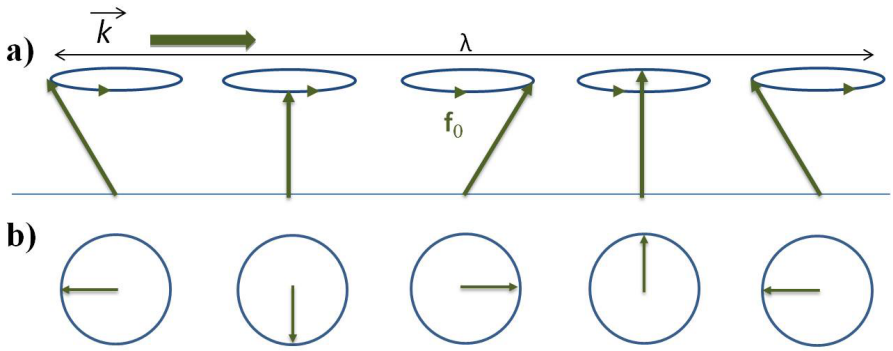

Figure 1.5: a) Sketch of a propagating spin wave with a frequency f_0 and a wavevector k. b) a top view of the wave showing the phase shift between the spins

on the spin waves propagating in the magnetostatic regime. In this regime the coupling between the spins is due to the dipolar interaction rather than the exchange interaction since the spin waves are propagating with a wavelength λ much greater than the exchange length l_{ex}. In the magnetostatic regime the coupling between the electrical and the magnetic field is neglected and the Maxwell equation is written as:

$$\begin{cases} \vec{\nabla} \times \vec{h} &= 0, \\ \vec{\nabla} \cdot \vec{b} &= 0, \end{cases} \tag{1.27}$$

where $\vec{h}$ is the magnetic field, and $\vec{b} = (1 + \bar{\chi})\vec{h}$ is the magnetic induction. From the first equation of 1.27 one can write the magnetic field in terms of a scalar potential Ψ as $\vec{h} = -\vec{\nabla}\Psi$. Based on the equations of 1.27 one can derive the wave equation of the spatial part for the scalar potential as [100]:

$$(1+\chi)(\frac{\partial^2\Psi}{\partial x^2} + \frac{\partial^2\Psi}{\partial y^2}) + \frac{\partial^2\Psi}{\partial z^2} = 0, \tag{1.28}$$

This is the well known Walker equation. Imposing the electromagnetic boundary conditions one can solve the Walker equation (i.e solve for the scalar potential) to determine the dynamical magnetization profile (m) of the spin wave using:

$$\vec{m} = \chi\vec{h} = -\chi\vec{\nabla}\Psi.$$

In the next sections, we present the solution of the Walker equation and the dispersion relation in a bulk ferromagnet and in a thin film. In the case of thin films the scalar potential solution is determined for three different configurations of the spin waves.

1.3.1 In a bulk ferromagnet

The spatial symmetry of the bulk ferromagnet allows us to express the trial solution of the scalar potential in equation-1.28 in terms of a plane wave solution,

$$\Psi(\vec{r},t) = \Psi_0 e^{i(\omega t - \vec{k}.\vec{r})}.$$

Substituting the trial solution of Ψ in equation-(1.28), and considering that the wave is propagating with an angle θ with respect to the applied field H, one obtains:

$$\begin{cases} (1+\chi)(k_x^2+k_y^2)+k_z^2 &= 0 \\ \sin^2\theta = \frac{k_z^2}{k^2} \end{cases} \tag{1.29}$$

where $k = k_x^2 + k_y^2 + k_z^2$. Then the solution of equation (1.29) is written as:

$$\chi \sin^2\theta = -1. \tag{1.30}$$

By substituting χ from (1.14) in (1.30), one can derive the magnetostatic modes in a bulk ferromagnet which writes as [100]:

$$\omega = [\omega_0(\omega_0 + \omega_M \sin^2\theta)]^{\frac{1}{2}}. \tag{1.31}$$

One notices that the dispersion relation in (1.31) represents a frequency band which is independent of the wavevector k. This degeneracy is lifted when the boundary conditions are imposed as in the case of thin films or when the waves in the exchange-dipolar regime are considered.
The frequency of the modes are in the range $(\omega_0 \leq \omega \leq \sqrt{\omega_0(\omega_0+\omega_M)})$, where the lower and higher limits correspond to the frequencies of the waves propagating parallel and perpendicular to the applied field respectively.

1.3.2 Thin films

In this section, the characteristics of the magnetostatic waves are studied in a thin film with a finite thickness (t) bounded with dielectric materials. We solve the Walker equation-1.28 accounting for the electromagnetic boundary conditions. We will describe the solution obtained in the case of spin waves propagating in a normally and in a tangentially magnetized thin film as shown in the figure-1.6.

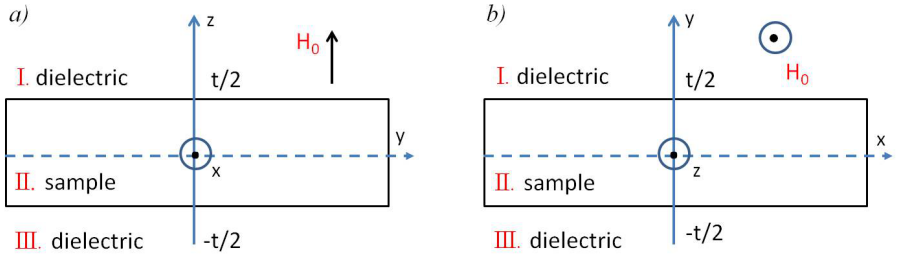

Figure 1.6: Sketch of the coordinate axis used for the cases of a normally magnetized film (a) and of a tangentially magnetized film (b).

1.3.3 Normally magnetized films

Assume that a static magnetic field is applied perpendicular to the film plane (z-axis) as shown in figure-1.6a. If this field is high enough to overcome the shape anisotropy ($H_0 > M_s$), the magnetization will align parallel to the film normal ($\overrightarrow{M} \parallel \overrightarrow{n}$). Assume, a spin wave propagates in the film plane with a wavevector $\overrightarrow{k}$ such as ($\overrightarrow{k} \perp \overrightarrow{n}$). A spin wave propagating in this geometry (($\overrightarrow{M} \parallel \overrightarrow{n}$) $\perp$ ($\overrightarrow{k}$)) is known as a magnetostatic forward volume waves (MSFVW). In the following, we derive the dispersion relation and the scalar potential for the MSFVW configuration.
Suppose the spin waves propagates with a wave vector $\overrightarrow{k}$

$$\overrightarrow{k} = \overrightarrow{k}_t \qquad \text{where} \qquad \overrightarrow{k}_t = \hat{x}k_x + \hat{y}k_y.$$

Since in the dielectric layers $\chi = 0$, Walker's equation reduces to a Laplace's equation ($\Delta\Psi = 0$). The solution of the scalar potential in the dielectric layers is written with the assumption that it vanishes at infinity as:

$$\begin{aligned} \Psi_I(r) &= Ae^{i\overrightarrow{k}_t.\overrightarrow{r}-k_t z}, \qquad z > t/2 \\ \Psi_{III}(r) &= Be^{i\overrightarrow{k}_t.\overrightarrow{r}+k_t z}, \qquad z < -t/2, \end{aligned} \tag{1.32}$$

where A, and B are constants to be determined later.
Inside the magnetic layer, the trial solutions of the Walker equation are expressed as an even or odd function respectively, they are of the form :

$$\begin{aligned} \Psi_{II}(r) &= \Psi_0 \cos(qz)e^{i\overrightarrow{k}_t.\overrightarrow{r}}, \qquad -t/2 < z < t/2 \\ \Psi_{II}(r) &= \Psi_0 \sin(qz)e^{i\overrightarrow{k}_t.\overrightarrow{r}}, \qquad -t/2 < z < t/2, \end{aligned} \tag{1.33}$$

where Ψ_0 is a constant which determines the amplitude of the mode and q is a quantity to be determined . Applying the boundary conditions at the interfaces of the magnetic and the dielectric layers and solving the system of equations, one can derive the dispersion relation of the (MSFVW) and obtain the constants A, B, Ψ_0. After a few steps of mathematical calculations, an implicit dispersion relation is obtained [100]:

$$\tan[\frac{k_t t}{2}\sqrt{-(1+\chi)} - \frac{n\pi}{2}] = \frac{1}{\sqrt{-(1+\chi)}}, \tag{1.34}$$

where n could be an even or odd integer. In the general case, for any mode of order n, the frequency spectrum is obtained by looking for a graphical solution of (1.34). Kalinikos derives an explicit dispersion relation of the frequency ω for the lowest order mode (n=0) which writes [54]:

$$\omega^2 = \omega_0[\omega_0 + \omega_M(1 - \frac{1 - e^{-k_t t}}{k_t t})]. \tag{1.35}$$

The solid red line in the figure-1.8 shows a plot for the dispersion relation of the MSFVW configuration. The frequency of the MSFVW depends on the film thickness t and on the magnitude of the wavevector k. It is independent on the direction of the wavevector, so the wave propagation is isotropic in the plane of the film. In contrary to the continuum frequency spectrum in the bulk, the frequency band is discrete in the MSFVW .
From the boundary conditions, One can find the constants (A, B) and q as:

$$A = B = \Psi_0 e^{k_t t/2}\cos(qt/2), \qquad q = k_t\sqrt{-(1+\chi)}. \tag{1.36}$$

The even solution of the scalar potential for the MSFVW is expressed as:

$$\begin{cases} \Psi_I(r) &= \Psi_0 e^{k_t t/2}\cos(k_t\sqrt{-(1+\chi)}t/2)e^{i\overrightarrow{k}_t.\overrightarrow{r}-k_t z} & z > t/2 \\ \Psi_{II}(r) &= \Psi_0\cos(k_t\sqrt{-(1+\chi)}z)e^{i\overrightarrow{k}_t.\overrightarrow{r}} & -t/2 < z < t/2 \\ \Psi_{III}(r) &= \Psi_0 e^{k_t t/2}\cos(k_t\sqrt{-(1+\chi)}t/2)e^{i\overrightarrow{k}_t.\overrightarrow{r}+k_t z} & z < -t/2. \end{cases} \tag{1.37}$$

Inside the magnetic layer the wave amplitude of the MSFVW signals is distributed sinusoidally over the volume of the film. The dynamical magnetization for the MSFVW are plotted in the figure-1.7a).
In this configuration, the group and the phase velocities are both in the same direction (v_g and $v_{ph} > 0$). Accordingly, these waves are called forward waves.

1.3.4 Tangentially magnetized films

In this section, we will consider the case of a tangentially magnetized film with ($\overrightarrow{M} \perp \overrightarrow{n}$). The Walker equation is solved in two cases: where the magnetization ($\overrightarrow{M}$) orientation is either parallel or perpendicular to the propagation direction ($\overrightarrow{k}$).

1.3.4.1 Magnetostatic backward volume wave

Here, we will discuss briefly the magnetostatic backward volume wave (MSBVW) configuration where the propagation direction is parallel to the magnetization direction ($\overrightarrow{k} \parallel \overrightarrow{M}$). Following the same procedure as in the section 1.3.3, one can obtain the dispersion relation for the even and odd modes solution as:

$$tan[\frac{k_z t}{2\sqrt{-(1+\chi)}} - \frac{(n-1)\pi}{2}] = \sqrt{-(1+\chi)}, \tag{1.38}$$

where n is an integer. An explicit dispersion relation is derived by Kalinikos for the lowest order mode (n=1):

$$\omega^2 = \omega_0[\omega_0 + \omega_M(\frac{1 - e^{-k_z t}}{k_z t})]. \tag{1.39}$$

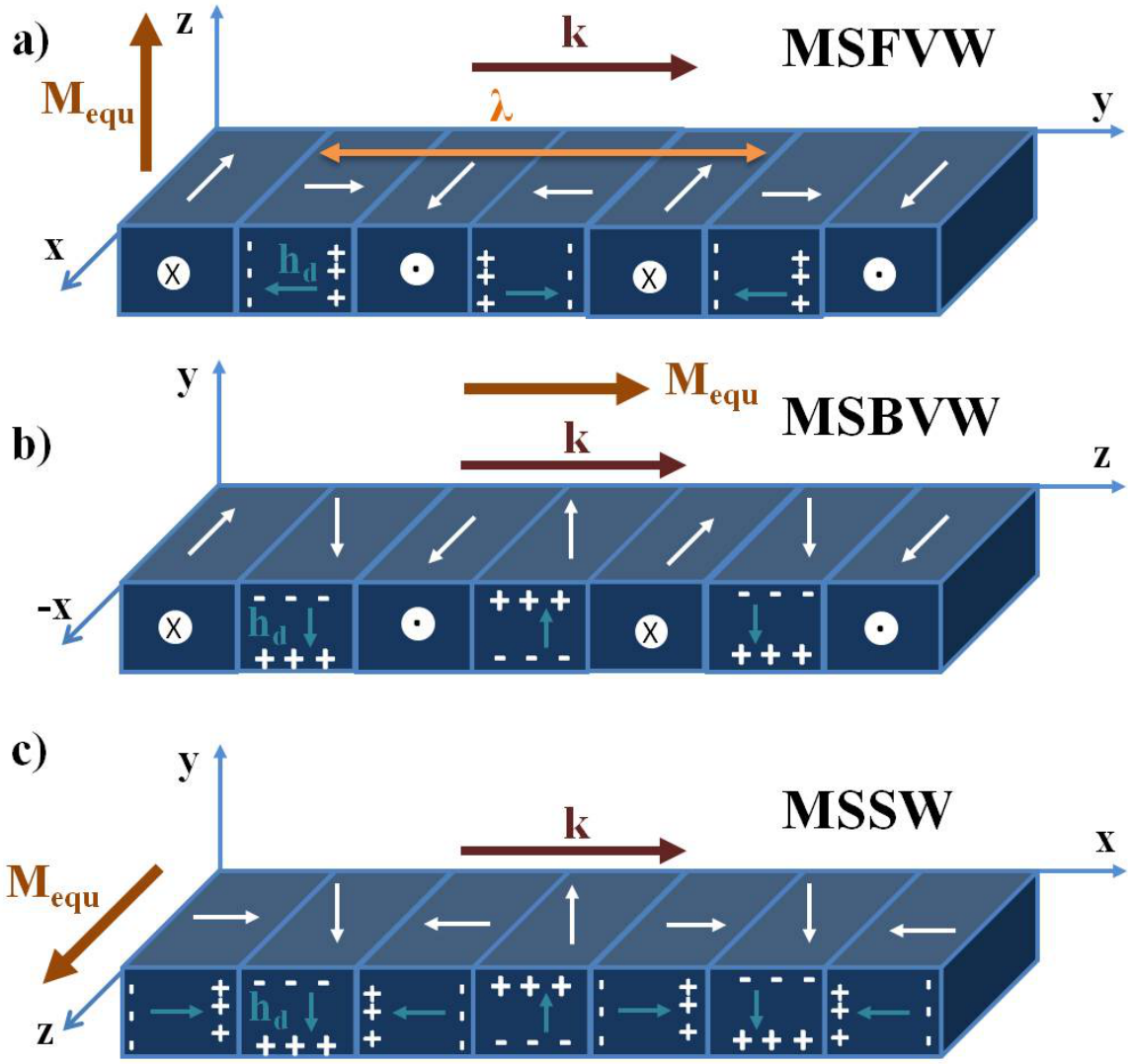

Figure 1.7: Sketch of a propagating spin wave with a wavevector k and with different orientations of the magnetic field. It corresponds to the configurations a) Magnetostatic forward volume wave, b) Magnetostatic backward volume wave c) Magnetostatic surface waves. In each sketch we plot the dynamical magnetization (white arrows) and the dipolar field (dark cyan arrows) over a quarter wavelength region.

The solid green line in the figure-1.8 shows a plot for the dispersion relation of the MSBVW. With few mathematical steps, one can write the scalar potential of the even modes as:

$$\begin{array}{rcll} \Psi_I(r) & = & \Psi_0 e^{k_z t/2}\cos(k_y t/2)e^{i\nu k_z.z-k_z.y} & y > t/2 \\ \Psi_{II}(r) & = & \Psi_0\cos(k_y y)e^{i\nu k_z z} & -t/2 < y < t/2 \\ \Psi_{III}(r) & = & \Psi_0 e^{k_z t/2}\cos(k_y t/2)e^{i\nu k_z.z+k_z.y} & z < -t/2 \end{array} \quad (1.40)$$

with $\nu = \pm 1$ indicates the propagation direction. The amplitude of the MSBVW in the magnetic layer is distributed sinusoidally over the thickness. Figure-1.7b shows the dynamical magnetization of this MSBVW configuration.
It is known as a backward volume wave since its group velocity is negative and it is opposite to its phase velocity.

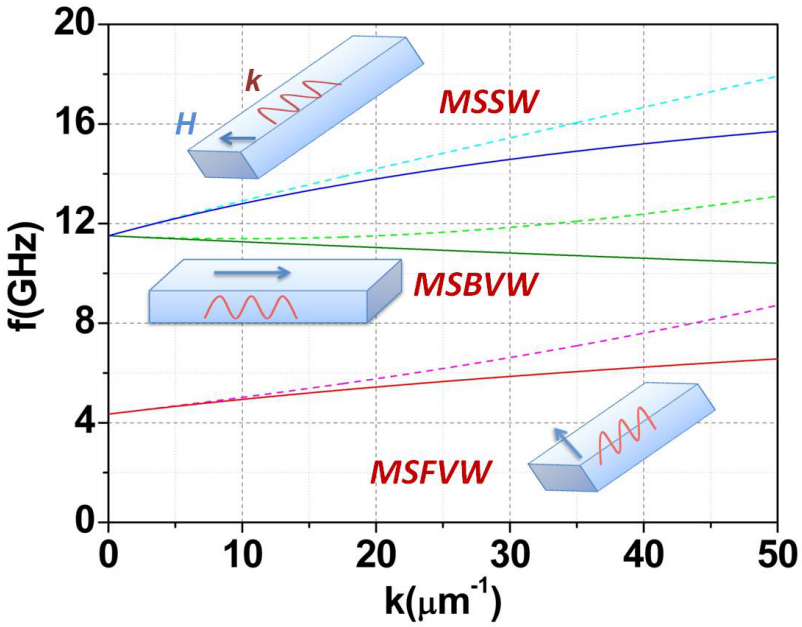

Figure 1.8: Plot of the dispersion relation in the magnetostatic regime (solid lines) and the exchange-dipolar regime (dotted line) for the three configurations: MSFVW, MSBVW, and MSSW. The film thickness is t =10nm, $\mu_0 M_s$=0.9T, and the other parameters are $\gamma/2\pi$ =29 GHz/T. In the case of the MSSW and MSBVW the field is $\mu_0 H_0$=0.15T, and in the case of the MSFVW the total applied field is $\mu_0 H_0$=1.05T.

1.3.4.2 Magnetostatic surface waves

Consider a thin film magnetized in-plane along the z-axis and a wave propagating along the x-axis with a wave vector k, such that $(\overrightarrow{k} \perp \overrightarrow{M})$ as shown in fig-1.6b. This configuration where $((\overrightarrow{k} \perp \overrightarrow{M}) \perp \overrightarrow{n})$ is known as magnetostatic

surface spin waves (MSSW) or Damon-Esbach modes [26].
Now, we will solve the Walker equation (1.28) in the MSSW configuration to obtain the dispersion relation and the scalar potential of this mode.
As mentioned previously, the Walker equation (1.28) reduces to Laplace's equation in the dielectric medium. Then the scalar potential reads:

$$\begin{array}{rcll} \Psi_I(\overrightarrow{r}) & = & Ce^{-ik_y y+i\nu k_x x} & z > t/2 \\ \Psi_{III}(\overrightarrow{r}) & = & De^{ik_x y+i\nu k_x x} & z < -t/2 \end{array} \tag{1.41}$$

where C, D are constant, and $\nu = \pm 1$ corresponds to the propagation direction. Substituting the scalar potential into the Laplace's equation one obtains:

$$(k_x^2 + k_y^2) = 0. \tag{1.42}$$

The solution of this equation provides us with the condition $k_y = ik_x$. Then the scalar potential becomes:

$$\begin{array}{rcll} \Psi_I(\overrightarrow{r}) & = & Ce^{-ky+i\nu kx} & z > t/2 \\ \Psi_{III}(\overrightarrow{r}) & = & De^{ky+i\nu kx} & z < -t/2 \end{array} \tag{1.43}$$

where $k = k_x$. Inside the magnetic layer, there exists a hyperbolic solution to the Walker equation (1.28) it writes:

$$\Psi_{II}(\overrightarrow{r}) = e^{i\nu kx}[\Psi_{0+}e^{ky} + \Psi_{0-}e^{-ky}] \tag{1.44}$$

Note that the scalar potential in MSSW consists of a propagating part along the x-axis and an evanescent profile over the y-axis. By solving explicitly the boundary conditions on the two surfaces

$$\left\{ \begin{array}{ccc} \Psi_I(t/2) & = & \Psi_{II}(t/2) \\ \Psi_{III}(-t/2) & = & \Psi_{II}(-t/2) \\ (1+\chi)\frac{\partial \Psi_{II}(t/2)}{\partial y} + i\kappa\Psi_{II}(t/2) & = & \nabla\Psi_I(t/2) \\ \nabla\Psi_{III}(-t/2) & = & (1+\chi)\frac{\partial \Psi_{II}(-t/2)}{\partial y} + i\kappa\Psi_{II}(-t/2) \end{array} \right. \tag{1.45}$$

one can derive the dispersion relation of MSSW. Collecting the similar terms together and solving the system of equations one obtains the dispersion relation as:

$$e^{-2kt} = \frac{(\chi+2)^2 - \kappa^2}{\chi^2 - \kappa^2}, \tag{1.46}$$

inserting χ and κ from (1.14) and developing (1.46), the dispersion relation is obtained as [100]:

$$\omega^2 = \omega_0(\omega_0 + \omega_M) + \frac{\omega_M^2}{4}[1 - e^{-2kt}] \tag{1.47}$$

The dispersion relation depends on the film thickness (t) and on the magnitude of the wavevector (k). The solid blue line in the figure-1.8 represents a plot of the dispersion relation of the MSSW configuration.
Arranging the boundary equations and solving for the constants, the scalar potential in the three layers can be written as:

$$\Psi_\nu(\overrightarrow{r}) = \left\{ \begin{array}{cc} \Psi_0(e^{kt} + p(\nu))e^{-ky+i\nu kx} & y > t/2 \\ \Psi_0(e^{ky} + p(\nu)e^{-ky})e^{i\nu kx} & -t/2 < y < t/2 \\ \Psi_0(1 + p(\nu)e^{kt})e^{ky+i\nu kx} & y < -t/2 \end{array} \right. \tag{1.48}$$

where Ψ_0 is a constant, and

$$p(\nu) = \frac{\Psi_{0-}}{\Psi_{0+}} = \frac{\chi - \nu\kappa}{\chi + 2 + \nu\kappa} e^{-kt}. \tag{1.49}$$

1.3.4.3 Characteristics of MSSW

The characteristics of the magnetostatic surface wave configuration are of a particular importance for this PhD thesis. Here we summarize some of these properties:

- **Dispersion relation**
  The dispersion relation in the MSSW is independent on the direction of ν for a thin film bounded by two dielectrics. In contrary to the other configurations the MSSW propagates with a single frequency instead of a series of modes as it was pointed for the MSFVW and the MSBVW. Notice also the frequency of the MSSW is higher than the limit for the frequency of a wave propagating in the bulk 1.3.1, this is because the wave of this configuration can not exist in the bulk of the ferromagnet. These waves exist only near the surface and for this reason they are known as surface waves.

- **Scalar potential**
  The scalar potential of the magnetostatic surface wave depends on the direction of ν. A mode propagating with a wave vector $\overrightarrow{k}$ has more amplitude near one of the surfaces. The largest amplitude is shifted to the other surface if the wavevector direction is reversed ($+\overrightarrow{k} \longrightarrow -\overrightarrow{k}$). This is known as field displacement non-reciprocity.

- **Wave amplitude**
  The wave amplitude is not distributed sinusoidally through the film thickness as in the MSFVW and MSBVW modes. It is decaying exponentially away from the surface of the film as shown in figure-1.9 which displays the variation of the magnitude of Ψ over the film thickness.

- **Dynamical magnetization**
  The dynamical components of the magnetization m_x and m_y have different magnitudes as shown in figure-1.9. The out of plane orientation of the demagnetizing field h_d along the y-axis reduces the magnitude of the magnetization m_y as shown in figure-1.7c. The asymmetry between m_x and m_y indicates that the magnetization has an elliptical trajectory.

- **The velocity**
  The MSSW configuration have also the highest group velocity among the three types of magnetostatic waves. The group velocity of the MSSW is given by
  $$v_g = \frac{\partial\omega}{\partial k} \qquad v_g = \frac{\omega_M^2 t}{4\omega} e^{-2kt}, \tag{1.50}$$
  the frequency increases with the wavevector which results in a positive group velocity.

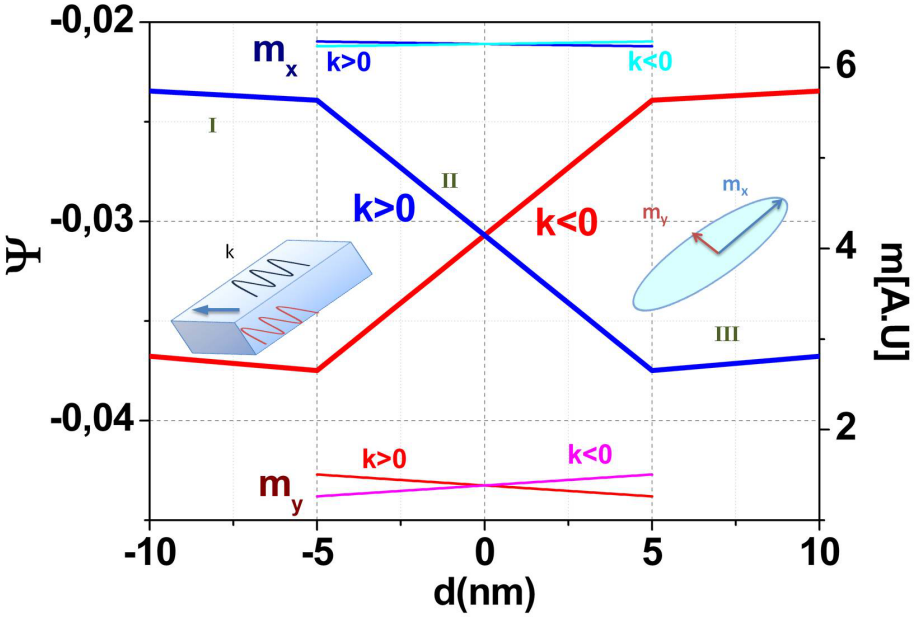

Figure 1.9: Plot of the scalar potential and of the dynamical magnetization distribution profile in the MSSW configuration. The calculation is performed with the following set of the parameters: thickness t =10nm, field $\mu_0 H_0$=30mT, $\mu_0 M_s$=0.9T, $\gamma/2\pi$ =29 GHz/T and k=3.86μm^{-1}. I, and III indicate the dielectric region whereas II indicates the magnetic layer.

1.3.5 Exchange-dipole regime

In the section 1.3, the wavelength (λ) of the spin waves is considered to be larger than the exchange length (l_{ex}), so that the spin waves are in the pure magnetostatic regime approximation. However, in the region where the wave propagates with a wavelength comparable to the exchange length one should account for the exchange interaction. The exchange-dipolar regime is briefly discussed in this section based on the Kalinikos-Slavin theory [55].

Due to the presence of the exchange operator in the effective field, the equation of motion will be an integro-differential equation of the second order. To solve this equation one needs supplementary boundary conditions in addition to the electromagnetic boundary conditions. Rado and Weertman [88] studied the modification in the ferromagnetic resonance under the influence of the exchange interaction. They introduced surface spin pinning conditions. The supplementary exchange boundary condition is written as [99]:

$$T_{surf} = -\frac{2A}{M_s^2} M \times \frac{\partial M}{\partial n}, \tag{1.51}$$

where n is the normal of the surface, and T_{surf} is the total surface torque density which arises from forces other than the exchange interaction. Using these

boundary conditions, Kalinikos and Slavin solved the integro-differential equation for the spin wave modes with an arbitrary angle between the propagation direction and the field. The dispersion relation of the spin wave in the case of the exchange-dipolar regime reads [55] :

$$\omega_n^2 = (\omega_H + \alpha\omega_M k_n^2)(\omega_H + \alpha\omega_M k_n^2 + \omega_M F nn) \tag{1.52}$$

with $k_n^2 = k_\parallel^2 + q_n^2$, where q_n is the wavevector over the thickness of the film, and $\alpha = \frac{2A}{\mu_0 M_0^2}$, with

$$F_{nn} = P_{nn} + sin^2\theta(1 - P_{nn}(1 + cos^2\phi) + \omega_M \frac{P_{nn}(1 - P_{nn}sin^2\phi)}{\omega_H + \alpha k_n^2}, \tag{1.53}$$

where the θ is the angle between the magnetization and the normal of the film, and ϕ is the angle between $\overrightarrow{M}$ and $\overrightarrow{k}$. P_{nn} are the matrix elements relating the dynamical magnetization and the dipolar field. In the case of unpinned surface spins ($q_n = \frac{n\pi}{d}$), the expression for P_{nn} has the form

$$P_{nn} = \frac{k^2}{k_n^2}(1 + \frac{k^2}{k_n^2}\frac{2}{1 + \delta_{0n}}\frac{1 - (-1)^n e^{-kt}}{kt}) \tag{1.54}$$

where δ_{0n} is the kronecker delta.
Figure-1.8 shows the dispersion relation in the exchange-dipolar regime (the dotted lines) for the three configuration of the spin wave (MSFVW, MSBVW, MSSW). The dispersion relation in the exchange-dipolar regime differs significantly from the dispersion relation of the magnetostatic regime at high k values.

1.4 Magnetization relaxation in ferromagnetic metal thin films

According to the Landau-Lifshitz model the effective field exerts a torque on the magnetic moments resulting in a precessional motion. However after a finite time the magnetization will align with the direction of the minimum energy. This relaxation of the magnetization is accompanied with a transfer of energy from the magnetic system to other degrees of freedom such as impurities, phonons, magnons, ... Various physical processes are responsible for the relaxation mechanism in metallic ferromagnetic systems, either through a spin-spin process or via a coupling with the lattice. In this section, a phenomenological description of the damping in the Landau-Lifshitz equation is introduced. Then a discussion of the possible physical origin for the relaxation processes is presented.

1.4.1 Phenomenological description

According to the (LL) equation-1.6, the magnetization can precess forever around the external field, and it never returns back to the equilibrium position which is its lowest energy state. Since in a real system the magnetization dynamics is always damped, Landau and Lifshitz proposed to introduce a damping term on the right hand of the equation-1.6 which reads:

$$\frac{\partial \overrightarrow{M}}{\partial t} = -\gamma\mu_0 \overrightarrow{M} \times \overrightarrow{H}_{eff} - \frac{\gamma\lambda}{M^2} \overrightarrow{M} \times (\overrightarrow{M} \times \overrightarrow{H}_{eff}), \tag{1.55}$$

where λ is a dissipation parameter with the dimensionality of a field. Although, equation-1.55 accounts for the damping, the most familiar equation of motion is the Landau-Lifshitz-Gilbert (LLG) equation. In 1955 Gilbert modeled the damping as a 'friction' which is proportional to the rate change of $\overrightarrow{M}$, the LLG equation reads as [38]:

$$\frac{\partial \overrightarrow{M}}{\partial t} = -\gamma\mu_0 \overrightarrow{M} \times \overrightarrow{H}_{eff} + \frac{\alpha}{M_s} \overrightarrow{M} \times (\frac{\partial \overrightarrow{M}}{\partial t}), \tag{1.56}$$

where α is a dimensionless coefficient known as the Gilbert damping coefficient. The equation-1.55 can be transformed to the equation-1.56 by performing the substitution:

$$\gamma \to \frac{\gamma}{1+\alpha^2}, \qquad \lambda \to \frac{\alpha M}{1+\alpha^2}.$$

The phenomenon of damping is sketched on the figure-1.10, where the precessing magnetization relaxes toward the direction of the effective field. Writing the linearized equation as in the section-1.2.1.1 one finds:

$$i\omega m = \hat{z} \times [-\omega_M h + (\omega_0 + i\alpha\omega)m], \tag{1.57}$$

it appears that the effect of the damping parameter is to add an imaginary part to the natural frequency of the oscillations. Accordingly, one can include the losses in the Polder tensor simply by performing the following transformation $(\omega_0 \to \omega_0 + i\alpha\omega)$.

The components of the Polder tensor are written as a sum of a real $(\chi^{'})$ and an imaginary $(\chi^{''})$ part. The real part is expected to change its sign and

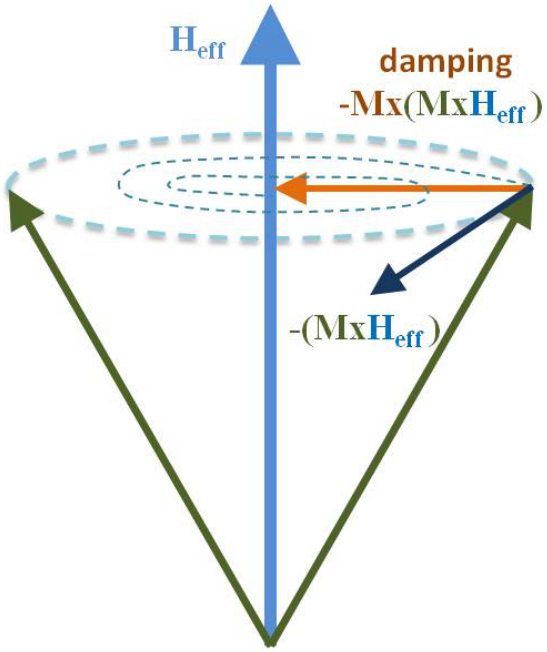

Figure 1.10: The damping term causes the magnetization to relax toward the direction of the effective field.

the imaginary part passes through a maximum at the resonance. The damping parameter α is extracted from the full width at half maximum (FWHM) of the imaginary part. In a conventional ferromagnetic resonance (FMR) experiment where we sweep the field at a fixed frequency the linewidth is $\Delta H = \frac{2\alpha\omega}{\gamma}$. The single parameter α contains a contribution from intrinsic and extrinsic relaxation processes as we will discuss in the following subsections.

1.4.2 Intrinsic processes

The intrinsic precession damping in transition metals elements and their alloys mainly results from the spin-orbit which couples the spin of the itinerant electrons with other degrees of freedoms. We shall now discuss the pictures for such processes.

- **Berger picture: collision of a magnon with conduction electrons**

  In this picture described in reference [12] a magnon with an energy $E(q) = \hbar\omega$ collides with an electron with an energy $\epsilon_{k,s}$ where s denotes its spin as shown in figure-1.11. The magnon is destructed and the electron is transferred from one band to another band with higher energy. One can distinguish between two cases:

– In the first case, the magnon-electron interaction conserves the spin angular momentum (e.g. s-d exchange interaction). Then the electrons should flip its spin during the collision. The magnon relaxation time (τ_m) is given by [12]:

$$\frac{1}{\tau_m} \propto [A + A'/\Lambda_e]E(q) \tag{1.58}$$

where Λ_e is the electronic mean free path.

– In the second case, the interaction does not conserve the spin momentum (e.g. spin-orbit coupling). The magnon relaxation time in that case is given by:

$$\frac{1}{\tau_m} = A\frac{m^2 E(q)}{\hbar^5 \pi^2 4q} arctan(\Lambda_e q). \tag{1.59}$$

where A is a constant related to the anisotropic exchange factor.

The magnon relaxation time in the 2 processes depends on the overlap between the spectral density of the state of the occupied and unoccupied states around the Fermi level. Due to the Heisenberg uncertainty principle the finite mean free path of the electrons implies an uncertainty on the wavevector of the electrons ($\Delta k = \Lambda_e$). The relaxation time increases linearly with the frequency ω, with a constant slope proportional to the Gilbert damping factor ($\alpha = (2\omega\tau_m)^{-1}$).

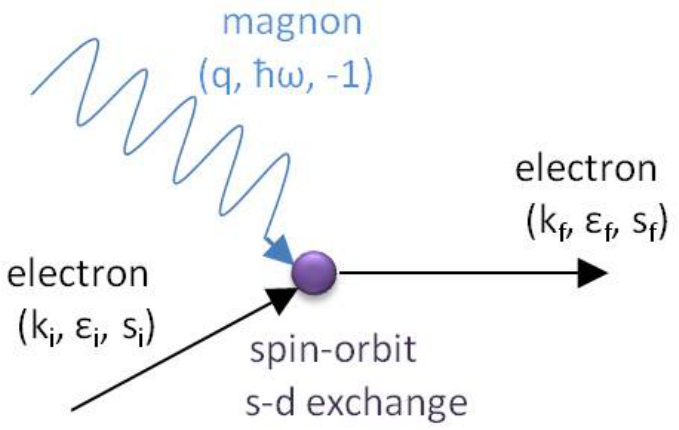

Figure 1.11: A sketch showing a magnon with an energy $\hbar\omega_q$ being absorbed by an electron with an energy ε_i and being scattered to a state with an energy ε_f.

- **Elliot-Yafet picture: phonon-magnon collision:**

In this picture, the magnetization relaxation is due to the interaction between the magnon and the lattice vibration. The process is a destruction of a spin precession by a phonon, assisted by a spin flip of the electron state. This interaction is mediated by the spin-orbit interaction. In the presence of the spin orbit interaction, the electron wavefunctions are an admixture of spin-up and spin-down states. Hence, phonon scattering induces finite spin flip probabilities. The scattering rate of the magnon is given by [56]:

$$\tau^{-1} = (\frac{\gamma\hbar}{2})^2 Z_f \tau_s^{-1}, \tag{1.60}$$

where τ_s is the spin flip relaxation given by $\tau_s^{-1} = \frac{(\delta g)^2}{\tau_e}$. $(\delta g)^2$ is the deviation of the g-factor from the free-electron value, τ_e is the ordinary electron-phonon collision, and Z_f is the density of states at the Fermi level.

- **The Kambersky torque model**

The torque model proposed by Kambersky [56] describes the non monotonic dependence of the damping of the transition metals (Fe, Co, Ni) as a function of the temperature. In this model, the damping of a uniform precession is dominated by a combination of the spin-orbit coupling and the electron-lattice scattering. This process includes 2 sub-mechanisms: first a uniform magnon decays into an electron-hole pair due to the spin-orbit coupling, then the electron-hole pair is scattered by the lattice vibration. In the Landau-Lifshitz formulation the magnetization conserves its magnitude whereas it changes its direction. Due to the spin-orbit interaction, the precession of the magnetization is accompanied by a variation of the energy of the electron states, and by transitions between the electron states. The effective field H_{eff} is written as:

$$H^{eff} = -\frac{1}{\mu_0 M} \sum_{n,k} [\rho_{n,k} \frac{\partial \varepsilon_{n,k}}{\partial M} + \varepsilon_{n,k} \frac{\partial \rho_{n,k}}{\partial M}], \tag{1.61}$$

where $\varepsilon_{n,k}$ is the energy of a single electron state and $\rho_{n,k}$ is the state occupancy. Let us examine how the two terms in the right hand side of equation-1.61 can lead to a relaxation of the magnetization dynamics.

  - **Intraband transition:**

    The first term of the effective field represents the variation of the spin-orbit energy of the state with the direction of the magnetization. This term causes a variation of the Fermi surface. As a consequence some of the occupied states below the Fermi level are shifted above it, and other unoccupied states above the Fermi level are shifted down. The resulting out of equilibrium electrons distribution is brought back to the equilibrium by intraband transitions due to scattering. This process known as a "breathing Fermi surface" was described by Kambersky [56], Koreman [60] and Gilmore [39]. The damping rate is given

by:

$$\lambda_{bfs} = \pi\hbar\frac{\gamma^2}{\mu_0}\sum_n \int \frac{d^3k}{(2\pi)^2}\Gamma_n^-(k)^2 \times \int d\varepsilon_1 A_{nk}(\varepsilon_1)A_{nk}(\varepsilon_1)\eta(\varepsilon_1). \tag{1.62}$$

The integral describes the overlap between the spectral density $A_{n,k}(\varepsilon)$ of states with the same band index n around the Fermi level. The torque matrix elements are described by the term Γ_n^-. A calculation of the damping rate using the torque model by virtually modifying the Fermi level performed by [39] shows a correlation between the damping coefficient and the density of states of the material as shown in fig-1.12 for (Fe, Co, Ni). The integral of the square of the spectral functions is proportional to the scattering time just as the conductivity. .

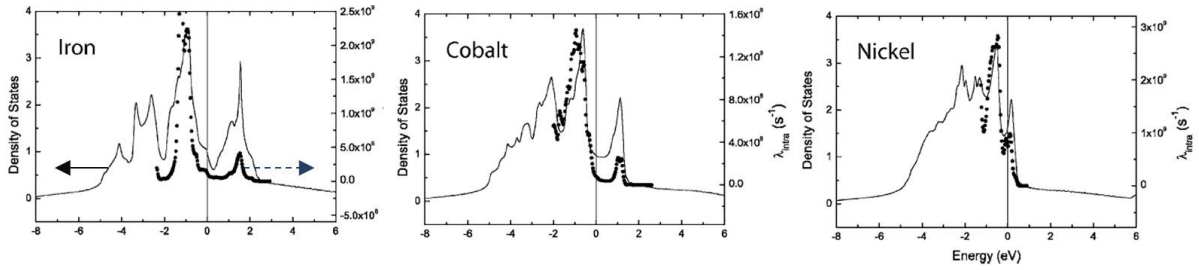

Figure 1.12: The calculated damping rate due to intraband transitions compared with the density of state for Fe, Co, and Ni. The image is taken from [39].

– **Interband transition:**

The second term of the effective field represents the change of the occupancy of the state due to the rotation of the magnetization. The rotation acts as a time dependent perturbation caused by band transitions between the states $\Psi_{m,k}$ and $\Psi_{n,k}$ (same wavevector but different band). The damping rate is given as [39]:

$$\lambda = \pi\hbar\frac{\gamma^2}{\mu_0}\sum_n\sum_{m\neq n} \int \frac{d^3k}{(2\pi)^2}\Gamma_{mn}^-(k)^2 \times \int d\varepsilon_1 A_{nk}(\varepsilon_1)A_{mk}(\varepsilon_1)\eta(\varepsilon_1), \tag{1.63}$$

where the integral represents the overlap between the electron spectral function of the bands A^m and A^n. The probability of interband transitions between the states m and n depends on the energy difference $\varepsilon_m - \varepsilon_n$. If the scattering rate $\hbar/\tau$ is less than the energy difference the interband transition probability is inversely proportional to the scattering time just like the resistivity.

The torque operator is written as:

$$\Gamma^- = \xi(l^-\sigma^z - l^z\sigma^-),$$

where the ξ is the strength of the spin-orbit coupling. The torque operator acts to lower the angular momentum of the state. This happens either by lowering the spin-orbit moment through a spin flip or by lowering the orbital momentum through an orbital excitation. Then the intraband and interband transition both have two sub mechanisms: either an orbital excitation or a spin flip process.
We consider the unperturbed spin state as ψ_n^0 and the spin-orbit interaction as a perturbation potential $V = \xi V^{'}$. The states can be expanded as:

$$\psi_n = \psi_n^0 + \xi^1 \psi_n^1 + \xi^2 \psi_n^2.$$

The damping rate due to intraband transitions is found to have a quadratic dependence on ξ and it is dominated by the orbital excitations. The damping rate due to interband transitions is found to be of the third order in ξ, it contains contributions from both the orbital excitations and the spin flip process.
The damping rate of bulk Ni metal is observed to increase as the temperature decreases, and it shows a plateau at low temperature, however the damping rate of bulk Fe varies slowly with the temperature, it varies of about less than a factor of 2 between 4 and 300 K [15]. The damping rate in Ni is higher than in Fe which is attributed to a larger density of states and to a larger spin orbit coupling.
Recently, first principle calculations accounting for disorder and spin-orbit coupling in bulk permalloy give $\alpha = 0.0046$ [101]. All these observations are explained by the torque model described above.

1.4.3 Inhomogeneous broadening

Magnetic inhomogeneities in a thin film result in an extrinsic broadening of the ferromagnetic resonance line. Such inhomogeneities can arise from a spatial distribution of the local field or from the misalignment of the applied field with respect to the normal of the surface of each individual crystallite.
The effect of inhomogeneities can be easily understand in two extreme cases:

- **Negligible inhomogeneity:**
  If the magnetic material is uniform the inhomogeneity could be ignored and the line width represents the intrinsic damping only.

- **Uncorrelated grains:**
  When the exchange and the dipolar interaction between the grains of an inhomogeneous sample are negligible, the grains are oscillating independently (local resonance). Then the measured linewidth reflects the convolution of the intrinsic line with the distribution of the resonance fields.

In the intermediate case where the different grains are correlated and the magnetic inhomogeneities are considered, the broadening might be described in some cases by the 2-magnon model [71] [3]. In the following we will describe the more general mean field model proposed by McMichael [70].
In this model the film is divided into blocks, where the block size D is chosen as a characteristic length scale of the inhomogeneity. The static field H is oriented along the x-axis and the pumping field h_p is in the yz plane. In each individual

block (i) the linear response to a magnetic field is described as:

$$m_i = \chi_i(\omega, H_x, K_i).h_i, \tag{1.64}$$

where the local susceptibility $\chi_i(\omega, H_x, K_i)$ depends on the frequency ω, the local static field, and on a parameter K_i that differs by from one block to another. In each block the field is a sum of the applied field and the interaction field between different blocks. The interaction field is assumed to depend on the average of the magnetization M. It is written in terms of the interaction tensor J as:

$$H_{int} = J.M = J_x M_s + J_{yz}.\chi_{eff}.h_p, \tag{1.65}$$

where J_{yz} is the y-z part of the J and χ_{eff} is the global magnetic susceptibility of the film. Substituting the H_{int} in equation 1.64 and averaging over the blocks we obtain,

$$\bar{m} = \bar{\chi}(\omega, H_0 + J_x M_s, K_i)[I + J_{yz}\chi_{eff}].h_p, \tag{1.66}$$

where I is the identity tensor, and $\bar{\chi}$ is the average susceptibility of the block array which represent the susceptibility of the non interacting blocks with a distribution P(K) of the local properties, with a shift of the applied field by the interaction field. Then one can deduce the

$$\chi_{eff} = [(\bar{\chi}(\omega, H_0 + J_x M_s, K_i))^{-1} - J_{yz}]^{-1} \tag{1.67}$$

McMichael determines numerically χ_{eff} accounting for exchange and dipolar interaction in J. The full width half maximum (FWHM) is extracted from the imaginary part of the effective susceptibility. The calculation was done for a permalloy film of thickness 3 nm, and Gilbert damping coefficient $\alpha = 0.008$ with the exchange length 5.7nm. The inhomogeneity is considered to be due to a local anisotropy field added to the applied field, and the distribution P(K) is considered to be Gaussian with a standard deviation σ. The calculated linewidth for different values of the block size are shown in figure 1.13. For infinite blocks one recovers the local resonance results whereas for smaller blocks the frequency dependence becomes non-linear and gradually tends to the intrinsic linewidth.

1.4.4 Slow relaxers

Consider a ferromagnet layer coupled to a fluctuating system with a relaxation time τ. It can be shown that the ferromagnet resonance is modified as follows: at a constant frequency ω the resonance field is shifted down by an amount S and the line is broadened by ΔH, where S and ΔH writes:

$$\begin{array}{c} S \propto \frac{1}{2}\frac{(\omega\tau)^2}{1+(\omega\tau)^2} \\ \Delta H \propto \frac{\omega\tau}{1+(\omega\tau)^2}. \end{array} \tag{1.68}$$

Because τ is assumed to vary strongly with the temperature, the slow relaxers phenomenon results in strong temperature dependence of S and ΔH. This has been observed in YIG doped with rare earth metals, in Py doped with rare earth [114] and in exchange bias bilayer systems such as Py/NiO [29][64] or Py/FeMn [40]. In each system the relaxation mechanism of the slow fluctuators is different which yields a different temperature scale.

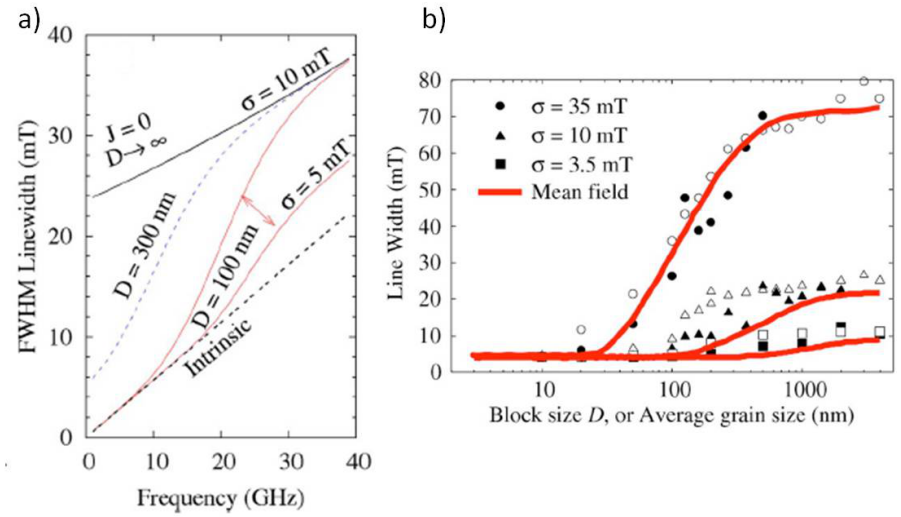

Figure 1.13: a) Frequency dependence of full width at half maximum linewidth. b) The red lines are the meanfield results compared to an eigenmode spectrum calculated in [71]. The image is taken from the reference [70].

Conclusion

In this chapter, we describe the uniform magnetization and the spin waves phenomena in the ferromagnetic thin films. A special attention to the magnetostatic surface waves characteristics is provided since we choose to perform the experiments using this configuration. And a general review of the magnetization relaxation processes in thin films is presented.

Chapter 2

Electrical transport and spin transfer torque in ferromagnetic metal thin films

This chapter is dedicated to explain the physical basis needed for the discussion of the film thickness dependence of the spin polarized transport. It is divided into three sections. In §2.1 we will discuss the electrical transport in ferromagnets based on the two current model. In §2.2 the electron-surface scattering is presented based on the Fuchs-Sondheimer model. In §2.3 the spin transfer torque phenomenon is explained and some experimental observations are presented.

2.1 Electrical transport in a ferromagnet

The two current model is a well known model used to describe the spin dependent transport in a ferromagnetic metal. This section discusses first the basic vision of the two current model, then it presents the calculation suggested by Fert and Campbell to make it more realistic. Finally more recent ab initio calculations illustrating the limitations of the two current model are discussed.

2.1.1 The two current model

In transition metals, the electrons are split into two populations according to their spin direction, the spin-up (majority) and the spin-down (minority) electrons whose spin magnetic moment is parallel and antiparallel to the magnetization direction respectively. The electron states for the majority and the minority electrons at the Fermi levels are different as shown in figure 2.1-a. This yields a different scattering probability for the 2 populations or equivalently different relaxation times. Consequently, the resistivity of the spin-up $\rho_{\uparrow}$ and spin-down $\rho_{\downarrow}$ channels are different. Accordingly, Mott proposed to describe the transport properties of a ferromagnet in terms of the two current model. It depicts the spin-up and the spin-down electrons as two independent conduction channels as shown in the figure- 2.1-b. The physical background of the two current model is that the interaction between the two bands are small. At low temperature, one

can neglect any angular momentum transfer between the two channels (no spin flip scattering).

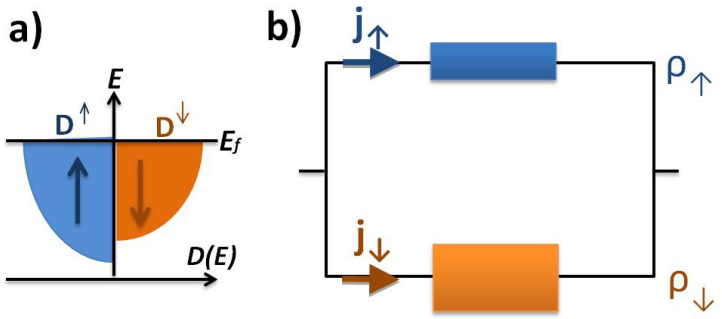

Figure 2.1: a- The density of state for the majority and minority electrons in a ferromagnet. b- A scheme for the two current model showing the resistivity of the spin up $\rho_\uparrow$ and the spin down $\rho_\downarrow$ channels.

Accordingly, the two channels contribute to the resistivity of the metals as two parallel resistors. Then the total resistivity is given as parallel resistance [19]:

$$\rho = \frac{\rho_\uparrow \rho_\downarrow}{\rho_\uparrow + \rho_\downarrow}, \tag{2.1}$$

with the scattering spin asymmetry ratio defined as

$$\alpha = \frac{\rho_\downarrow}{\rho_\uparrow}. \tag{2.2}$$

And the degree of spin polarization defined as:

$$P = \frac{\rho_\downarrow - \rho_\uparrow}{\rho_\downarrow + \rho_\uparrow} = \frac{\alpha - 1}{\alpha + 1}. \tag{2.3}$$

The spin dependent resistivities were determined by measuring the deviations from the Matthiessen rule in binary and ternary alloys obtained by diluting different impurities into ferromagnetic metals. The Matthiessen rule would suggest that the total resistivity is the sum of the resistivities (ρ^i) one would have if each scattering process (each impurity) were present alone [4] as series resistance:

$$\rho = \sum_i \rho^i. \tag{2.4}$$

In the case of impurities into Ni[30], Fe, and Co [63] large deviation from the Matthiessen rule were observed which were interpreted as signatures of large spin asymmetry ratios. In particular, for most impurities in Ni it was shown that the majority channel carries most of the current.

2.1.2 The modified two current model

Fert and Campbell [34] presented theoretical calculations of the two current model where the spin-flip scattering events are considered. Here, we refer to their calculation of the spin dependent resistivities.

In this model, the Boltzmann equation is solved for a distribution of the spin up and the spin down electrons using the variational method used by Ziman [120]. In the notation of Ziman, the Boltzmann equation is expressed as a deviation of the electron distribution from the equilibrium under the action of an external field. The Boltzman equation is written as [120]:

$$X = P\Psi(k,\sigma), \tag{2.5}$$

where X depends on the external field, P is the scattering operator and $\Psi(k\sigma)$ is the deviation of the electron distribution from its equilibrium defined as:

$$f(k\sigma) = f_0(\epsilon_k) - \Psi(k\sigma)(\frac{\partial f^0}{\partial \epsilon_k}),$$

where k is the wavevector and $\sigma = \pm\frac{1}{2}$ is the spin index. The problem is simply to find the form of the $\Psi(k\sigma)$ by searching for a minimum value of the quantity:

$$\frac{<\Psi, P\Psi>}{|<\Psi, X>|^2}. \tag{2.6}$$

To determine the out of equilibrium distribution, a trial solution of $\Psi(k\sigma)$ is expressed in terms of a linear combination of the spin up and the spin down distribution $\phi_\sigma(k)$ as:

$$\Psi(k\sigma) = \sum_{\sigma'} \eta_{\sigma'}\phi_{\sigma'}(k)\delta_{\sigma\sigma'}, \tag{2.7}$$

where $\phi_{\sigma'}(k)$ is assumed to be known and independent on the scattering process, while $\eta_{\sigma'}$ are variable coefficients which have to be adjusted to find the minimum. The values of $\eta_{\sigma'}$ are given by:

$$EX_\sigma = \sum_{\sigma'} P_{\sigma\sigma'}\eta_{\sigma'} \tag{2.8}$$

where $X_\sigma = -\int (v_k.u)e\frac{\partial f^0}{\partial \epsilon_k}\Phi_\sigma(k)dk$ with u a unit vector in the direction of the applied electric field (E), and $P_{\sigma\sigma'}$ is

$$P_{\sigma\sigma'} = \frac{1}{k_B T}\sum_{\sigma''\sigma'''}[\phi_\sigma(k)\delta_{\sigma\sigma''} - \phi_\sigma(k')\delta_{\sigma\sigma'''}]P(k_{\sigma''}k'_{\sigma'''})\times[\phi_{\sigma'}(k)\delta_{\sigma'\sigma''} - \phi_{\sigma'}(k')\delta_{\sigma'\sigma'''}]dkdk'. \tag{2.9}$$

where $P(k_{\sigma''}k'_{\sigma'''})$ is the equilibrium rate between the state $(k\sigma'')$ and $(k'\sigma''')$. Ziman wrote the electrical resistivity ρ as:

$$\rho^{-1} = \Sigma_{\sigma\sigma'}X_\sigma(P^{-1})_{\sigma\sigma'}X_{\sigma'}. \tag{2.10}$$

The circuit scheme in the figure 2.2 represents the scattering processes after including the spin-mixing. The total resistivity and the degree of the spin po-

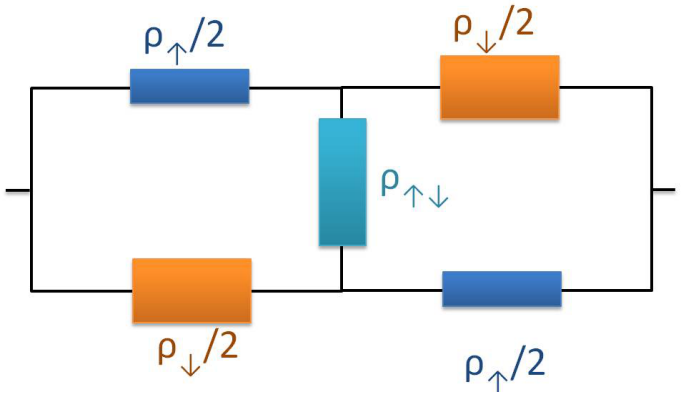

Figure 2.2: A scheme for the two current model after the spin flip scattering is included.

larization are:

$$\begin{aligned} \rho &= \frac{\rho_\uparrow\rho_\downarrow+\rho_{\uparrow\downarrow}(\rho_\uparrow+\rho_\downarrow)}{\rho_\uparrow+\rho_\downarrow+4\rho_{\uparrow\downarrow}}, \\ P &= \frac{\rho_\downarrow-\rho_\uparrow}{\rho_\uparrow+\rho_\downarrow+4\rho_{\uparrow\downarrow}}, \end{aligned} \tag{2.11}$$

where

$$\begin{aligned} \rho_\uparrow &= \frac{P_{\uparrow\uparrow}}{X_\uparrow^2} + \frac{P_{\uparrow\downarrow}}{X_\uparrow X_\downarrow} \\ \rho_\downarrow &= \frac{P_{\downarrow\downarrow}}{X_\downarrow^2} + \frac{P_{\downarrow\uparrow}}{X_\downarrow X_\uparrow} \\ \rho_{\uparrow\downarrow} &= -\frac{P_{\uparrow\downarrow}}{X_\uparrow X_\downarrow}. \end{aligned} \tag{2.12}$$

This is a general expression of the resistivity which accounts for the interband transitions between the majority and the minority electrons. The $\rho_\uparrow$, $\rho_\downarrow$, $\rho_{\uparrow\downarrow}$ are linearly proportional to the scattering operator, which indicates that the different scattering processes provide an additive contribution to the resistivity, which justifies *Mathiessen's* rule for each sub-band resistivity. In this model the band σ includes all the electrons with the spin σ with s, d or hybridized characters.
The spin flip scattering events tend to the equalize the currents in the two channels. They could be attributed to two different scattering processes:

- In the first process, the conduction electrons scatter onto spin waves. By conservation of the angular momentum, this is accompanied with a spin flip. This process induces a $\rho_{\uparrow\downarrow}(T)$ which vanishes at T= 0K as calculated by [33] [90].

- In the second process, the spin-orbit coupling can contribute to a spin flip scattering of conduction electrons even at low temperature. The spin-orbit coupling mixes the spin state of each band and there is no more pure spin state. The majority spin electron states acquire some minority character,

so that the electrons can be scattered into the minority spin band states. The additional scattering in light metals as Ni, Fe is strong because of the large minority density of the final state. Consequently the resistivity is strongly enhanced [22].

2.1.3 Ab-initio calculation of spin dependent resistivities

Mertig et al. [74] performed an ab-initio calculation of the spin-dependent resistivity for the dilute Ni alloys. The calculation of the residual resistivity confirms that the current is mostly carried by the electrons of the majority band in most cases, whereas the calculated values of the residual resistivity for Ni alloyed with Fe, Zn ,Co, and Cu impurities are too small compared to the measured values. The small calculated values of the resistivities highlight the importance of including the spin-orbit coupling since it was ignored in their calculation. Banhart et al. [9] have performed a fully relativistic transport calculation of the resistivities in ferromagnetic alloys of $Ni_{1-x}Fe_x$ and $Co_{1-x}Fe_x$. They obtained higher values of the resistivities which are more comparable to the experimental measurements. This work shows the importance of the spin-orbit coupling which is in contrast to the assumption of the basic two current model.

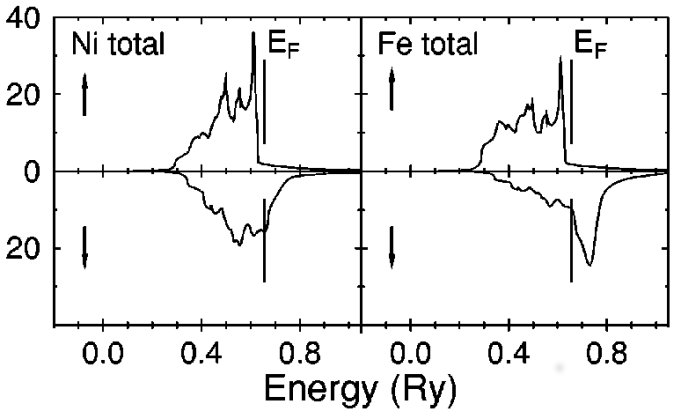

Figure 2.3: The density of the state for the majority and the minority spin band of the Nickel and Iron. The figure is taken from the reference [75].

In $(Ni_{80}Fe_{20})$ permalloy, the impurities act as spin-dependent scattering centers as Minjnarends et al. [75] suggested. Figure-2.3 shows the density of states for the spin-up and the spin-down bands (top and bottom panel respectively) for Ni and Fe sites (left and right panels respectively). The density of states of the majority spin band of both Nickel and Iron sites have a narrow peak below the Fermi level and they are almost at the same energy, which indicates that the majority spin up of Ni is undamped by the Fe impurities. However the density of the state of the minority spin band of the nickel and iron are significantly different, and hence the minority spin down of Nickel are strongly damped by the Fe impurities.

2.2 Size effect

In the form of thin films, metals can show higher resistivities than in the bulk if their thickness is comparable to the electronic mean free path. A large number of measurements of thickness dependence of the resistivity were done for different materials (Cu, Ni, Au,...), in order to study this phenomenon. To interpret these measurements, theoretical models separating the surface and the bulk scattering contributions have been used. The Fuchs-Sondheimer theory [98] is the leading theory for this. This section will discuss the size effects in a thin film. We will first focus on the electron surface scattering (the Fuchs- Sondheimer theory) and we will briefly describe the electron scattering due to the grain boundaries. At the end of the discussion, experimental work is presented for some materials.

2.2.1 Surface scattering in thin films

Fuchs-Sondheimer model

The aim of this section is to present the electron surface scattering contribution to the resistivity based on the Fuchs-Sondheimer theory [98]. The formalism consists in solving the Boltzmann equation accounting for the boundary conditions at the film surfaces.
Consider a metallic thin film of thickness t, such that the surfaces of the film are located at the planes z=0 and z= t. The velocity distribution function of the electrons can be written as: $f = f_0 + f_1(v, z)$, where f_0 is the equilibrium distribution and f_1 is the out of equilibrium distribution which depends only on the z coordinate. The rest of the problem is to solve the Boltzmann equation to determine this out of equilibrium function. Suppose the electrical field (E) is applied along the x-direction, the Boltzmann equation can be written as:

$$\frac{\partial f_1}{\partial z} + \frac{f_1}{\tau v_z} = \frac{eE}{mv_z}\frac{\partial f_0}{\partial x} \tag{2.13}$$

where τ is the relaxation time of the electrons. The general solution of the Boltzmann equation can be written as:

$$f_1 = \frac{e\tau E}{m}\frac{\partial f_0}{\partial v_x}\{1 + F(v)\exp(-\frac{z}{\tau v_z})\} \tag{2.14}$$

where $F(v)$ is an arbitrary function of the velocity. By imposing the boundary condition one can determine $F(v)$. Fuchs-Sondheimer introduces a p coefficient in the model to describe how the electrons are scattered from the surface. The p-coefficient is assumed to be independent of the motion of the electrons and it has a value between 0 and 1. For p=0 the surface scattering is completely diffusive (i.e the momentum is randomized) and for p=1 the scattering is specular (i.e the in-plane momentum is conserved). The boundary condition can be written for the electrons leaving the surface $z = 0$ and $z = t$ in terms of the distribution functions f_1^+ and f_1^- for the electrons with the velocity $v_z > 0$ and $v_z < 0$ as:

$$f_0 + f_1^+(v_z, z = 0) = p(f_0 + f_1^-(-v_z, z = 0)) + (1 - p)f_0 \tag{2.15}$$

$$f_0 + f_1^-(v_z, z = t) = p(f_0 + f_1^+(-v_z, z = t)) + (1 - p)f_0 \tag{2.16}$$

With these two boundary conditions the solution of the Boltzmann equation can be written as:

$$\begin{array}{lcll} f_1^+(v_z,z) & = & \frac{e\tau E}{m}\frac{\partial f_0}{\partial v_x}[1-\frac{1-p}{1-p\exp(-\frac{t}{\tau v_z})}\exp(-\frac{z}{\tau v_z})] & v_z>0 \\ f_1^-(v_z,z) & = & \frac{e\tau E}{m}\frac{\partial f_0}{\partial v_x}[1-\frac{1-p}{1-p\exp(-\frac{t}{\tau v_z})}\exp(\frac{t-z}{\tau v_z})] & v_z<0. \end{array} \quad (2.17)$$

Once the distribution function of the electrons is known, the current density J can be calculated using

$$J = 2e(\frac{m}{h})^3 \int v f dv, \quad (2.18)$$

then Fuchs and Sondheimer deduce the conductivity of the thin film to be:

$$\frac{\sigma_0}{\sigma} = \frac{\phi_p(\kappa)}{\kappa} \quad (2.19)$$

where $\kappa = \frac{t}{\ell}$, with ℓ is the electron mean free path and

$$\frac{1}{\phi_p(\kappa)} = \frac{1}{\kappa} - \frac{3}{2\kappa^2}(1-p)\int_1^\infty (\frac{1}{t^3}-\frac{1}{t^5})\frac{1-e^{-\kappa t}}{1-pe^{-\kappa t}}dt. \quad (2.20)$$

For very thick films ($\kappa >> 1$), equation-2.19 can be written as:

$$\frac{\rho}{\rho_0} = \frac{\sigma_0}{\sigma} = 1 + \frac{3}{8\kappa}(1-p). \quad (2.21)$$

This equation is still approximately valid even if the thickness is comparable to the mean free path.
Accordingly, the electron-surface scattering contributes to the resistivity of the thin films in addition to the bulk scattering. Normally, the surface scattering contribution to the resistivity is determined by carrying out a thickness dependence measurements of the resistivity as we will see in chapter 3.

2.2.2 Grain boundaries

This section will discuss briefly the contribution to resistivity of the electron scattering by the grain boundaries. The scattering of the electrons by the grain boundaries is believed to have a small effect on the resistivity, when the grain size (d) in a metallic film is larger than the mean free path. Mayadas et al. [68] proposed a model to account for the contribution of the grain boundary scattering to the total resistivity. In this model, the grain boundaries are represented by N parallel planes oriented perpendicular to the direction of the electrical field. Each of these planes is modelled as a δ function potential. The reflection of the electrons due to the grain boundaries is described by a reflection coefficient (R). Mayadas et al. solved the Boltzmann equation to evaluate the conductivity in the presence of the grain boundaries and background scattering (phonons, defects) they obtained:

$$\frac{\sigma_g}{\sigma_0} = 1 - \frac{3}{2}\alpha + 3\alpha^2 - 3\alpha^3 \ln(1+\frac{1}{\alpha}), \quad (2.22)$$

where $\alpha = \frac{\ell}{d}\frac{R}{1-R}$.
The scattering of the electrons by the grain boundaries for fine grains can usually be included as a bulk parameter.

2.2.3 Experimental measurements

During the 1970's and 1980's many studies were carried out to understand the size effects in a wide range of metals such as (Al, Cu, Pd, Au, Ni,..) [109]. In these studies, the bulk resistivity (ρ) and the mean free path (ℓ) are extracted with the help of various models [46]. Mainly, ρ and ℓ are extracted using the Fuchs-Sondheimer model and/or the Mayadas model, in these models the only adjusted parameters are the specularity parameter p and the reflection coefficient R.
Jacob et al. [53] suggested a method to separate the surface and volume scattering in a polycrystalline metal. In this work, the surface of Cu films were coated with adatoms of Ni or Al. Accordingly, the surface scattering increases whereas the volume scattering remained unchanged. From the maximum relative increase in the resistivity at two different temperature of two identical films coated, the mean free path can simply be determined. Using this method the mean free path and the specularity parameter are $\ell(300K) = 24 \pm 4nm$, p= 0.42 ± 0.07. In the following, we will present two recent thickness dependence

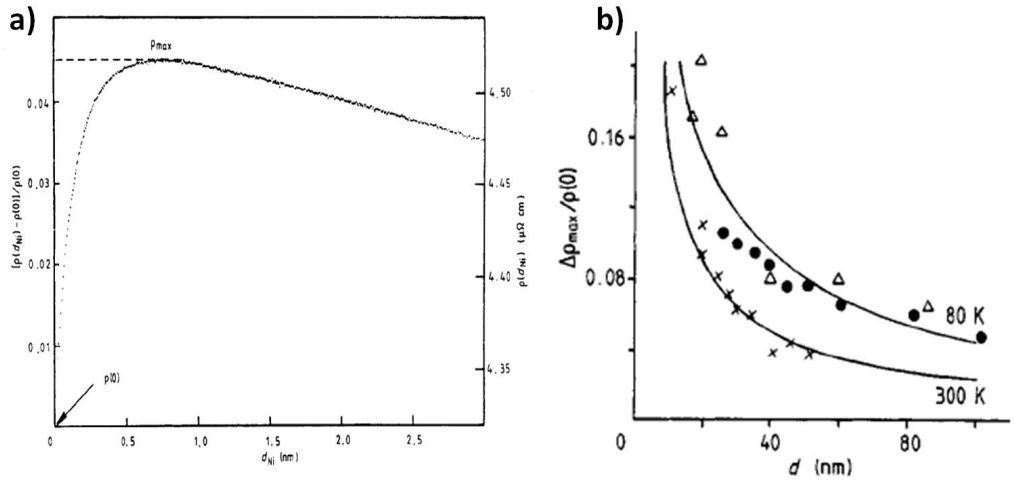

Figure 2.4: a) The variation of the resistivity of a copper film during coating with nickel atoms. b) The relative change in resistivity during coating with Ni and Al atoms as a function of the copper film thickness. The image is taken from the reference [53].

studies performed on copper thin films and gold nanowires.

Figure-2.5 shows measurements of the thickness dependence of the resistivity on epitaxial copper thin film done by [21]. The resistivity measurements were done at 298 K in vacuum and in air, and at liquid nitrogen (77 K). The results follow the FS model with the parameter $p = 0.6 \pm 0.2$ for Cu-vacuum interface and $p = 0 \pm 0.1$ for the Cu-air interface with a mean free path $\ell = 39$ and 313 nm for 298 K and 77 K.
In the second study the film thickness was held constant whereas the width of the

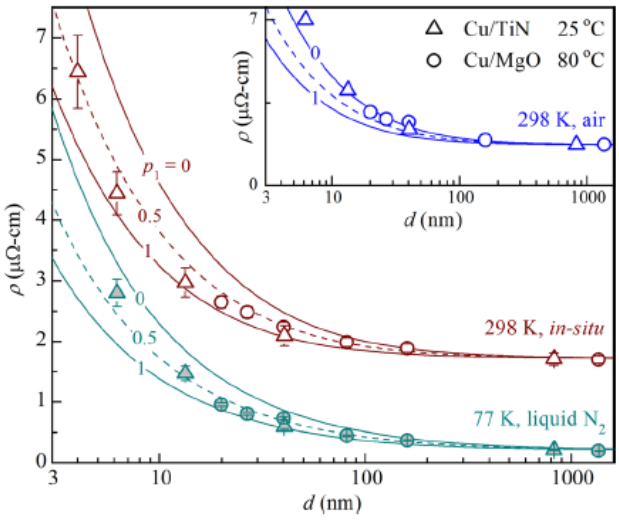

Figure 2.5: The variation of the resistivity as a function of the film thickness for epitaxial copper thin films. The image is taken from the reference [21].

gold nanowire is varied [31]. The measured resistivity values are not accounted well by the Fuchs-Sondheimer theory as shown in figure 2.6a. This deficiency is resolved when the grain boundaries contribution is considered. A better fit of the result was done with a combination of the Fuchs-Sondheimer and the Mayadas-Shatzkes theory as shown in the figure 2.6b. The parameter of the fit were obtained as $\ell = 40$ nm, average grain size is 40 nm, p=0.5 and R=0.9.

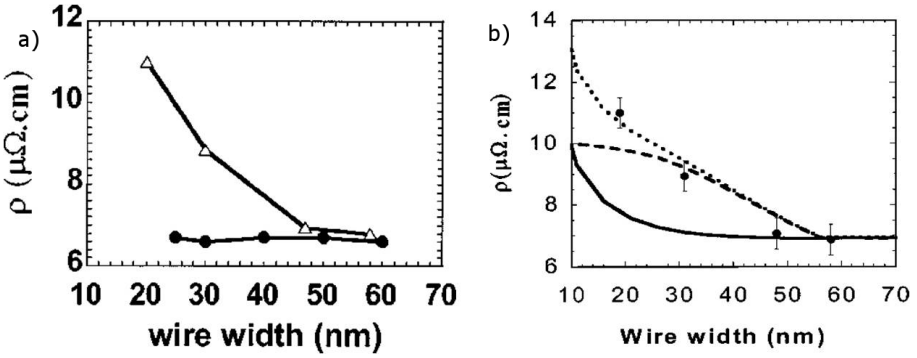

Figure 2.6: The variation of the resistivity in a nanowire of gold of thickness 20 nm as a function of the wire width. A) Measured dependence of resistivity on wire width for a mean grain size of 20 nm (filled circles) and 40 nm (triangles). B) A fitting of the data with fuchs Sondheimer (solid line), Mayadas-Shatzkes (dashed curves) and a combination of the two models (dotted curves). The image is taken from the reference [31].

2.3 Spin transfer torque

After the discovery of the spin transfer torque by Berger [13] and Slonczweski [97] in 1996, this phenomenon has attracted the attention for fundamental and technological studies. In this section, the basic elements for understanding the spin transfer torque are discussed.

2.3.1 Spin current

A moving ensemble of spins engenders a spin current. It originates from an imbalance between the number of the spin-up and the spin-down carriers. In other words due to the spin-dependent properties of the electrons in a ferromagnet, a magnetic layer can act as a spin filter. Because the spin current is a flow of spins, it is characterized by a velocity velocity vector **v** in the real space and a spin density vector **S** in the spin space. Classically, the spin current Q_{ij} is a tensorial quantity defined as: Q_{ij}=$S_i \bigotimes v_j$.

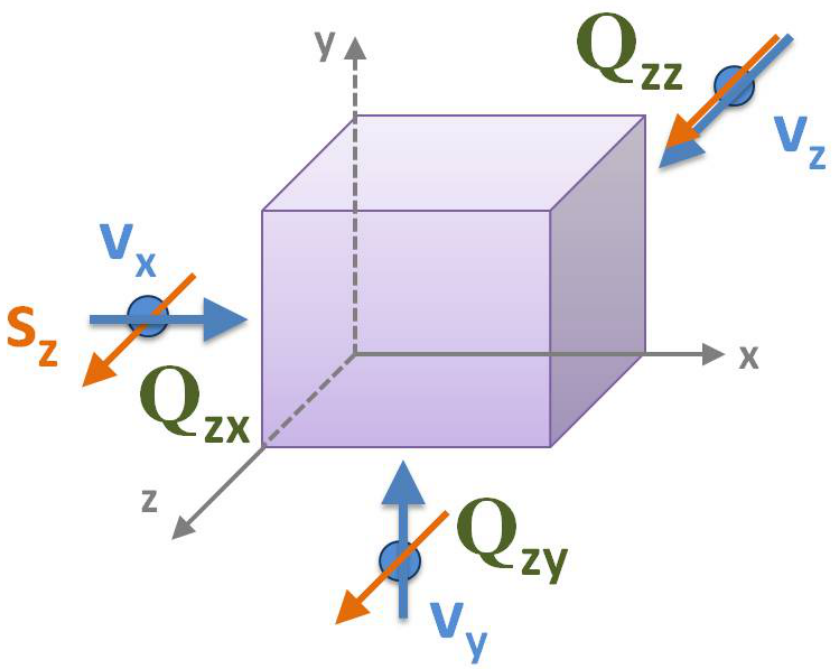

Figure 2.7: A scheme for the spin current definition. It shows the motion of a spin S_z in the real space [110].

Figure-2.7 shows a schematic drawing for the spin current associated to the z-component of a spin. The spin current associated to a motion along the three axis is shown (v_x, v_y, v_z).

2.3.2 Spin transfer torque

In 1996, Berger [13] and Slonczweski [97] studied independently the coupling between a spin polarized current and the magnetization of a ferromagnetic layer in a multilayer structure. They predicted a vectorial transfer of the spin angular momentum between the flowing electrons and the magnetization. This is the so called spin transfer torque phenomenon. It arises whenever the flow of angular momentum is not constant through the ferromagnet.
Figure-2.8 illustrates the basic physics of the spin transfer torque. It describes the interaction between the spin of the electrons flowing and the magnetization. This interaction results in a reorientation of the electrons spin in order to follow the direction of the local magnetization. This yields the outgoing electrons to have a different spin direction compared to the incident ones. By conservation of the angular momentum, the flowing spins exert an equal and opposite torque on the magnetization vector. As a result, a spin polarized current can manipulate the direction of the magnetization in a ferromagnetic layer. A simple way

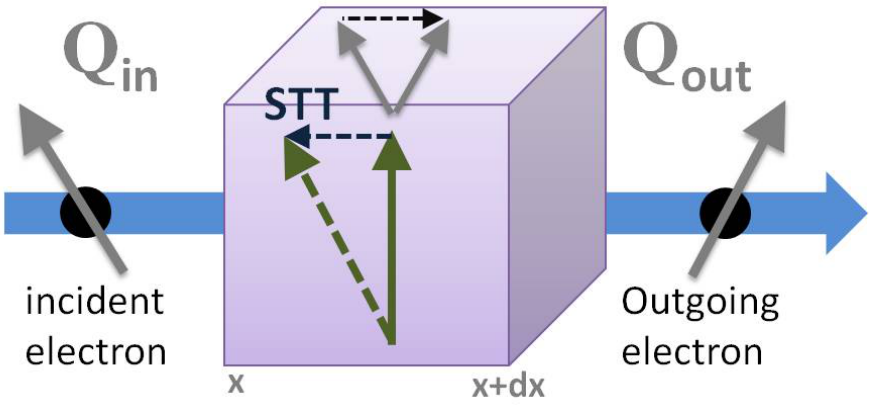

Figure 2.8: A spin polarized current passes through a ferromagnet. The interaction between the incident current and the magnetization of the layer results in a change of the spin direction for the outgoing spin electrons. The change in the spin direction between the incident and the outgoing spins give rises to a spin transfer torque on the ferromagnet.

to calculate the spin transfer torque $(\frac{dM}{dt})_{STT}$ acting on a volume (V) of the ferromagnet is to consider the net change in the flux of the spin current (N_{STT}) through a surface of that volume.

2.3.3 Adiabatic spin transfer torque

In this section we will derive the spin transfer torque for a continuous magnetization distribution. We assume the magnetization varies slowly. I.e, it changes over a length scale smaller than the characteristic length of transport, (the decoherence length, the electronic mean free path of the majority and the minority spin, and the spin flip length). In this case it is supposed that the electron spin is aligned everywhere with the local magnetization direction: the electron spin

is said to follow "adiabatically" the magnetization.
Let us consider an incoming spin current $\mathbf{Q(x)}$ at a position x flowing along the x-axis through a surface (A) of the ferromagnet. The outgoing spin current is $\mathbf{Q(x+dx)}$. The spin balance for the volume Adx during the infinitesimal time interval dt is written as:

$$N_{STT} = (\mathbf{Q(x)} - \mathbf{Q(x+dx)})Adt. \tag{2.23}$$

Due to the conservation of the angular momentum, the variation of the magnetic moment in the ferromagnet is equal to N_{STT}

$$\delta\mu = (\mathbf{Q(x)} - \mathbf{Q(x+dx)})Adt, \tag{2.24}$$

using the definition of the magnetization $M = \frac{\mu}{Adx}$ then one can write the change of the magnetization with time, i.e. the spin transfer torque, as:

$$\frac{dM}{dt} = -\frac{\mathbf{dQ}}{dx}. \tag{2.25}$$

This definition of the spin transfer torque can be generalized to 3-dimensions as:

$$\frac{dM}{dt}_{STT} = -\nabla\mathbf{Q}, \tag{2.26}$$

notice that the spin transfer torque is opposite to the spatial variation of the spin current density.
For a continuous magnetization distribution the spin current is expressed as:

$$\mathbf{Q} = -P\frac{\mu_B}{e}\frac{\mathbf{M}}{M_s}\bigotimes\mathbf{j}, \tag{2.27}$$

where $\mathbf{j}$ and $\mathbf{M}$ are the current density and the magnetization vector, M_s is the saturation magnetization P is the degree of the spin polarization.
For the basic two current model, the degree of the spin polarization is expressed in terms of the resistivities of the two conduction channels ($\rho_\uparrow$, $\rho_\downarrow$) as:

$$P = \frac{\rho_\downarrow - \rho_\uparrow}{\rho_\uparrow + \rho_\downarrow}. \tag{2.28}$$

Then the adiabatic spin transfer torque for a current density flowing along the x-direction is written as:

$$\frac{\mathbf{dM}}{dt} = +P\frac{\mu_B j}{eM}\frac{\mathbf{dM}}{dx}, \tag{2.29}$$

For a current passing along an arbitrary direction in the space, the spin torque is generally expressed as:

$$\frac{\mathbf{dM}}{dt} = -(\overrightarrow{u}.\overrightarrow{\nabla})\overrightarrow{M}. \tag{2.30}$$

where u is the effective magnetization velocity defined as $u = -\frac{\mu_B P}{eM_s}j$. The spin transfer between the current and the local magnetization is determined once the variation of the magnetization profile is known.

2.3.4 Non-adiabatic spin transfer torque

Phenomenologically, the spin polarized current is expected to exert another torque on the magnetization. This additional torque is perpendicular to the adiabatic spin transfer torque. It is known as the non-adiabatic spin transfer torque, which is described as a spatial damping of the magnetization [105]:

$$\beta u \frac{\mathbf{M}}{M_s} \times \frac{\partial \mathbf{M}}{\partial x}, \tag{2.31}$$

with β the non adiabatic coefficient.
The non-adiabatic spin transfer torque is explained based on two approaches:

- In the first approach, Zhang et Li [117] derived the non adiabatic term by computing the response of the conduction electrons to a magnetization distribution varying in space and time within the semiclassical transport theory. The non-adiabatic term originates from the mistracking between the spin of the conduction electrons and the magnetization. This mistracking depends on the the relaxation of the conduction electron spins to the local magnetization by means of spin-flip scattering.

- In the second approach, Xiao et al. [115] studied the non-adiabatic spin transfer torque by considering the length scale of the variation of the magnetization (typically the domain-wall width) is comparable to the characteristics length L of transport, without accounting explicitly for the scattering in contrary to the Zhang approach. Their results showed the non-adiabatic torque occurs when the width of the domain-wall is smaller or comparable to L. The non-adiabatic torque is found to decrease exponentially as the width of the domain wall increases.

Although, the magnitude of the β coefficient is expected to be very small (of the order of the Gilbert damping coefficient α), this small effect is able to explain the domain wall motion in the current induced domain wall motion experiments (see 2.4.2).

2.3.5 The role of the spin transfer torque in the magnetization dynamics

As we have seen in the first chapter, the magnetization dynamics in a ferromagnetic sample is described by the Landau-Lifschitz-Gilbert equation of motion. As we have seen in the previous section 2.3.2, the spin current exerts a torque on the the magnetization orientation. Hence, in the presence of a spin current, the dynamical equation should be modified to include the adiabatic and the non-adiabatic spin transfer torque terms. It is written as:

$$\frac{\partial \mathbf{M}}{\partial t} = -\gamma \mathbf{M} \times \mathbf{H_{eff}} + \frac{\alpha}{M_s} \mathbf{M} \times \frac{\partial \mathbf{M}}{\partial t} - u \frac{\partial \mathbf{M}}{\partial x} + \beta u \frac{\mathbf{M}}{M_s} \times \frac{\partial \mathbf{M}}{\partial x} \tag{2.32}$$

where the current is supposed to be along the x-axis and u is the effective spin transfer velocity defined as $u = -P\frac{\mu_B j}{eM_s}$ [104].

2.4 Experimental observation of the spin transfer torque

In this section we present some observations of the spin transfer torque in spin valves, domain walls and spin waves experiments.

2.4.1 Spin transfer torque in spin valves

In the beginning of the 90th, the giant magnetoresistance (GMR) effect [5][41] was measured in ferromagnetic (FM) multilayer stacks (FM 1 / normal metal/ FM 2). A spin valve consists of two ferromagnetic layers (FM1, FM2) separated by a non-magnetic layer. The resistance of this stack depends on the relative orientation of the magnetization between the two ferromagnetic layers. Most often it is low when the magnetization of the two layers are aligned parallel and it is high when they are aligned antiparallel. In a spin valve the current induced switching of the magnetization can be viewed as a reciprocal effect to the GMR. According to the description of the spin transfer torque phenomenon in the last section, a spin polarized current can be used to manipulate the magnetization of a ferromagnetic layer [80].

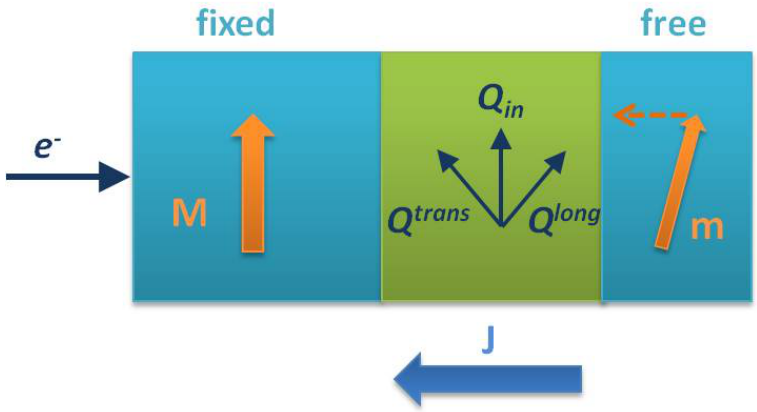

Figure 2.9: A schematic drawing of a spin valve where the electrons flow from the fixed to the free layer. The spin current exerts a torque on the magnetization m of the free layer tends to align it parallel to M.

Consider an electrical current passing through the spin valve as shown in figure 2.9 i.e electrons flowing from the FM1 to the FM2 layer. FM1 is a thick ferromagnetic layer with a hard magnetization direction **M** (the fixed layer) which serves to spin-polarize the current flowing perpendicular to the interfaces. FM2 is a thin ferromagnetic layer with a magnetization **m** (the free layer). The transmitted flow becomes spin polarized after it passes through the fixed layer. In the spacer layer, the flow conserves its spin orientation parallel to **M** with a non zero spin current. Let us assume the magnetization **m** of the FM2 is not aligned parallel to the magnetization **M** of the FM1 layer. The spin current Q can be decomposed into a longitudinal and a transverse component.

The longitudinal component passes through the FM2 layer and the transverse component is absorbed by the interface. The transverse component transfers angular momentum to **m**. The transfer of the angular momentum exerts a torque on **m** and it acts to pull **m** towards the direction of the magnetization of the fixed layer. Consider now an electrical current such as the electrons flow from the free to the fixed layer as shown in figure 2.10. The electrons coming from the free layer are reflected back into it, and the spin polarized current results from the reflected electrons. In the spacer the magnetization of the spin current **Q** is antiparallel to **M**. As in the preceding case, angular momentum is transferred from the transverse component of **Q** to **m**. The resulting torque pulls out the magnetization of the free layer. Therefore this current polarity destabilizes the parallel configuration between the two layers and it stabilizes the antiparallel configuration.

Slonczewski calculated the spin transfer torque on the free layer magnetization

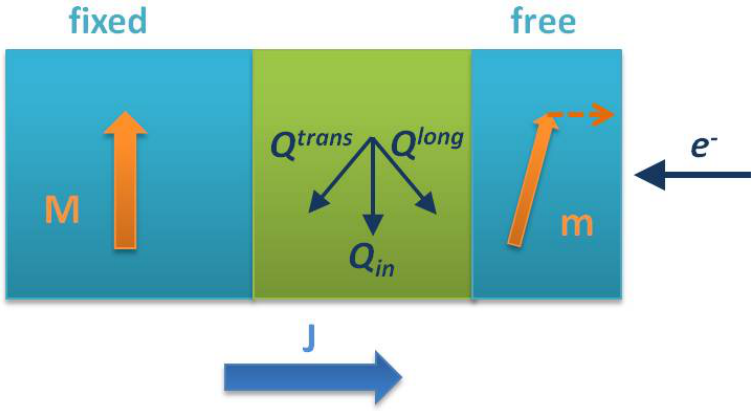

Figure 2.10: A schematic drawing of a spin valve where the electron flow from the free to the fixed layer. The spin current exerts a torque on the magnetization m of the free layer tends to align it antiparallel to M.

m due to the misalignment angle θ with the fixed layer magnetization **M** as [97]:

$$\frac{\partial \mathbf{m}}{\partial t} = g(\theta)\frac{I}{e}\mathbf{m} \times (\mathbf{m} \times \mathbf{M}) \tag{2.33}$$

where $g(\theta)$ depends only on the polarization of the spin current $P = \frac{I_\uparrow - I_\downarrow}{I_\uparrow + I_\downarrow}$ in the spacer. It is written as:

$$g(\theta) = [-4 + \frac{(1+P)^3(3+mM\cos\theta)}{4P^{3/2}}]^{-1} \tag{2.34}$$

Equation-2.33 shows the torque direction depends essentially on the sign of the injected current. It is zero once the magnetization directions in the two layers are aligned parallel or antiparallel to each other.

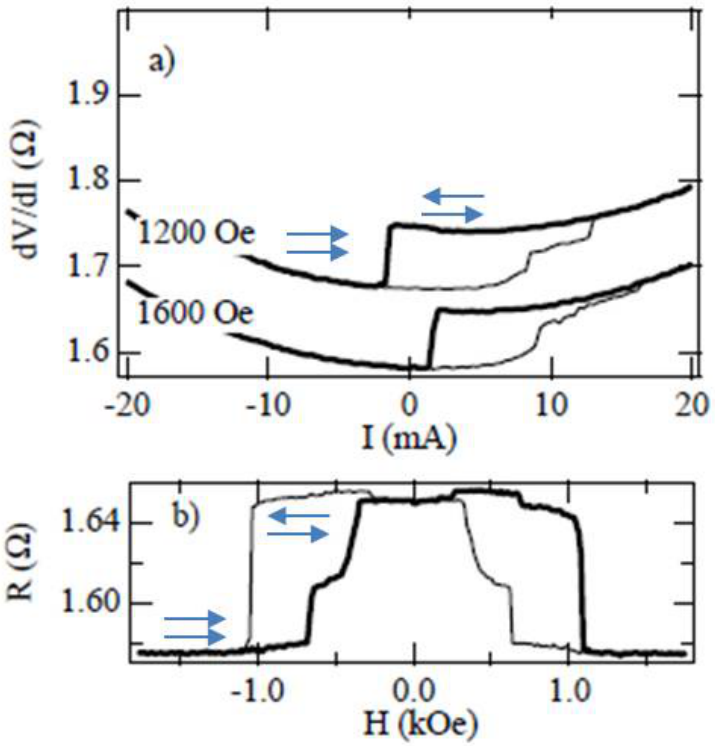

Figure 2.11: dV/dI of a pillar device (Co/Cu/Co) exhibiting hysteretic jumps as the current is swept. The current sweep begins at zero; light and dark lines indicate increasing and decreasing current, respectively. (b) Zero-bias magnetoresistive hysteresis loop for the same sample. The blue arrows indicate the direction of the magnetization in the two FM layers. The image is taken from [57].

2.4.2 Current induced domain wall motion

Another manifestation of the spin transfer torque phenomenon is the current induced domain wall motion. Originally, three decades ago, Berger asked the question: What would be the effect of the electrical current on a stationary magnetic domain wall? Theoretically, he predicted that a spin current exerts a torque on the domain which tends to displace or to distort the domain wall. Due to the many technological difficulties it was difficult to check this idea until recently. One of the first domain wall study performed in a nanowire was done by Yamaguchi et al. [116], it will be presented in this paragraph.
The study was performed in a 10nm thick permalloy nanowire with an L-shape. A magnetic domain wall is injected in the nanowire, with a head to head configuration. Sequential current pulses at a constant current density are applied through the wire. A magnetic force microscopy images was taken after each pulse as shown in the figure-2.12. The MFM images show a sequential displace-

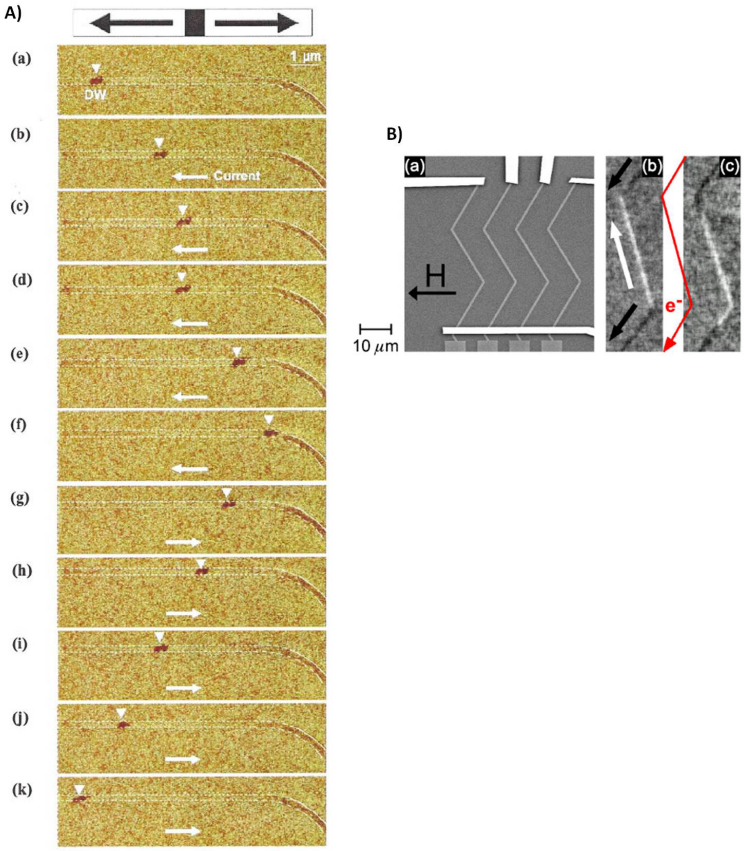

Figure 2.12: A) Successive MFM images with one pulse applied between consecutive images. The domain wall motion is viewed in the dark contrast and the current direction is shown by the white arrows. The image is taken from the reference [116]. B) Shows the domain wall motion in a zigzag wire. The image is taken from the reference [59].

ments of the domain wall from its original position, and the displacement of the domain wall is opposite to the current direction. The measurement is repeated with a tail to tail domain wall and the result showed the motion of the domain wall is also opposite to the direction of the applied current. This observation excludes the hypothesis of the Oersted field contribution of the domain wall motion. The displacement of the wall is almost proportional to the pulse duration and the domain wall velocity increases as the current intensity increases, which is in agreement with the effect of the spin transfer torque.
Other experimental works which used spin polarized scanning electron microscopy in zigzag nanowires [59] and x-ray microscopy in curved nanowires [72] showed a distortion of the domain wall configuration after many repetitive current pulses.
The results of a micromagnetic simulation by Thiaville et al. [104] of the domain wall motion due to a spin polarized current using the adiabatic spin transfer torque 2.30 suggested that the phenomenon should be observed with a current density ten times higher than the density used in the experiments. This discrepancy motivated the introduction of another spin transfer torque (the non-adiabatic torque of equation-2.31), which was shown to be likely to explain the measured domain wall velocities.

2.4.3 Current induced spin wave Doppler shift

Another consequence of the spin transfer torque is the current-induced change of the frequency of spin waves (spin-wave Doppler shift). In the following paragraphs, we review the theoretical predictions of this effect, we show how it can be deduced from the expression of the spin transfer torque given in 2.3 and we review the experimental works published so far.

Theoretical predictions:

In the 1960's Lederer and Mills [62] suggested that a Doppler shift could occur for the spin waves of a metal ferromagnet subjected to an electrical field. A spin wave propagating in a reference frame $\mathbf{R}^{'}$ has a plane wave form as:

$$m^{'}(x^{'}) = m_0 e^{i(w_0 t - k_0 x^{'})}. \tag{2.35}$$

In the lab frame $\mathbf{R}$ the effect of the electrical field can be seen as a global drift of the reference frame (linked to the electrons of the metals) with a velocity v_d. The coordinates of the lab frame $\mathbf{R}$ can be expressed in terms of the coordinates of $\mathbf{R}^{'}$ as: $x = x^{'} + v_d t$ as shown in the figure 2.13. Then the spin wave in $\mathbf{R}$ is written as:

$$m(x) = m_0 e^{i(w_0 t - k_0 x + k_0 v_d t)}, \tag{2.36}$$

with an apparent frequency $\omega_0^{'} = \omega_0 + \delta\omega$, where the Doppler frequency shift writes

$$\delta\omega = k_0 . v_d. \tag{2.37}$$

Later, Bazaliy et al. [11] derived a continuum description for the magnetization of a ferromagnet in the presence of a spin-polarized current (i.e with spin transfer torque). Their results showed that a spin current induces a shift in the spin wave spectrum. In 2004 Fernandez-Rossier et al. [32] studied the influence

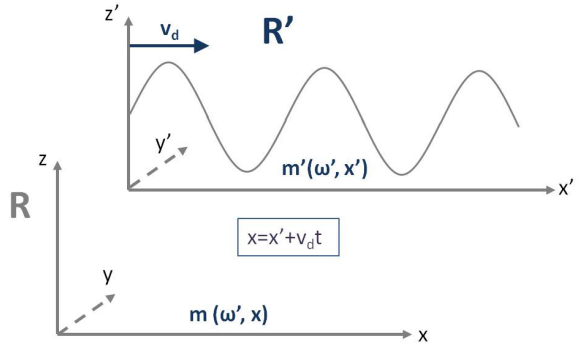

Figure 2.13: An illustration of the current induced spin wave Doppler shift [110].

of the DC electrical current on the collective magnetization dynamics in a ferromagnet based on different approaches (classical Galilean invariance, microscopic description starting from the Hubbard model, spin transfer theory). All these approaches showed that the effect of a uniform current is to introduce an extra term in the spin wave spectrum which is proportional to the current density **J** and to the wavevector **q**:

$$\delta\epsilon(\mathbf{q}) \propto \mathbf{q}.\mathbf{J}. \tag{2.38}$$

Coupling between the spin transfer torque and a spin wave:

Let us now investigate the effects of the spin transfer torques of equation 2.32 on a spin-wave. The spin wave is a stationary system with a defined frequency ω and wavevector k. It is written in the form of a plane wave as ($\mathbf{m} = \mathbf{m}_0 e^{i(\omega t - k.x)}$). Therefore, its spatial and temporal evolution are simply known as ($\frac{\partial m}{\partial x} = -ikm$, $\frac{\partial m}{\partial t} = i\omega m$). Then the linearized equation 2.32 can easily be rewritten as:

$$i\omega\mathbf{m} = -\gamma(\mathbf{m}\times\mu_0\mathbf{H_0}+\mathbf{M_0}\times\mu_0\mathbf{h})+\frac{i\omega\alpha}{M_s}\mathbf{M_0}\times\mathbf{m}+iku\mathbf{m}-ik\beta u\frac{\mathbf{M_0}}{M_s}\times\mathbf{m} \tag{2.39}$$

One could remark that the adiabatic and the non-adiabatic spin transfer torque are accounted by the following substitution:

$$\omega \longrightarrow \omega + u.k \tag{2.40}$$

$$\alpha\omega \longrightarrow \alpha\omega - \beta u.k. \tag{2.41}$$

Figure 2.14 shows an illustration of the spin transfer torque effects on the precessing magnetization **m**. The adiabatic torque tends to modify the precessional frequency, as shown by the dark blue arrow. The non-adiabatic torque tends to modify the damping of the magnetization, as shown by the gray arrow.

Experimental observations of the CISWDS:

In 2008 our group in Strasbourg was the first to set an experimental design for the current induced spin wave Doppler shift. Figure-2.15 shows the

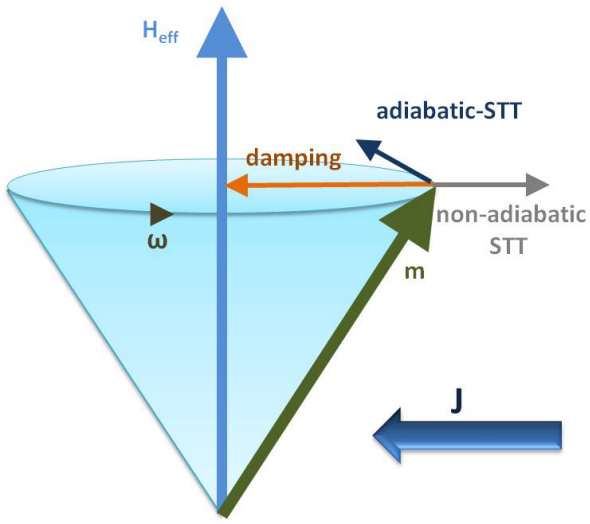

Figure 2.14: A schematic picture showing the effect of the spin transfer torque on the precession of the magnetization. The orange arrow represents the Gilbert damping coefficient. The dark blue and the gray arrows corresponds to the adiabatic and the non-adiabatic spin transfer torques respectively.

device used for the experiment. The spin waves are excited in the magnetostatic forward volume wave configuration in a permalloy stripe using micro-sized antennas. The spin wave propagates with a wavevector k and at a pulsation ω_0 along the stripe. A DC current (I) is sourced along the propagation direction (k) of the spin wave. The flow of the spin polarized electrons exerts an angular momentum on the propagating spin waves. Due to the spin transfer torque phenomenon, a frequency shift is measured for the propagating spin wave as shown in figure-2.16. The frequency shift is observed to increase linearly with the applied dc current. Based on the Doppler shift deduced from the adiabatic spin transfer torque term: ($\delta\omega = k.u$ where $u = P\frac{\mu_B j_c}{eM_s}$), the degree of the spin polarization of the electric current is extracted. The degree of the spin polarization in a 20 nm permalloy film is measured to be about 0.5 [111].
Later the current induced spin wave Doppler shift was measured by two other groups in the frequency domain at low temperature [118] and in the time domain [92]. Both experiments use the magnetostatic surface wave configuration. The low temperature measurements showed the polarization to increase from 0.58 to 0.75 between 300 to 80K as shown on the figure 2.17. Current induced spin wave Doppler shift measurements were also performed on other systems: $(CoFe)_{1-x}Ge_x$ [119] and $(Ni_{0.8}Fe_{0.2})_{1-x}Gd_x$ [106]. The results of the polarization measurements as a function of the impurity concentration are shown in figure 2.18.

Non-adiabatic spin transfer torque:

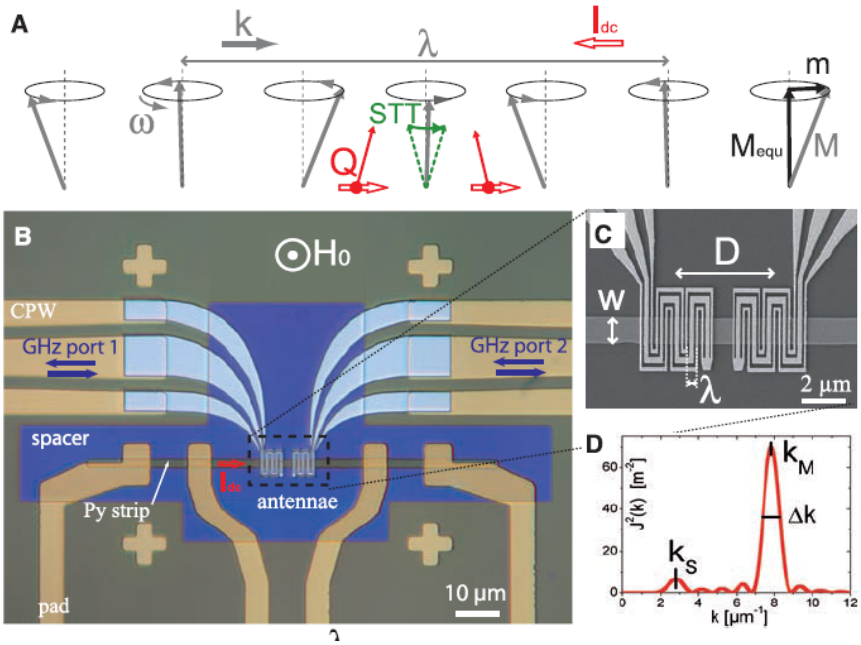

Figure 2.15: The experimental device for the current induced spin wave Doppler shift experiment. The image is taken from [111].

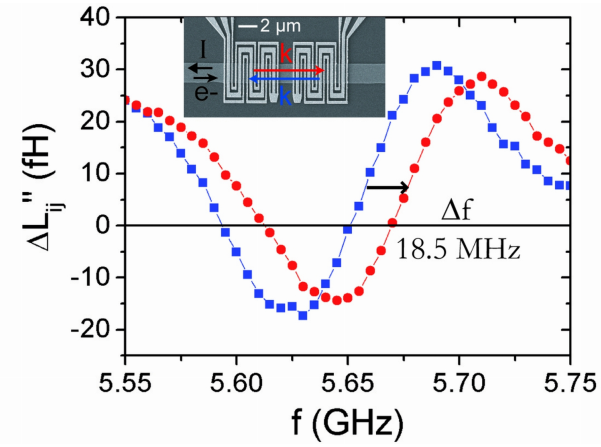

Figure 2.16: The current induced frequency shift measured between two opposite propagating signals.

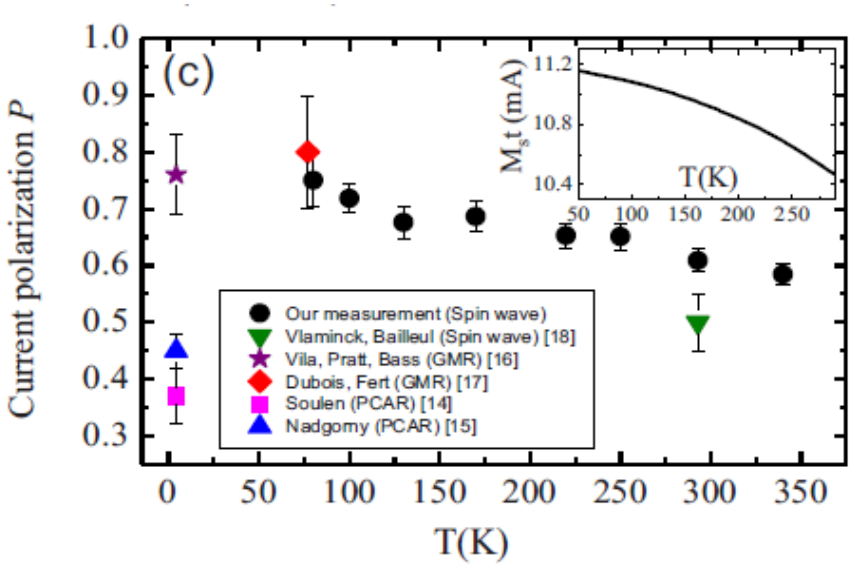

Figure 2.17: The degree of the spin polarization of the electrical current versus temperature extracted from the CISWDS measurements. The image is take from the [118].

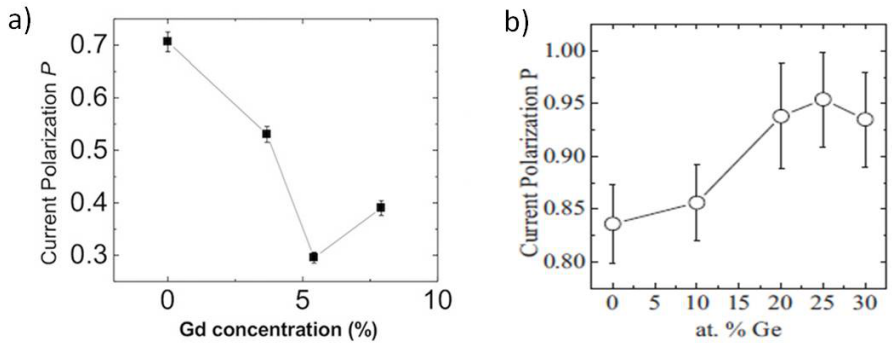

Figure 2.18: The degree of the spin polarization of the electrical current versus impurities concentration in a)$(Ni_{0.8}Fe_{0.2})_{1-x}Gd_x$ and b)$(CoFe)_{1-x}Ge_x$. The images are taken from [106] and [119] respectively.

In 2009 Seo et al. [95] studied theoretically the effect of the dc current on the amplitude of a propagating spin wave. Their results indicates that the attenuation length of the spin wave increases when the spin wave and the electron are moving in the same direction. This enhancement in the attenuation was explained as a direct impact of the non adiabatic spin transfer torque. As it was discussed in the section 2.3.5, the non adiabatic term could be seen as an additional spatial damping of the propagating waves. In 2012, Sekiguchi et al. [92] detected a change in the amplitude of the propagating wave when the dc current is applied. The attenuation in the amplitude of the signal is analyzed in the frame of the non-adiabatic spin transfer torque. Solving the LLG equation including the spin transfer torque terms, Sekiguchi et al. derive the following formula for the non-adiabatic parameter beta:

$$\beta = -\frac{\alpha(\omega_0 - u_0 k)(\omega/k)}{(2\pi\gamma M_s)^2 d\exp(-2kd)} + \frac{(\omega_0 - u_0 k)u_0 + (2\pi\gamma M_s)^2 d\exp(-2kd)}{\gamma(H_i + 2\pi M_s)u_0 k}\frac{\ln(A_{STT})}{x} \tag{2.42}$$

where x, k, d, and M_s are the propagation distance of the spin wave, the wavevector, the film thickness, and the saturation magnetization. A_{STT} is the normalized spin wave amplitude defined as $A(u \neq 0)/A(u = 0)$. They estimate the measured beta to be between 0.02 and 0.03. A general believe in the community is that the beta term and the Gilbert damping term (α) are of the same order of magnitude. However the microscopic origin of this term is still controversial and its value is still not known precisely.

Conclusion

This chapter provides a sufficient background to understand and to analyze the role of the surfaces scattering of the spin polarized transport using the current induced Doppler shift experiment.

Chapter 3

Magnetic and electrical characterization of thickness series of Permalloy thin films

For thicknesses in the nanometer range, devices become very sensitive to surface effects. In thin films of the transition metal ferromagnets (Fe, Co, Ni) the surfaces can influence significantly both electrical and magnetic properties. For a better understanding of the permalloy thin films used in this thesis, we performed various structural, electrical, and magnetic characterizations onto thickness series of such films. This chapter describes the results of these studies.
In section-§3.1 the samples and their structural characterization are presented. In section-§3.2 the static magnetic properties of the thin films are discussed. In section-§3.3 the effects of the surfaces on the electrical properties of the thin films are studied. In section-§3.4 a detailed study of the effects of the surfaces on the magnetization dynamics is described based on ferromagnetic resonance measurements. We end the discussion in section-§3.5 with supplementary measurements and a discussion aiming at identifying the origin of the observed magnetization damping.

3.1 Sample and structure

We deposit series of permalloy ($Ni_{80}Fe_{20}$) thin films of different thicknesses (t) ranging from 4 to 160 nm. The permalloy films were sputtered using a magnetron sputtering machine available at the IPCMS. The sputtering chamber has a space to place 9 substrates on the sample holder and to install 6 different targets. The sample holder is automatically rotated over a specific target to deposit the desired material. Four series of the permalloy thin films sandwiched with aluminium oxide Al_2O_3 layer are sputtered, the parameters of each series are mentioned in the table-3.1. The films were deposited using the DC mode for the permalloy and the RF mode for the Al_2O_3. The permalloy is sputtered using a face to face target with a deposition rate of 0.25 nm/sec at a current of 800 mA and a power of 500 Watt. The Al_2O_3 is sputtered using a circular target with a deposition rate of 0.04 nm/sec and at a power of 150 Watt. The base vacuum

is of the order of a few 10^{-8} mbar. The deposition was done under pure argon at a pressure of 2.10^{-3} mbar with a flow of about 15 sccm.

Series	composition	thickness (nm)
S1	SiOx/ Al_2O_3 8 nm /Py (t nm)/Al_2O_3 8 nm	[4-160]
S2	SiOx/Py (t nm)/$Al_2O_3$8 nm	[4-160]
S3	Si/Al_2O_3 21 nm /Py (t nm)/Al_2O_3 5 nm	[6-40]
S4	Si/Al_2O_3 21 nm /Py (t nm)/Al_2O_3 5 nm	[6-40]

Table 3.1: The composition and the thickness of the 4 series of permalloy thin films.

The layers are sputtered on (001) intrinsic silicon substrates (resistivity ($> 100\Omega cm$). For the series (S1, S2) thermally oxidized substrates (oxide thickness 300 nm) were used. The upper Al_2O_3 layer was deposited to protect the permalloy surface from oxidation. The lower Al_2O_3 layer is used since it is a better heat conductor than the thermal silicon oxide layer. This step will be helpful for the current induced spin wave Doppler shift measurements. The four series were used for the electrical and magnetic characterization.

3.1.1 Structural characterization

A sample of Si/Al_2O_3 (12 nm)/Py (10 nm)/ Al_2O_3 (12 nm) has been studied using a transmission electron microscope for a structural characterization. Images both in a plane view and in a cross view of the sample were taken. The cross view images indicates that the measured film thickness is 10 nm, in agreement with the nominal deposited thickness. It also shows that the interfaces between the permalloy and the Al_2O_3 are very smooth with negligible roughness as shown in figure-3.1. The plane view images indicate that the film is polycrystalline without showing a well defined texture.

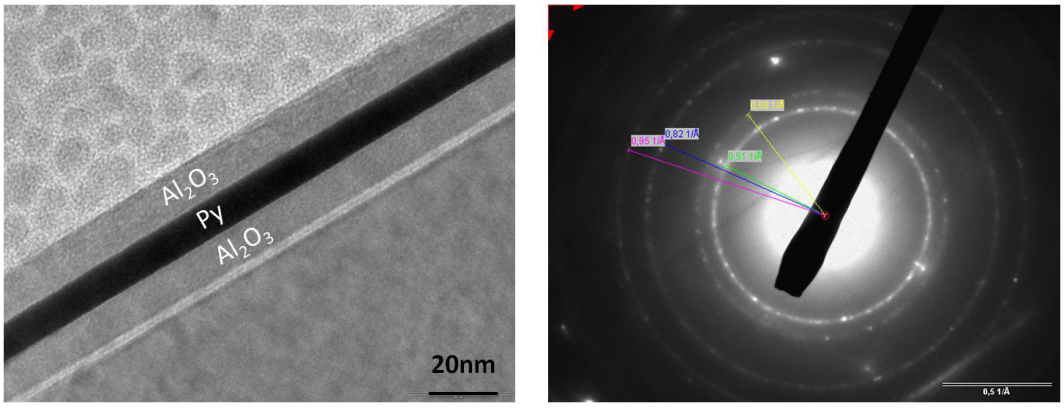

Figure 3.1: Transmission electron microscope images a) Cross view. b) Diffraction image for the plane view: Sample Si/Al_2O_3 (12 nm)/Py (10 nm)/ Al_2O_3 (12 nm).

3.2 Static magnetic characterization

For the magnetic characterization of the thin films superconducting quantum interference device (SQUID) and alternating gradient force magnetometer (AGFM) measurements are performed. Hysteresis loops for all the samples of S2 series were measured along the easy and hard axis using the AGFM. The easy axis is oriented parallel to the normal of the targets of the face to face magnetron. The measurements show a coercive field $\mu_0 H_c = 0.1$ mT along the easy axis of the film, and an in-plane anisotropy $\mu_0 H_K = 0.5$ mT along the hard axis as shown in figure-3.2. The SQUID measurement are performed at room temperature for

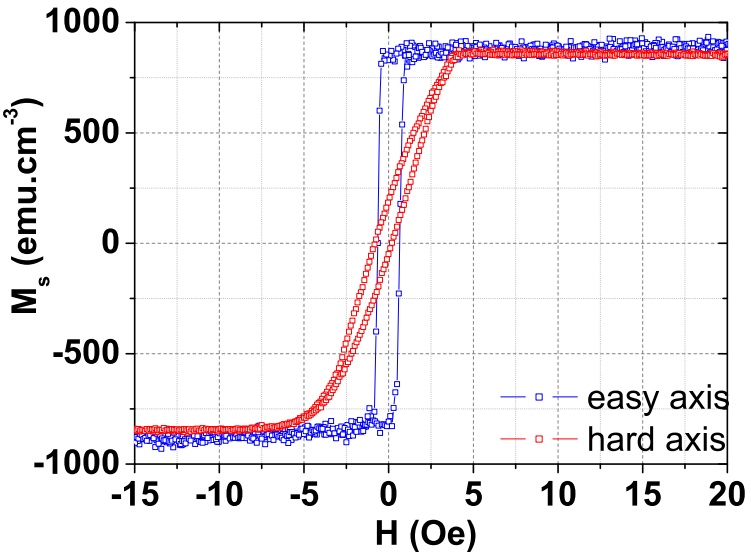

Figure 3.2: The hysteresis loop at room temperature for the 80 nm film from the S2 series. The applied field is oriented along the easy (blue curve) and the hard axis (red curve). It indicates a coercive field of 0.1 mT, and an in-plane anisotropy of 0.5 mT.

the sample of the S1 and S2 series. Figure-3.3 shows the variation of the magnetization density as a function of the film thickness. The magnetization density increases gradually with the thickness. The magnetic moments per unit surface (μ_s/S) is plotted in the figure-3.4. μ_s/S increases linearly with the thickness. It writes as:

$$\frac{\mu_s}{S} = A + M_s \times t$$

From the slope, the saturation magnetization $\mu_0 M_s$ is deduced to be equal to 0.96 T. One could notice a zero μ_s/S for a finite thickness of the order of 1.1 nm. This magnetic dead layer t_{dead} could be due to an oxidation of the permalloy surfaces during the deposition [35] or due to the inter-diffusion of permalloy and Al_2O_3 layers. We define the magnetic thickness t_{mag} of the films as: $t_{mag} = t_{nominal} - t_{dead}$, where $t_{nominal}$ is the nominal deposited thickness.
For a 40 nm film from the S1 series we follow the variation in the hysteresis loop at different temperatures as shown in the figure-3.5. One can notice a change in

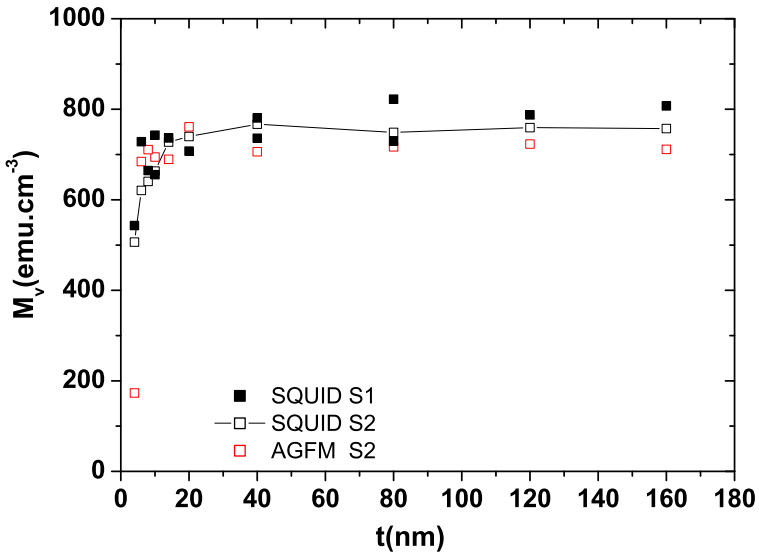

Figure 3.3: The variation of the magnetization density as a function of the thickness for the S1 and S2 series. The measurements were performed at room temperature (300K) and under a weak field, using the SQUID and AGFM experiments.

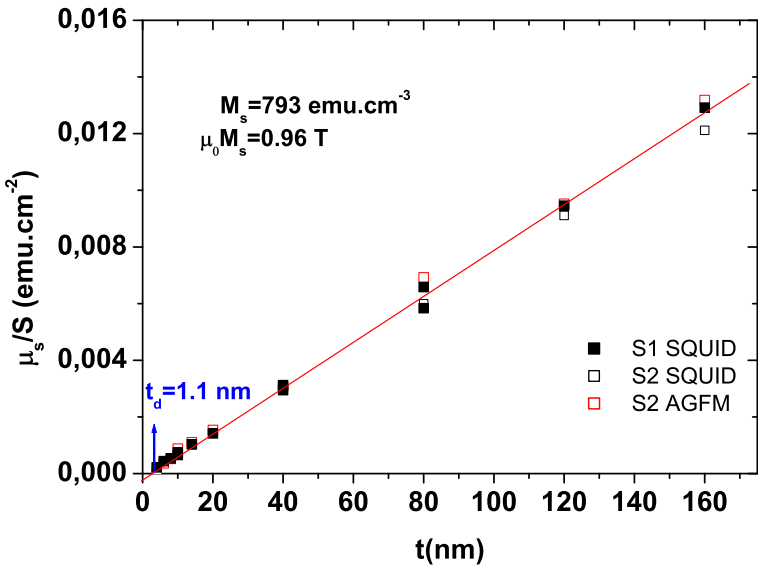

Figure 3.4: The variation of the magnetization per unit surface of the S1 and S2 series as a function of the film thickness. The measurements show the saturation magnetization of the films is about 0.96 T and it shows an interfacial magnetic dead layer with a thickness $t_{dead} = 1.1$ nm.

the coercive field with temperature, (increases at low temperature). At 2 K a shift of the hysteresis cycle of about 1.5 mT is measured. This is attributed to an effect of exchange bias which could be due to a coupling of the ferromagnetic film to an antiferromagnetic layer. The same behavior was observed for a film of 8 nm thickness.

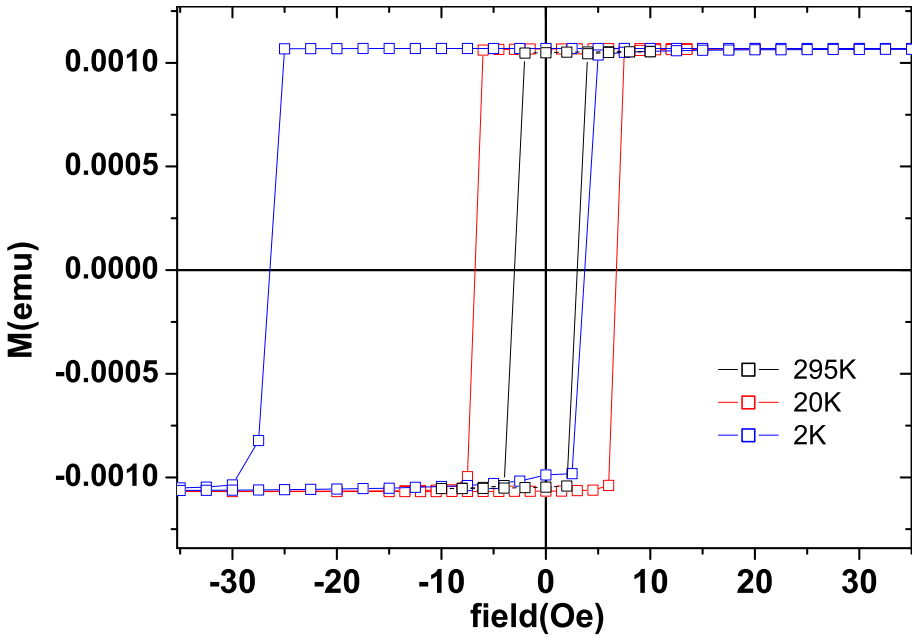

Figure 3.5: The hysteresis loop for the 40 nm film at different temperatures. The coercive field increases as the temperature decreases. In addition a shift of the hysteresis loops of about 1.5 mT is observed below 20 K.

3.3 Electrical resistivity

The resistivity of bulk metals is mainly due to the scattering of the electrons by phonons, lattice imperfections, and grain boundaries. In confined geometries such as thin films, the surfaces contribute to the resistivity when the electron mean free path is comparable to the film thickness. In this section we aim to study the electron surface scattering. Carrying out a thickness dependent study, the bulk and the surfaces contributions to the electrical resistivity are separated.

We perform resistivity measurements at room temperature for the 4 series of permalloy thin films using the Van der Pauw (VdP) method. This method measures the sheet resistance (R_s) of a sample with an arbitrary shape. VdP method can be applied for a sample verifying the following conditions:

- The film thickness should be homogeneous over the entire sample.
- No holes should exist in the surface of the sample.
- The contacts of the needles should have a very small dimension.

Consider a sample with a square dimension labeled as ABCD, two successive measurements of the resistance were done: $R_{AB,CD}$, and $R_{BC,DA}$. The resistance $R_{AB,CD}$ is measured with the current entering through the contact A and leaving through the contact B, where the potential measured is $V_D - V_C$. For $R_{BC,DA}$, the current passes through the contacts B and C, and the potential measured is $V_A - V_D$. We obtain the measured sheet resistance (R_s) of the sample from the following relation [108]:

$$\exp(-\pi R_{AB,CD}/R_s) + \exp(-\pi R_{BC,DA}/R_s) = 1. \tag{3.1}$$

The sheet resistance is measured for a piece with a square shape of 3×3 mm dimensions cut from the thin films, and we deduce the resistivity (ρ) of each film using the relation: $\rho = R_s \times t$.

The resistivity of the films increases as the film thickness decreases as shown in figure-3.6. The resistivity of the films increases from 26 $\mu\Omega.cm$ for the 160 nm film to 77 $\mu\Omega.cm$ for the 4 nm film. Because we do not expect a major change of the film structure with the film thickness, most of this change is attributed to an additional contribution to the resistivity due to the electron-surface scattering. Using the Fuchs-Sondheimer theory described in 2.2.1 one can determine the bulk resistivity and the electronic mean free path. We calculate numerically the resistivity from equation 2.19 with the assumption that $\rho_B = 1/\sigma_0$, p, and ℓ are thickness independent. Our experimental data are reproduced well by the curves corresponding to p=0 and p=0.5 as shown in the figure-3.6 with a bulk resistivity ρ_B equal to 26 $\mu\Omega.cm$. The electronic mean free path is found to be: $\ell = 11$ nm with p=0, and $\ell = 25$ nm with p=0.5. Note that the choice of p is arbitrary as the thickness dependence of the resistivity depends mostly on the product $(1-p)\ell$ (see equation 2.21). We also performed a simple linear fit of the data of the form $\rho = \rho_B(1 + B/t)$, with the bulk resistivity $\rho_B = 26$ $\mu\Omega.cm$ and B= 5.15 nm. Using equation 2.21 we deduce the mean free path to be: $\ell =$ 13.7 nm with p=0, and $\ell = 27.5$ nm with p=0.5 from this simple linear fit.

We also performed the Van der Pauw measurements at variable temperature down to 6K, using a helium cryostat. This was done for the film with thicknesses

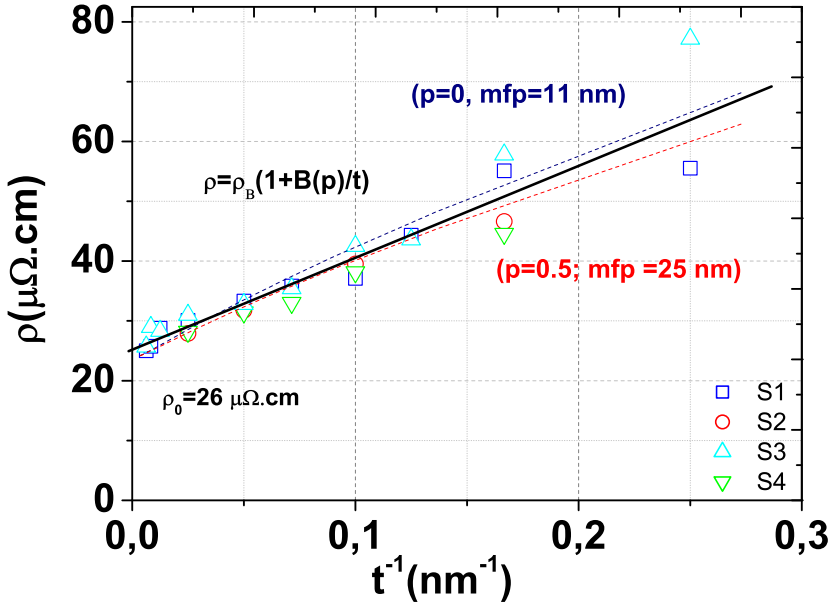

Figure 3.6: The variation of the resistivity for the 4 series of the permalloy as a function of the inverse of the film thickness. The measurements were done with 1 mA current for a piece of a sample with a square dimension of 3×3 mm. The dotted line shows the results of fitting the resistivity to the Fuchs-Sondheimer model. The red line corresponds to the (p=0, ℓ= 11 nm) and the blue line corresponds to (p=0.5, ℓ= 25 nm), with the bulk resistivity ρ_B =26 $\mu\Omega.cm$. The solid black line shows a linear fit of the results.

(6, 10, 20, and 80) nm belonging to the S1 series. Figure-3.7 shows the variation of the resistivity for each film as a function of the temperature. The measured resistivity increases with the temperature. One can extract a residual resistivity ρ_0 and a temperature dependent resistivity. The temperature dependence is well reproduced by a quadratic law: $\rho = \rho_0 + A.T^2$. Performing a quadratic fit of the data one can extract the A and the residual resistivity for each film thickness. The A parameter is found to be thickness independent with a value 1.6×10^{-4} $\Omega.cm.K^{-2}$. Figure-3.8 shows the variation of the residual resistivity as a function of the inverse of the thickness (t^{-1}). The residual resistivity increases as the thickness decreases, it varies from 15.2 $\mu\Omega.cm$ for the 80 nm film to 42.4 $\mu\Omega.cm$ for the 6 nm film. The temperature contribution of the resistivity can be attributed due to the scattering of the electrons by the phonons and magnons. The bulk extrapolation of the residual resistivity is associated with the scattering of electrons by the alloy disorder and by grain boundaries. The variation of the residual resistivity with the thickness is associated only to the electron-surface scattering.

A comparison between the measured values and the values from literature indicates that the permalloy films have typical electrical characteristics[81]. For instance, the measured bulk resistivity (26 $\mu\Omega.cm$) is in good agreement with

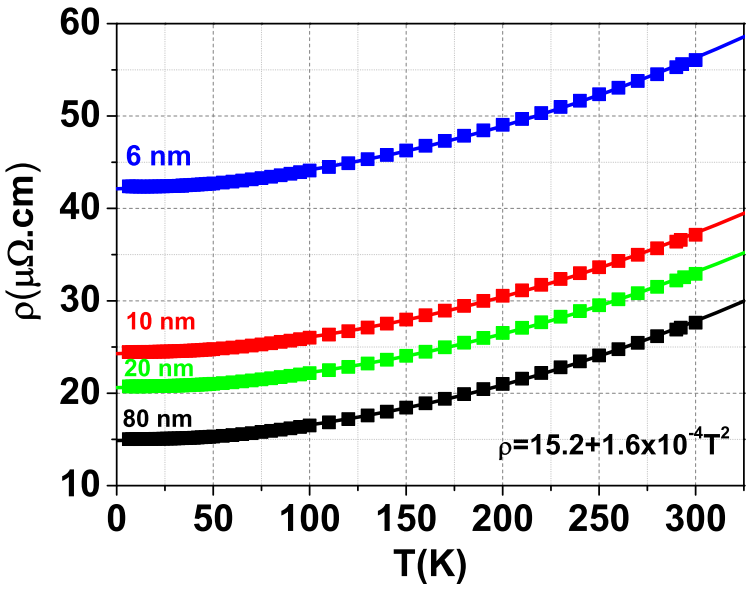

Figure 3.7: The variation of the resistivity as a function of the temperature for four different samples belonging to the S1 series. The resistivity is written as a residual resistivity and a temperature dependent resistivity.

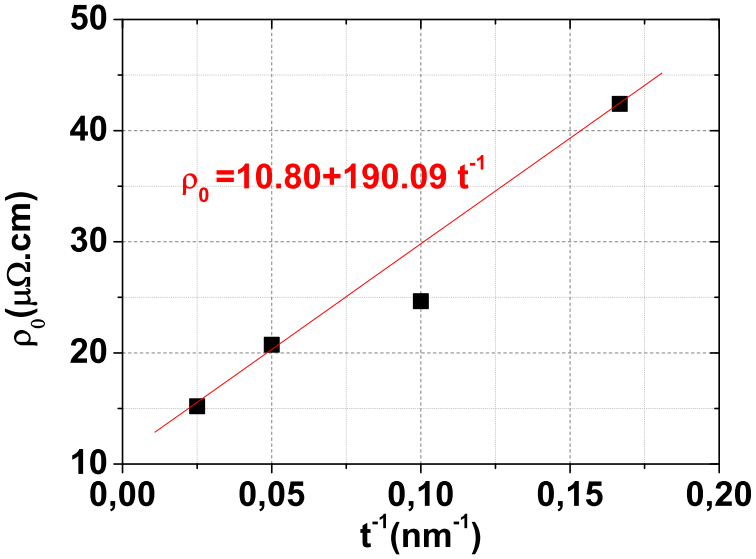

Figure 3.8: The variation of residual resistivity versus t^{-1} obtained from the low temperature measurements. The bulk residual resistivity value is = $10.8\mu\Omega.cm$

the values deduced from film thickness dependence 14-24 $\mu\Omega.cm$ [52] [67] [77] and with the value $14.9\mu\Omega.cm$ measured for bulk $Ni_{83}Fe_{17}$ [69]. The estimated

mean free path 11 nm is in agreement with the reported values in the range 9.6-23 nm [52][67]. The bulk residual resistivity 10.8 $\mu\Omega.cm$ is comparable to the values deduced from film thickness dependence in the range 14-22.3 $\mu\Omega.cm$ [23][52] and to the value 4.75 $\mu\Omega.cm$ in bulk $Ni_{83}Fe_{17}$ [69]. The temperature dependence parameter A found to be 1.6×10^{-4} is comparable to the 1.3×10^{-4} measured by [23].

3.4 Ferromagnetic resonance

At the nanometer scale, the surfaces and the interfaces are expected to influence the magnetic properties of the thin films. The surfaces and the interfaces can contribute to the magnetization relaxation, in particular through extrinsic processes such as 2-magnon scattering or spin pumping [37]. Although the magnetization relaxation is phenomenologically described with the Gilbert damping coefficient α, the underlying physical relaxation processes are still unclear. Here, we will study the surface effects on the magnetization dynamics of permalloy layers in contact with insulating Al_2O_3 layers. Sets of ferromagnetic resonance (FMR) experiments are performed as a function of the film thickness t.
The dynamics in the 4 series of the permalloy thin films are measured using a FMR setup with a X-band cavity (f$\sim$ 10 GHz). For each film, a $5 \times 3mm$ piece is cleaved, and it is glued on a teflon piece inserted into a quartz tube. Then the quartz tube is inserted in the center of the microwave cavity (TE 102) through a goniometer. The static magnetic field is applied in the film plane along the easy axis of the film. The experiment is carried out at a fixed frequency, the frequency of the cavity, while the magnetic field is varied slowly. The measured signals represent the derivative of the power absorbed by the sample with respect to the magnetic field $\frac{\partial P}{\partial H}$ as a function of the magnetic field, as shown in figure-3.10. The resonance field and the peak to peak line width ΔH_{pp} are extracted either directly from the measured signals, or by integrating the FMR signal and then performing a Lorentzian fit. The Lorentzian fit is quite good for most of the samples as shown in figure-3.10.

3.4.1 Resonance field

In thin films, the surface atoms introduce a surface anisotropy due to the breaking of their orbital symmetry. Hence the first effect of the surface is to introduce an additional surface energy term to the total magnetic energy of the system. We aim to deduce the surface anisotropy for the 4 series from thickness dependent ferromagnetic resonance measurements [89].
Figure-3.11 shows the variation of the resonance field as a function of the film thickness. The resonance field increases as the film thickness decreases, this is a common behavior for the 4 series. The samples from the series (S1, S3 and S4) have almost the same resonance field, whereas the samples of the S2 series for which Py is sandwiched between SiO_x and Al_2O_3 shows a higher resonance field than the other series for which Py is sandwiched between the two Al_2O_3 layers.
Qualitatively this behavior is explained as follows: For thick films, the demagnetizing field tends to keep the magnetization in the film plane. However for thinner films the surface anisotropy competes against the demagnetizing field

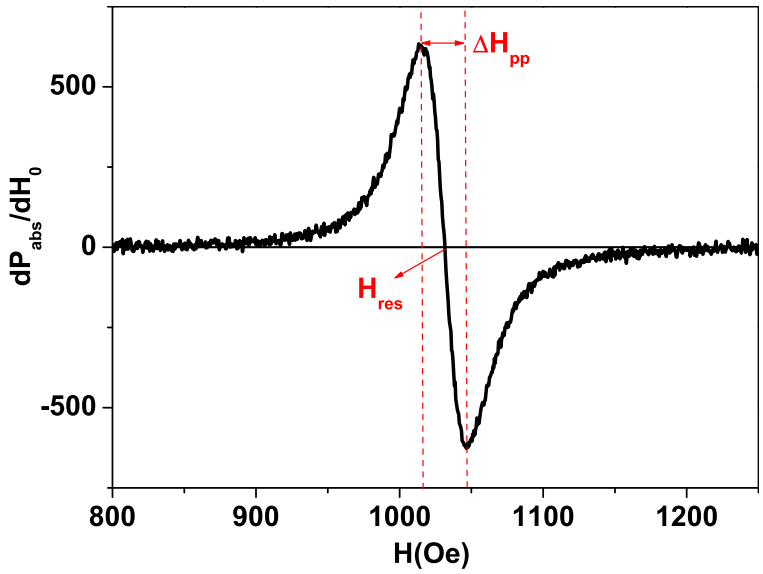

Figure 3.9: The measured FMR signal shows the variation of the $\frac{\partial P}{\partial H}$ as a function of the applied magnetic field. The signal is for a 10nm thin film. The resonance field and the peak to peak linewidth are indicated in the figure.

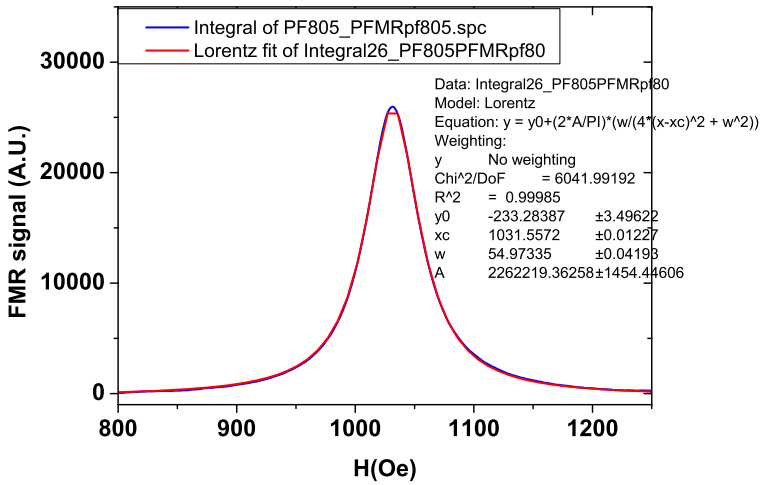

Figure 3.10: A lorentzian fit of the integrated FMR signal indicates a resonance field H_{res} = 1031 Oe and a full width at half maximum ΔH= 54.9 Oe for the 10 nm film.

and tends to change the alignment of the magnetization. The resonance field becomes higher for thinner film to conserve an in-plane orientation of the magnetization.

Quantitatively, we can use the resonance condition derived in section 1.2.2.2.

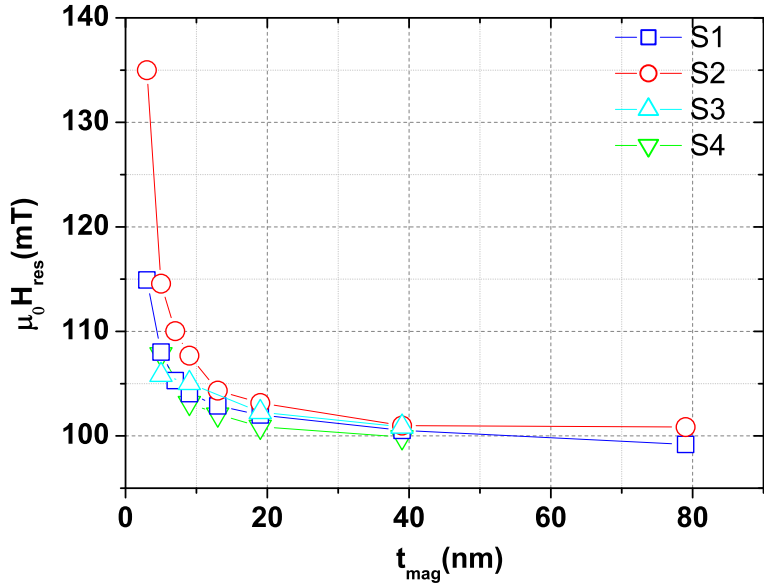

Figure 3.11: The variation of the resonance field as a function of the magnetic film thickness for the different samples of the 4 series of permalloy.

In the presence of a surface anisotropy oriented normal to the film, and for an external field oriented in the plane of the film one obtains:

$$\omega_{res} = \gamma\mu_0\sqrt{(H_{res} + M_{eff})H_{res}}, \tag{3.2}$$

where γ is the gyromagnetic ratio and the effective magnetization is defined as:

$$M_{eff} = M_s - \frac{2K_s}{\mu_0 M_s t} \tag{3.3}$$

Using equation-3.2 and assuming $\gamma/2\pi$= 30 GHz/T, the effective magnetization for each film thickness is determined. Figure-3.12 shows the effective magnetization has a linear dependence on the inverse of film thickness. From this linear dependence and using equation-3.3 one can deduce the saturation magnetization M_s and the surface anisotropy K_s. Table-3.2 displays the results for the 4 series. One could notice that the K_s for (S1, S3 and S4) are all about $0.23 mJ.m^{-2}$, whereas the surface anisotropy for the S2 is increased by a factor of 2. The saturation magnetization M_s for all the films is roughly 0.96 T. The obtained values of the surface anisotropy are in good agreement with other reported values for interfaces of permalloy to both non-magnetic metals and insulators as indicated in the table-3.3.

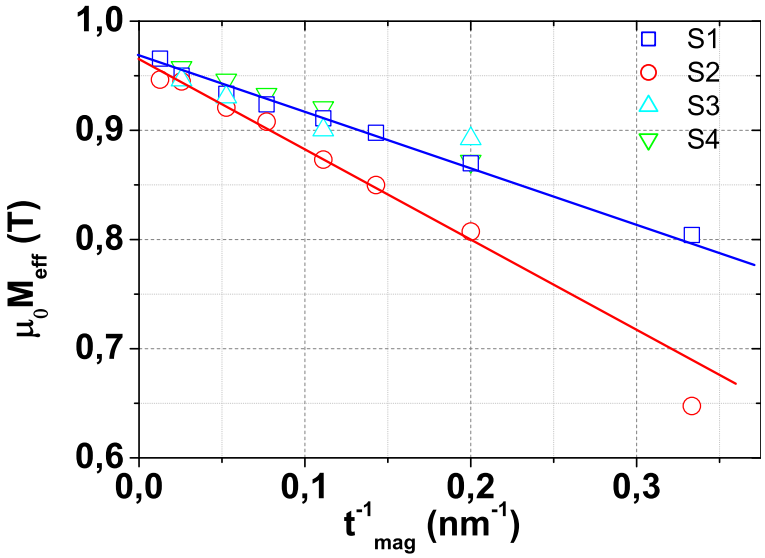

Figure 3.12: The changes of the effective magnetization with the inverse of the thickness for the 4 series. From the linear fit we extract the saturation magnetization of about 0.96 T and the surface anisotropy K_s.

Samples	$K_s(mJ.m^{-2})$	$\mu_0 M_s$(T)
S1	0.23	0.96
S2	0.45	0.97
S3	0.25	0.95
S4	0.24	0.97

Table 3.2: A summary of the surface anisotropy coefficient K_s and the saturation magnetization M_s for the 4 series.

Samples	$K_s(mJ.m^{-2})$	reference
SiOx/Py/resist	0.3	[52]
Al_2O_3/Py/Al_2O_3	0.5	[50]
Au/Py/Au	0.5	[51]
Ag/Py/Ag	0.2	[89]
Au/Py/Au	0.2	[89]
Ta/Py/Ta	0.16	[89]

Table 3.3: A comparison of the surface anisotropy coefficient K_s obtained from other studies for permalloy films with different capping layers

3.4.2 Line width

The second effect of the surfaces is to contribute to the magnetization relaxation processes. We aim to examine this effect through the thickness dependence of the peak to peak linewidth of the FMR signal.

We extract the peak to peak linewidth (ΔH_{pp}) from the Lorentzian fitting of the FMR signal for each film thickness. Figure-3.13 shows that the line width increases dramatically as the film thickness decreases for the 4 series. The line width increases from 2.8 mT for the 40 nm film to 5.8 mT for the 4 nm film. We can relate the line width to the Gilbert damping coefficient using $\Delta H = \frac{2\alpha\omega}{\sqrt{3}\gamma}$. The α coefficient varies linearly with the inverse of the film thickness as shown in figure-3.13, it can be modelled as:

$$\alpha = \alpha_0(1 + S/t).$$

In this expression, bulk (α_0) and surface (S) contributions to the Gilbert damping are separated. The bulk damping coefficient of the 4 series is ~ 0.007, and the surface damping of our films and of others studies are given in the table-3.4.

Samples	$\alpha_0[10^{-3}]$	S[nm]	reference
S1	7	2.7	our results
S2	6.7	3.6	
S3	7	2.1	
S4	6.7	2.7	
Al_2O_3/Py/Al_2O_3	7	1	[50]
SiOx/Py/PR - Cu/Py/Cu - Nb/Py/Nb	8	4	[52]
Al_2O_3/Py/PR	8	4	[23]
Cu/Py/Cu - Ta/Py/Ta	6.5-8	0	[78]
Ta/Py/Cu	8	2	[84]
Cu/Py/Cu- Ag/Py/Ag	8	1.5	[89]
Ta/Py/Ta	4	8	[89]

Table 3.4: The bulk and the surface contribution to the Gilbert coefficient for the four measured series, with a comparison with other studies. PR corresponds to the photoresist capping layer.

The damping coefficient in bulk permalloy is about 0.007 as measured in [10]. They attribute the magnetization relaxation to the spin-flip scattering of a conduction electron by phonons or defects through the spin-orbit coupling as discussed in [56].

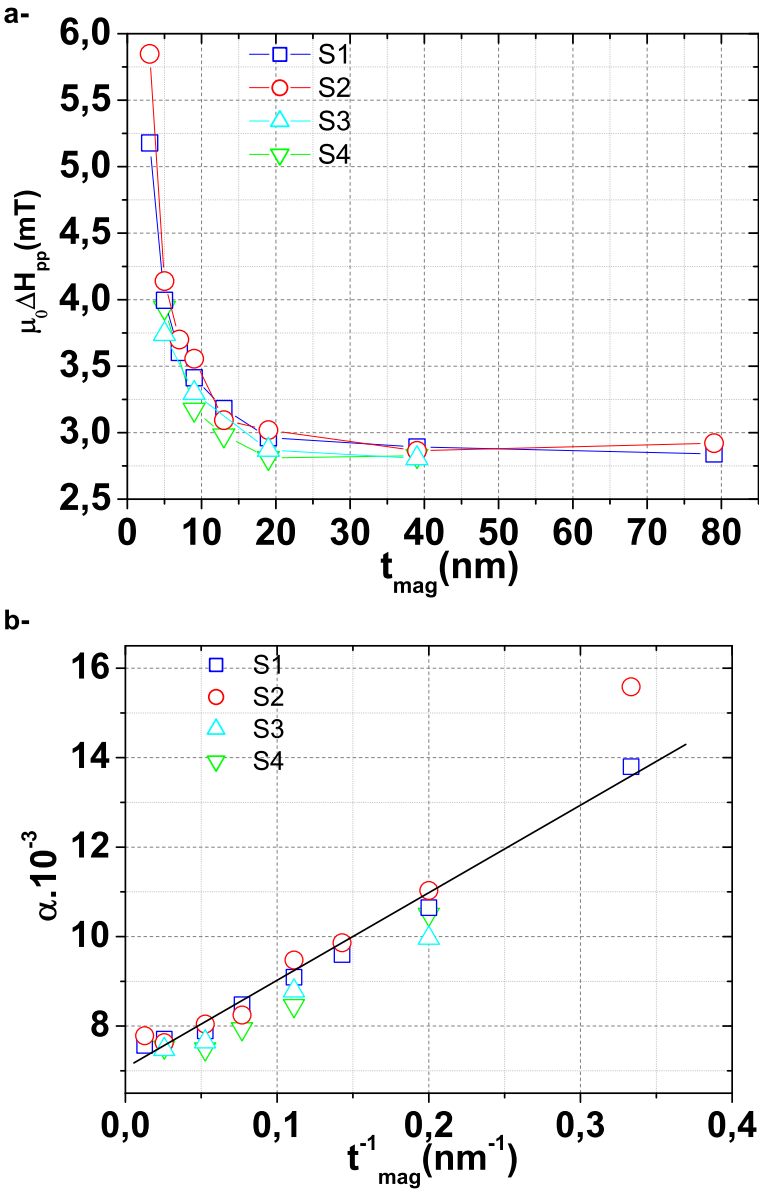

Figure 3.13: a) The variation of the line width as a function of the film thickness for the 4 series. b) The α damping coefficient as a function of inverse of the film thickness for the 4 series.

3.5 Complementary Ferromagnetic resonance characterization

In this section, first we present the results of complementary ferromagnetic resonance measurements as a function of the temperature and the angle. Second, we comment on a possible correlation between the magnetization relaxation and the resistivity, and we discuss the possible origin of the magnetization damping measured in our films.

3.5.1 Temperature dependence

As we conclude in section §(3.2), the static magnetic measurements at low temperature indicate an exchange bias effect in the thin films. It is known that the exchange bias contributes to an extrinsic contribution to the magnetization relaxation (see section §(1.4.4)). To investigate if the exchange bias influences the magnetization dynamics in our thin films ferromagnetic resonance measurements at variable temperature have been performed.
The measurements were done for 2 samples from the S1 series, with thicknesses 10 and 40 nm. The resonance field and the peak to peak line width from the FMR signals were extracted as we mention in a section §(3.4) at each temperature. The variation of the resonance field and the ΔH_{pp} are shown in the figure-3.14.

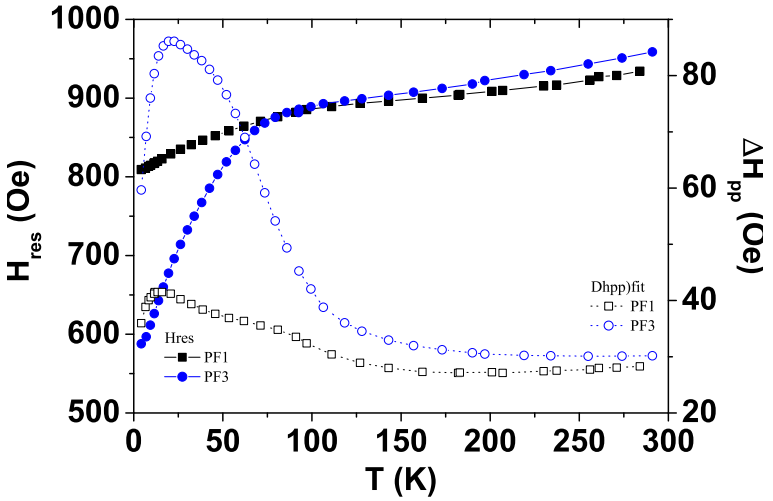

Figure 3.14: The H_{res} and the ΔH_{pp} as a function of the temperature for 2 films of thickness 10 and 40 nm from S1 series. The measurements were performed with a resonance frequency of the cavity is 9.38 GHz. The closed labels indicate the results of the resonance field and the open labels represent the linewidth. The blue and the black labels are for 10 nm and 40 nm film respectively.

One can observe a reduction in the value of the resonance field H_{res} as the temperature decreases for the 2 films. The H_{res} of the 10 nm film decreases more rapidly than that of the 40 nm film and at around 80 K it becomes sharper.

The H_{res} of the 10 nm reduces from $\sim$ 960 Oe at room temperature to $\sim$ 590 Oe at 4.2 K and the H_{res} of the 40 nm reduces from $\sim$ 935 Oe at room temperature to $\sim$ 810 Oe at 4.2 K. Notice that the relative variation of the H_{res} for the 10 nm between 300 K and 4.2 K is reduced by 4 time compared to the relative variation of the H_{res} of the 40 nm. This observation was explained by the exchange bias. At low temperature, either the oxide of the permalloy turns to be antiferromagnet, or the magnetic impurities are pinned near the interfaces. From this one expects a strong reduction of the resonance field. The effect seems to be a pure surface effect because it appears much more pronounced on the 10 nm than on the 40 nm film.
The peak to peak linewidth for the 10 nm film varies from about 30 Oe at room temperature to 60 Oe at 4.2 K and for the 40 nm film it varies from 28 Oe at room temperature to 36 Oe at 4,2 K. The peak to peak linewidth increases as the temperature decreases down to around 20 K. Then it passes through a maximum and it decreases again between 20 K and 4.2 K. The maximum of the line width at 20 K is more pronounced for the 10 nm film than for the 40 nm film as expected for a surface effect.
The temperature dependence of the linewidth is attributed to the slow relaxors effect (see §1.4.4) which adds an extrinsic process to the intrinsic linewidth. Accordingly, the total linewidth is expressed as:

$$\Delta H = \Delta H_{int} + \Delta H_{relaxer}(T),$$

where $\Delta H_{relaxer}$ is the linewidth contribution due to the slow relaxers.
The slow relaxors effect was observed in permalloy films [87], permalloy layer with a native oxide layer [64], permalloy films in contact with NiO [29], CoO layers [65] and in permalloy doped by heavy rare earth metals [114].
However in other studies the line width peak to peak is measured to be temperature independent as in permalloy layers protected with resist [23] and in permalloy layers which have a copper capping on both surfaces [64].

3.5.2 Angular dependence

An in-plane inhomogeneity of the sample results in an inhomogeneous broadening of the line of the ferromagnetic resonance as already discussed in the §(1.4.3). To examine the inhomogeneity in our thin films, angular ferromagnetic resonance measurements are performed. The variation of the orientation of the magnetization from the in-plane to the out-of plane configuration can be used to extract the inhomogeneous broadening in thin films. The angular dependent FMR measurements were carried out for 2 samples of the thickness of 40 and 6 nm from the S1 series. The angle between the in-plane axis and the static field was varied using a goniometer. At each angle we extract the resonance field and the peak to peak linewidth directly from the FMR signals.
Figure-3.15 shows the results of the measurements for H_{res} and ΔH_{pp}. One can observe an increase of H_{res} as the angle approaches the normal of the surface. It increases from 0.099 T (0.106T) when the field is applied in the film plane $\theta = 0^\circ$ to reach a maximum at 1.325 T (1.238T) when the field is applied out of the plane $\theta = 90^\circ$ for the 40 nm (respectively 6 nm) film. This is mainly due to a competition between the in-plane demagnetizing field and the out of plane

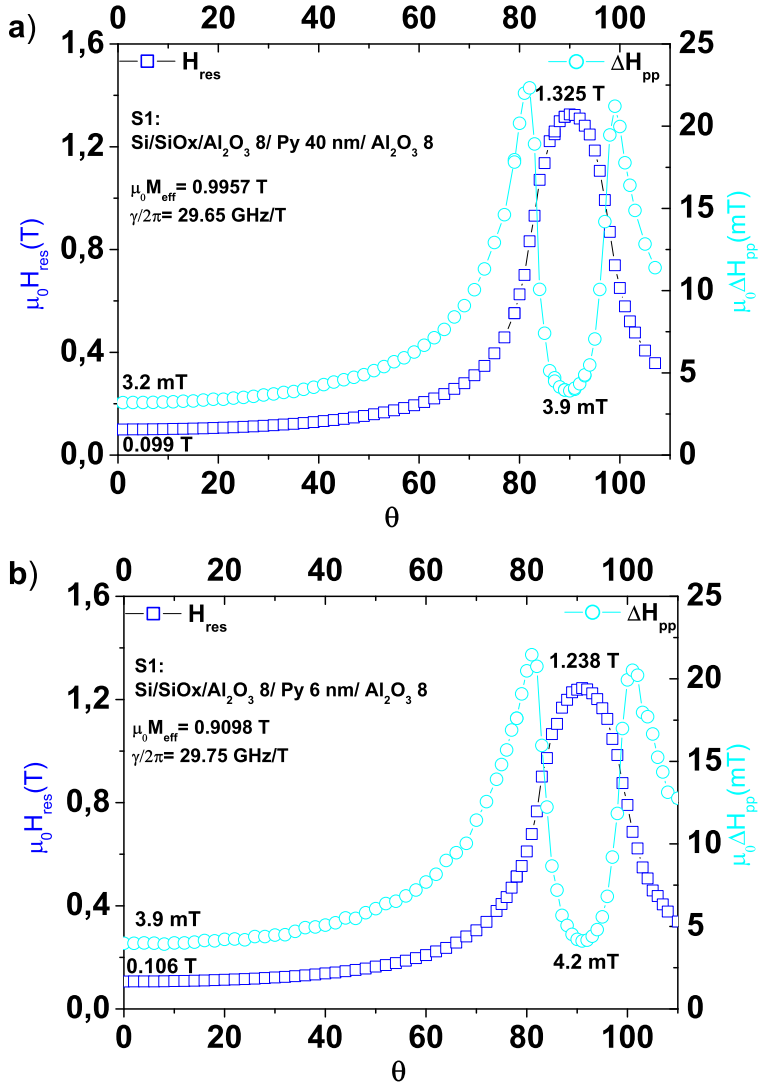

Figure 3.15: The FMR angular dependence for 2 samples of the S1 series of the thickness a) 40 nm and b) 6nm. The measured H_{res} and the ΔH_{pp} are plotted as a function of the angle θ between the in-plane axis and the applied static field. In the figure we indicate the H_{res} and the ΔH_{pp} for the in-plane and out of plane orientation of the magnetization. On each panel we indicate also the effective magnetization M_{eff} and the gyromagnetic ratio $\frac{\gamma}{2\pi}$ for each film. The measurements were performed at a resonance frequency 9.766 GHz of the cavity.

anisotropy field. Using the in-plane resonance condition in equation-3.2, and the out of the plane resonance condition $\omega_{res} = \gamma\mu_0(H_{res}^{\perp} - M_{eff})$, one can solve for M_{eff} and $\gamma/2\pi$. The extracted values are $\gamma/2\pi \sim 29.7 \pm 0.05$ GHz/T, and $\mu_0 M_{eff} = 0.995$ and 0.909 for the 40 nm and 6 nm films respectively.
Figure-3.15 shows also an increase of the linewidth as the magnetization is oriented out of the plane. The line width increases from 3.2 mT (3.9 mT) when $\theta = 0°$ to 3.9 mT (4.2 mT) when the $\theta = 90°$ and it passes through a maximum around $\theta = 80°$ for the 40 nm (respectively 6 nm film). The variation of the linewidth between the in-plane and the out of the plane orientation of the magnetization $(\Delta H_{\perp} - \Delta H_{\parallel})$ is measured to be very small for thinner films (0.3 mT) and increases slightly to 0.7 mT for the 40 nm film. These results are in agreement with the reported values $(\Delta H_{\perp} - \Delta H_{\parallel})$= 0.5 mT for the permalloy film sandwiched with Al_2O_3 layer [50]. We interpret this slight difference between the parallel and the perpendicular orientation to a very weak magnetic inhomogeneity of the samples. A distribution of the magnetic anisotropy appears as a distribution of the value of the effective magnetization δM_{eff}, within the local resonance model, this leads to an increase of linewidth $\Delta H_{\perp} = \delta M_{eff}$ for the perpendicular geometry and $\Delta H_{\parallel} = \frac{H_{res}}{H_{res}+2M_{eff}} \delta M_{eff}$ for the parallel geometry. The small measured values of $(\Delta H_{\perp} - \Delta H_{\parallel})$ indicates that the inhomogeneous broadening exist in our thin films but we emphasize that it is not dominant, and the measured linewidth is mainly due to the intrinsic relaxation of the magnetization.

3.5.3 Correlation between the damping and the resistivity?

As we have discussed the surfaces contribute to an additional scattering on the electrical resistivity (see §3.3) and to an additional contribution to the magnetization relaxation (see §3.4). Then a natural question may arise: are the electron scattering and the relaxation governed with a common process? we will treat this question first by referring to recent works and then we will discuss our results.
One of these works was performed by Ingvarsson et al. [52]. In this thickness dependence study the electrical resistivity and the damping coefficient were measured at room temperature. Their results showed an increase in the resistivity ρ is accompanied with an increase of the damping coefficient α. They report a linear variation between the damping and the resistivity as shown in figure-3.16. They interpret their results using a model proposed by [44] based on the effect

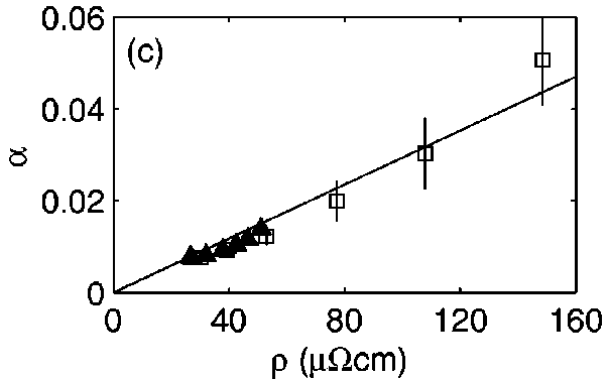

Figure 3.16: The variation of the damping coefficient α with the resistivity ρ obtained by Ingvarsson et al. The measurements were done for 2 series of permalloy film: the triangle label represents the films grown with an applied magnetic field, and the square label represents the series of the films grown without an applied field. The picture is taken from [52].

of the random walk process of the conduction electrons. This model predicts the following relation between the damping and the resistivity:

$$\alpha = \frac{\xi e^2 k_F \rho}{\pi^2 \hbar}, \tag{3.4}$$

where ξ is a constant relating the electron scattering and the spin relaxation $\tau_s^{-1} = \xi \tau^{-1}$, and k_F is the Fermi wave vector. They estimate the proportionality coefficient $\frac{e^2 k_F}{\pi^2 \hbar} = 3.7 \times 10^{-5} \Omega.m$ for a 3d metal, to deduce $\xi = 10^{-1}$ from the linear fit of the slope of α and ρ.

Counil et al. [23] examined the correlation between the magnetization relaxation and the electron scattering rate by extending the thickness dependence measurements at low temperature. The residual resistivity and the damping both increase as the thickness decreases. However, they do not show a linear relation as in [52] as shown in the figure-3.17.

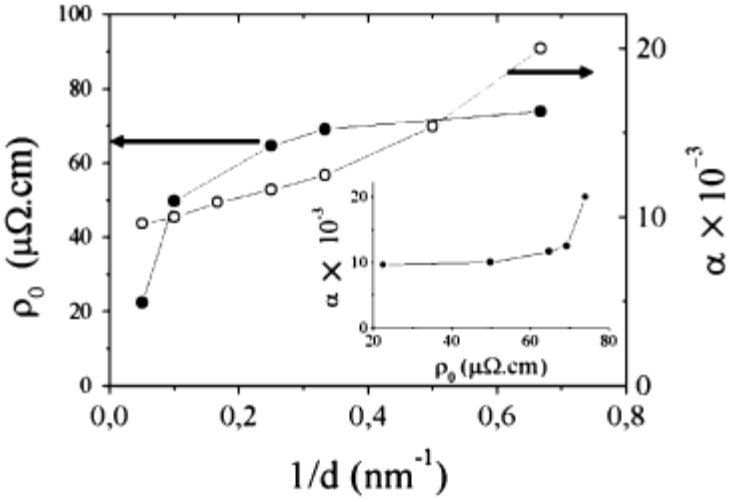

Figure 3.17: The variation of the residual resistivity and the damping as a function of the inverse of the thickness obtained by Counil et al. The in set shows the variation of the Gilbert damping parameter with the residual resistivity. The picture is taken from [23].

In our measurements the resistivity and the damping both increase as the film thickness decreases at room temperature. The correlation between the damping and the resistivity is shown in figure-3.18. One can notice that the thickness variation of the resistivity is larger than the thickness variation of the damping. The linear fit of our results shows a straight line which does not pass through the origin. It indicates the relation between the damping and resistivity is not compatible with the electron-magnon scattering as measured by Ingvarsson [52] ($\alpha \propto \rho$). As a possible explanation of this observation, one can imagine that different electron scattering processes (surfaces, disorder, and phonons) do not contribute in the same manner to the magnetization damping and to the resistivity [14].
The measured temperature dependence of the resistivity and the damping show different behaviors. The resistivity decreases with the temperature however the damping increases with temperature (which is attributed to the slow relaxer mechanism).

Based on the ferromagnetic resonance measurements we can discuss the possible origins of the measured FMR linewidth in our thin films.

- First, the intrinsic relaxation processes contribute significantly to the linewidth.
- Second, the inhomogeneous broadening does not contribute significantly to the measured linewidth.
- Third, the slow relaxors are not expected to contribute to the linewidth at room temperature.
- Fourth, we observe a surface contribution to the damping. This surface contribution may be attributed to the following hypothesis:

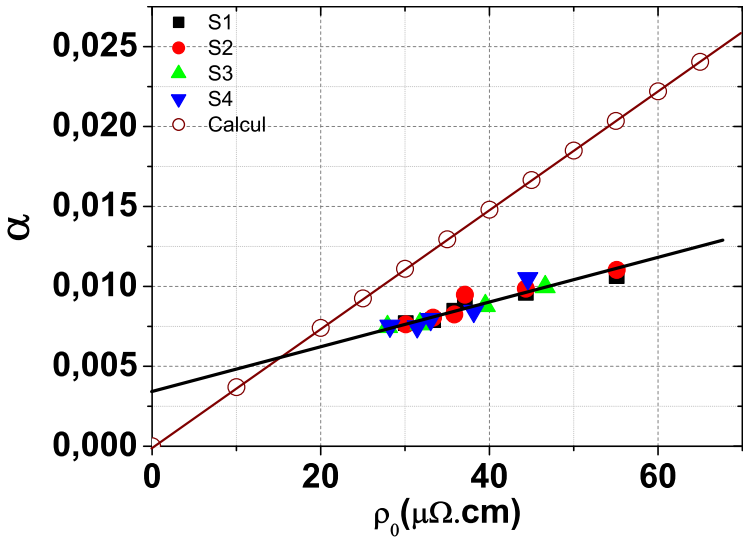

Figure 3.18: Variation of the Gilbert damping coefficient with the resistivity for the four series of permalloy. Open circles are the calculated values using equation 3.4 and the parameters extracted by [52].

- Due to a breaking of the orbital symmetry for the atoms located at the interfaces, the surface atoms could produce a higher spin-orbit coupling than the bulk atoms and hence a higher contribution to the magnetization damping.
- In case the thin films are not homogeneous (for example if a thin pure Nickel layer exists an interface α could be written as:

$$\alpha = \frac{\alpha_{Ni} t_{Ni} + \alpha_{Py} t_{Py}}{t_{Ni} + t_{Py}}$$

  which could be explained the observed 1/t behavior.

Conclusion

At the end of this chapter, we have identified the characteristics of our permalloy thin films by performing a set of measurements as a function of the film thickness. As one can notice, the surfaces play a major role in modifying the electrical and the magnetic (surface anisotropy) properties of the materials. In addition, the relaxation processes in the thin films were determined to be dominated by an intrinsic bulk contribution combined with a surface contribution which does not follow the simple behavior discussed in [52]. This chapter provides us with a general understanding of the properties of the permalloy thin films, which will be used for spin wave experiments of chapters 4 and 5.

Chapter 4

Propagation of magnetostatic surface wave in permalloy thin films of different thicknesses

Spin wave excitations and propagation in magnetic microstructures have been widely investigated during the last decade using propagating spin wave spectroscopy [6][7][112], Brillouin light scattering microscopy [27][82][113], and coplanar waveguide ferromagnetic resonance [24][96].
In this chapter, we present an original thickness dependence study of the propagation of spin waves in permalloy thin films using the propagating spin wave spectroscopy technique. The spin waves under investigation are the so-called magnetostatic surface waves (the in-plane magnetic field is perpendicular to the propagation direction).
In section §4.1 we will describe the principle of the propagating spin wave spectroscopy technique. In section §4.2, the magnetic parameters of the permalloy films are extracted from the reflection measurements. In section §4.3, the propagation characteristics of the magnetostatic surface waves are analyzed from the transmission signals. In section §4.4 the non reciprocity character in amplitude and in frequency of the magnetostatic surface wave signals are discussed.

4.1 Propagating spin wave spectroscopy

Recently the propagating spin wave spectroscopy was applied to study the spin wave characteristics in metallic ferromagnets. In contrast to the traditional FMR technique, this method requires nano-fabrication processes for each individual sample. In this section, the principle of the method is explained and the sample fabrication procedure is described. Then, a short description how to handle the measurements is provided (calibration and signal processing).

4.1.1 Principle of the method

Historically, the magnetization dynamics was detected using the cavity ferromagnetic resonance. This technique is an effective tool used to measure the uniform mode (k=0) of the magnetization dynamics in a ferromagnetic sample. One of the limitation of the cavity FMR technique is that it can not detect the non-uniform modes ($k \neq 0$). In addition, the cavity FMR works at a constant frequency and can not be used to follow the evolution of the modes as a function of the frequency. With the need to understand the non uniform oscillations of the magnetization in a microstructure, many experimental techniques were proposed to follow the resonance behavior with the frequency as in the coplanar waveguide FMR (CPW-FMR) or to study the non-uniform excitation with a finite wavevector ($k \neq 0$). Recently, a miniaturized version of the propagating spin wave spectroscopy technique (PSWS) was developed to study the spin waves in the frequency domain [7] and in the time domain [25]. The PSWS technique was initially applied to yttrium iron garnet (YIG) insulating film [18]. The principal challenge of applying the technique to metallic films was the larger damping of the oscillations compared to that in the insulating films which impedes propagation over distances larger than a few micrometers. Recently, a miniaturized version of the propagating spin wave spectroscopy technique at a nanometer scale was developed. In the following, an explanation of the principle of this technique is presented.

Propagating spin wave spectroscopy is an inductive technique where micrometer sized transducers (antennas) are used to excite and to detect the spin waves. In figure-4.1 a schematic drawing illustrates the principle of the technique. It shows a spin wave propagating between the two transducers with a given wavevector (k). The antennas are conducting patterns placed at a distance h on the top of the ferromagnetic stripe. Once a microwave current $i(\omega)$ passes through one antenna, a microwave field $h(\omega)$ is generated around each conductor. The microwave field $h(\omega)$ owes its spatial distribution to the shape of the antennas, and hence it oscillates at a wavelength determined by their periodicity. The microwave field couples to the oscillating spin wave modes in the ferromagnetic stripe and these spin waves propagate in both directions (+k and -k). The propagating waves induce an additional magnetic flux onto the second antenna. According to Faraday's law the magnetic flux generates an oscillating voltage $v(\omega)$ which can be measured using a suitable microwave receiver. Additionally, the antenna used for the excitation of the spin waves also detects the generated flux and a microwave voltage can also be measured on the excitation antenna itself.

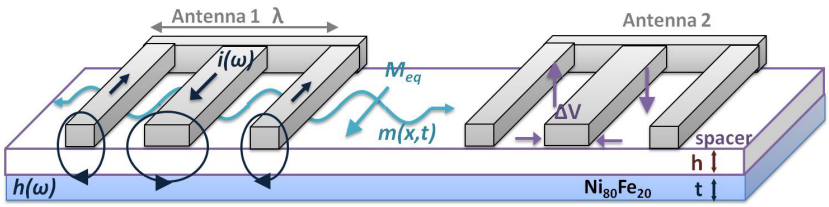

Figure 4.1: A sketch of the propagating spin wave spectroscopy technique. It displays a spin wave propagating between the antennas at a given wavevector.

4.1.2 Sample fabrication

Standard fabrication processes have been used to fabricate suitable microwave circuits for the propagating spin wave spectroscopy and the current induced spin wave Doppler shift experiments. The S4-series (table-3.1) have been used for that purpose. All the micro and nano-fabrication work has been done in the nanofabrication platform STnano in Strasbourg.
Four different devices have been realized for each film thickness. The nominal parameters of each single device are shown in the table-4.1. Each device consists of a ferromagnetic stripe, a pair of coplanar waveguide for the microwave connection, four DC pads, an insulator, and the two antennas. A picture of a final device is shown in the figure 4.2.

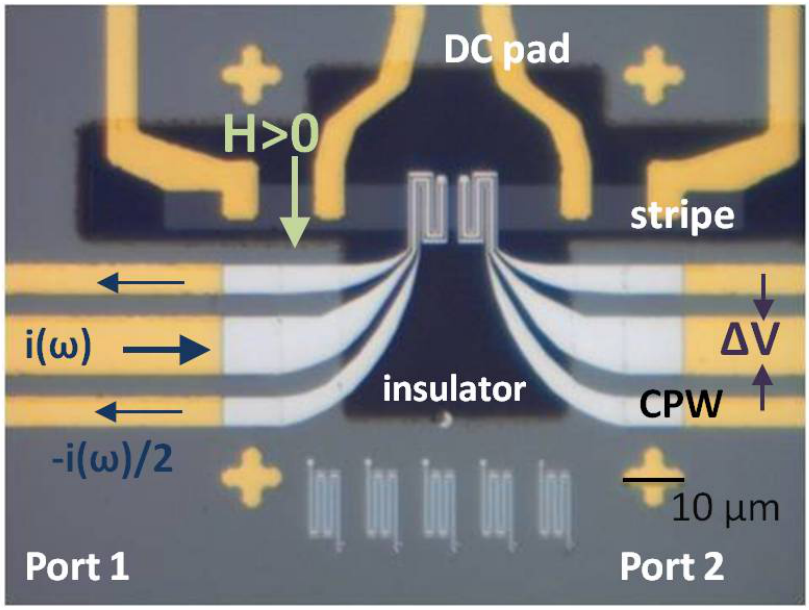

Figure 4.2: An optical image of a final device showing the result of the four fabrication steps: 1) the ferromagnetic stripe, 2) the coplanar wave guide and the DC pads, 3) the insulator pattern, 4) the antennas.

Device	w (μm)	k (μm^{-1})	λ (μm)	nb of meanders	D (μm)
8 μm	8	3.86	1.6	3	8.8
3 μm down	3.5	3.87	1.6	3	14.5
3 μm up	3.5	7.8	0.8	5	5.5
2 μm	2	7.84	0.8	5	7.7

Table 4.1: The parameter of each devices (w, k, λ, D) are the ferromagnetic stripe width, the wavevector, the wavelength, and the distance between the centers of the 2 antennas.

The antennas consist of a central conductor between two ground conductors adapted to the coplanar waveguide geometry. They are folded several times onto themselves to obtain a nearly periodic distribution. The Fourier transform of the linear current density normalized by the current is calculated for this geometry, figure-4.3 shows SEM images of the antenna for 8 μm and 2 μm devices together with the corresponding Fourier transformation. The Fourier transform shows two excitation peaks: a principle peak with higher wavevector (k_1) and a secondary peak with lower wavevector (k_2) [110]. The wavevectors of the peaks are almost monochromatic with a dispersion Δk as indicated on the figure-4.3. These wavevectors are the highest wavevectors that we could obtain with the resolution of the e-beam lithography. In the following we will present the fabrication procedure for each step.

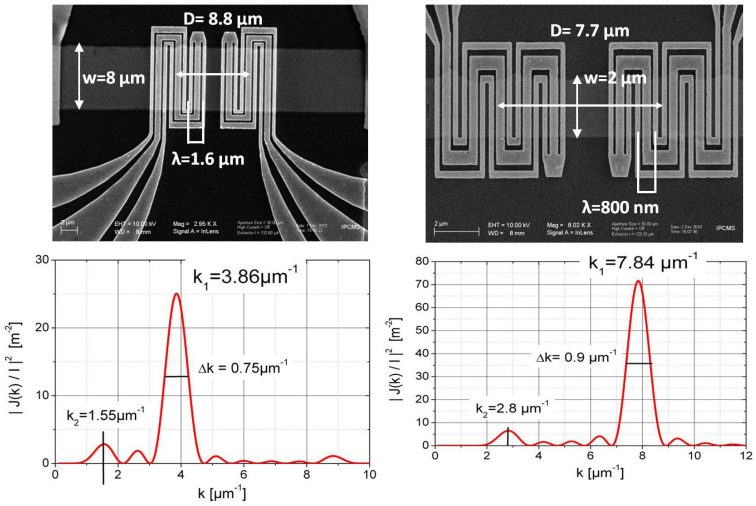

Figure 4.3: SEM images for the antennas used for the excitation of the spin wave in the 8 μm and 2 μm devices, and their Fourier transforms.

The Stripe:
In the first step, we fabricate the 4 ferromagnetic stripes with a length of 100 μm and a width w as noted in the table-4.1. The sample is covered with 0.5 μm of photoresist S1805. The sample is aligned below a mask (Chromium pattern on a glass plate) and the sample is exposed to an ultraviolet light using a MJB4

mask aligner ($\sim$ 3 sec). Then the sample is put in a solution (AZ developer 1:1 $H_2O \sim 12sec$) which dissolves only the resist exposed to UV light. We etch the uncovered parts of the film using the Ar^+ ion gun available in the Plassys evaporator. We precisely identify the etching rate for each material (table-4.2) by etching a thick layer of each metal for a long time. The etching time is adjusted for each sample to etch the top Al_2O_3 layer, the thickness (t) of the permalloy, and 5 nm of the bottom layer of the Al_2O_3. Then, the resist is dissolved to end up with the 4 stripes as shown in the figure-4.4.

metal	rate (nm/min)
Al_2O_3	6.5
Py	12
SiO_2	10

Table 4.2: The etching rates for the different materials.

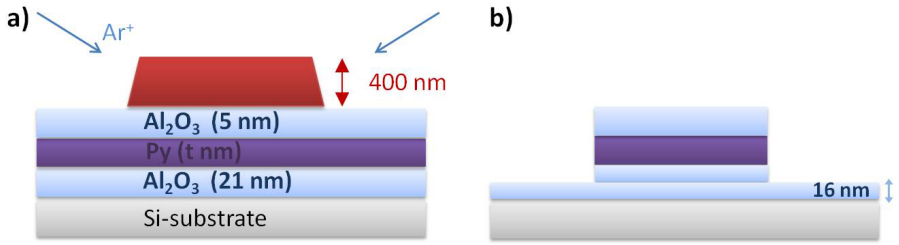

Figure 4.4: a) A sketch of the device after a positive optical lithography step. b) The pattern of the stripe after the etching and the removal of the photoresist.

The coplanar waveguide and the DC pads:
In the second step, a pair of coplanar waveguides is fabricated for the microwave connections together with four DC pads for the DC current used in the Doppler shift measurements. This is done using an optical lithography in the negative tone.
In a negative lithography we use an image reversal resist such as AZ 5214 resulting in a negative pattern of the mask. The image reversal is obtained by a crosslinking of the resist, with a postbake of the substrate at $120°C$ for 1 min. This leads the exposed resist to become insoluble in the developer, whereas the unexposed resist still behaves like a normal photoresist. After a flood exposure without a mask, the initially unexposed area is dissolved in the developer, while the crosslinked areas remain as shown in the fig-4.5a.
The next step (pre-etching and metal deposition) is done again in the Plassys e-beam evaporator. First, the on top Al_2O_3 layer is etched to ensure proper electrical contact with the Permalloy stripe. Then, a metal deposition is done with 10 nm of Ti and 60 nm of Au (base pressure 10^{-7} mbar, deposition rates 0.1 nm/min and 0.2 nm/min for Ti and Au respectively). Finally, the film is immersed in the aceton for a few minutes to lift-off the metals deposited over the photoresist as shown in figure 4.5.

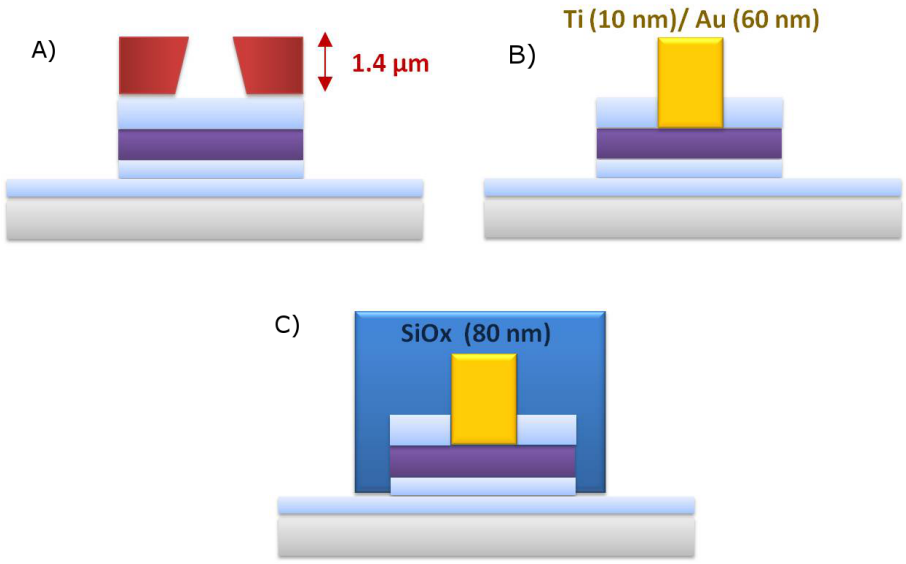

Figure 4.5: a) Sketch of the device after a negative optical lithography step. b) The pattern of the coplanar waveguide and the dc pads after the metal deposition and the lift off process. c) after the deposition of the insulating SiOx layer.

The insulator:
In the third step of fabrication, an insulating pattern is fabricated on the top of the stripe to avoid an electrical connection between the stripe and the antennas (figure-4.5 C). We pattern the structure by optical lithography using an image reversal resist as explained in the previous paragraph. An SiO_2 layer of 80 nm ($\sim$ 120 nm for the sample made from the 40 nm permalloy film) is deposited by sputtering [1] at the ECPM. The pattern is transferred by lift-off (which takes a longer time compared to the lift off of metals layers deposited by the evaporator).

The antennas:
We use e-beam lithography and e-beam evaporation to fabricate the antennas on the top of the magnetic stripe. The antennas have a meander shape, they consist of closely spaced lines with smallest size of the order of 150 nm. The main difficulty of this step is to adjust the nominal exposure dose of the resist. It is a critical parameter since if one underestimates the exposure time the resist will not be sufficiently developed and the lines will not lift off after the metal deposition, if one overestimates the exposure time the resist will be over exposed and the lines will fall down. We pay a careful attention to this parameter by doing several dose tests to identify the right resist and the right dose. The best results were obtained using a bilayer of resist A5 PMMA 495K/ A2 PMMA 950 K with a dose of $225\mu C/cm^2$ and at an electron beam voltage of 20 KV.

[1] Many attempts had been made to fabricate the SiO_2 layer by using an e-beam evaporator, unfortunately the layers obtained were not robust enough and were frequently destroyed during the lift off.

Before the metal deposition the resist is cleaned using a plasma oxygen cleaner (30 W, 45 sec) to remove any contamination in the lithography and to improve the connection between the coplanar waveguide and the antennas. Then a metal deposition of 10 nm of Ti and 120 nm of Al is done using the e-beam evaporator.

The final sample
During the lithography processes several problems happened which made some devices unusable. Table-4.3 summarize the results of the fabrication process.

Device	k μm^{-1}	40 nm	20 nm	14 nm	10 nm	6 nm
8 μm	3.86	M	M	X	M	M
3 μm down	3.87	M	X	X	M	NM
3 μm up	7.8	M	X	M	X	NM
2 μm	7.84	X	M	X	M	NM

Table 4.3: A summary table for the final obtained devices. M represent the samples that have been measured, X represents samples that were not useable and NM the samples that were usable but that could not be measured due to lack of time.

4.1.3 Calibration

4.1.3.1 The experimental setup

Figure-4.6 shows the experimental setup of the propagating spin wave spectroscopy. The microwave excitation and detection of the spin waves are performed by a vector network analyzer (VNA) (Agilent PNA E8364B) in the frequency range between 10 MHz and 26.5 GHz. The exits of the VNA (port 1 and port 2) are connected to flexible coaxial cables. The coaxial cables are connected to microwave picoprobers with a design matching the design of the coplanar waveguide. To connect the picoprobers to the coplanar waveguide the probers are mounted on micropositioners and their manipulation is done using a microscope.

4.1.3.2 The microwave circuit

Whenever there is an impedance mismatch between the microwave elements (the vector network analyzer, the coaxial cables, the coplanar waveguide,...), a part of the propagating signal is reflected and a standing wave is generated in the transmission line, which leads to a substantial change in the characteristic of the signal. Since the microwave elements are not ideal we can not avoid the impedance mismatch between them. However these errors can be corrected with the help of calibration standards whose reflection and transmission components are well known. The microwave circuit is calibrated for the 2 ports of the vector network analyzer using a calibration substrate containing coplanar circuits behaving electrically as: a short (0 Ω) , an open (∞ Ω), a load (50 Ω) and an ideal transmission line. We perform the calibration measurements of the microwave circuit over the whole frequency range (10 MHz- 26.5 GHz) at a power of -5

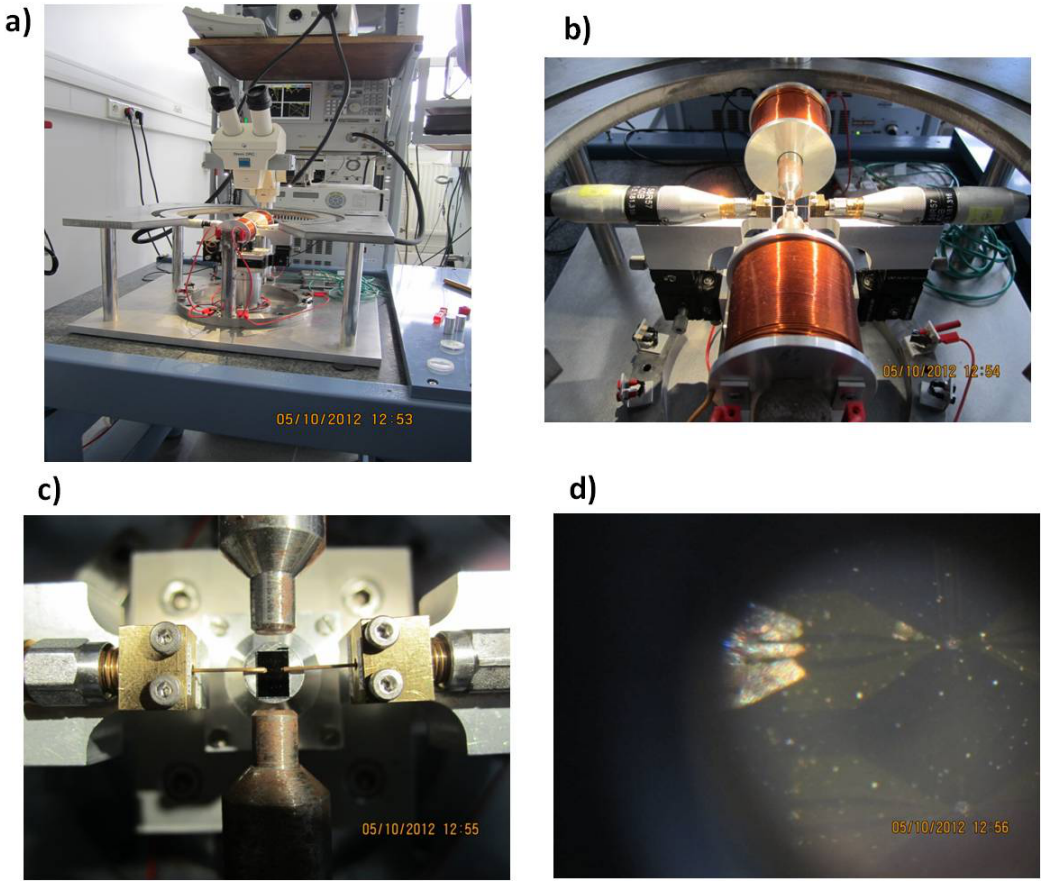

Figure 4.6: a) Picture of the propagating spin wave spectroscopy setup, a zoom-in view showing the coils and the coaxial cables (b), the picoprobers (c), and the contact between the picoprobers and the coplanar wave guide (d).

dBm. After we finish the calibration we add an additional electrical delay of about 17 ps to account for the propagation of the microwave signal between the coplanar access and the antennas.

4.1.3.3 The magnetic field

We use two home made coils consisting of a copper wire rounded over an aluminum cylinder. The coils are held over an iron pole. They are connected to a DC power supply. In the present version of the experiment, it is not possible to measure the magnetic field during the measurements. We calibrate the magnetic field before starting the measurement for each device. We measure the magnetic field for different current values between +5 A and -5 A with a Hall probe at the place of the sample. The calibration measurements shows a maximum of the magnetic field at 5 A of 0.31 T, and it indicates a hysteresis with a field of 15 mT at zero current as shown in the figure-4.7. During the measurements we start always from a high magnetic field value near the saturation field to ensure that the measured magnetic field belong to the major branch of the hysteresis loop. Any small deviation from the major branch of the loop will lead to a different value of the magnetic field. This could be reflected to an error on the value of the field.

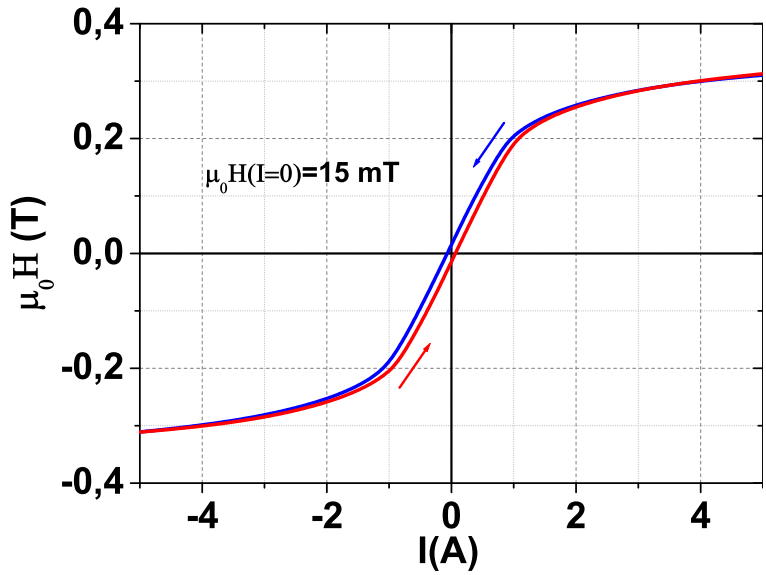

Figure 4.7: The calibration of the magnetic field with a Hall probe between +5 A and -5 A.

4.1.4 Signal processing

We measure the variation in the impedance Z_{ij} of the microwave circuit due to the magnetic flux induced by the propagating wave in the antennas. For a single measurement a couple of acquisitions is done at two different fields:

in the first acquisition the impedance $Z_{ij}(\omega, H_{res})$ is measured at a field H_{res} corresponding to the spin wave resonance field and in the second measurement the impedance $Z_{ij}(\omega, H_{ref})$ is measured at a reference field H_{ref} higher than H_{res}. The reference measurement is done to eliminate the electromagnetic peaks which do not belong to the resonance behavior. Since the coupling between the ferromagnetic stripe and the antennas is purely inductive, one can deal with the inductance matrix ΔL_{ij} as a response function of the ferromagnetic stripe to the microwave excitation. We transform the impedance measurements to inductance through the operation:

$$\Delta L_{ij} = \frac{1}{i\omega}[Z_{ij}(\omega, H_{res}) - Z_{ij}(\omega, H_{ref})], \tag{4.1}$$

The propagating spin wave spectroscopy signals can be recorded conveniently using the vector network analyzer (VNA) which is able of determining the impedance matrix $Z_{ij}(\omega)$ of a two port device

$$v_{ij} = \sum_j Z_{ij}(\omega) i_i(\omega) \tag{4.2}$$

where v_i and i_i are the voltage and the current related to the two ports i=1,2. To determine the four elements of the matrix, the VNA switches automatically the excitation between port 1 and port 2. We measure the self inductance ΔL_{ii} and the mutual inductance signals ΔL_{ij} in the same run. The mutual inductance signal of the magnetostatic surface waves are measured with a relatively small amplitude of the order of a picoHenry (pH). Such small signals are sensitive to any weak perturbation that occurs during the measurements. We average the signals many times to rule out these perturbation, and to improve the signal to noise ratio. In the following next sections, we will analyze the self and the mutual inductance to determine the magnetic parameter of the thin films and to identify the propagation characteristics of the spin waves in the permalloy thin films.

4.2 Reflection measurements

4.2.1 Self inductance spectra

This section is devoted to the discussion of the reflection signals measured by the propagating spin wave spectroscopy in the magnetostatic surface wave configuration. The analysis of the reflection signals allows one to understand the characteristics of the excited waves in the thin films [8]. The magnetic parameters of the film are extracted by following the frequency at which the waves are excited, and the line width of the reflection signal is known to be related to the relaxation processes.

4.2.2 Resonance frequency as a function of the magnetic field

An example of the measured reflected signals ΔL_{11} and ΔL_{22} is shown in figure-4.8, it corresponds to a measurement performed at an applied field of 28 mT and a reference field at 200 mT for the 8 μm device of the 10 nm film. Both the real

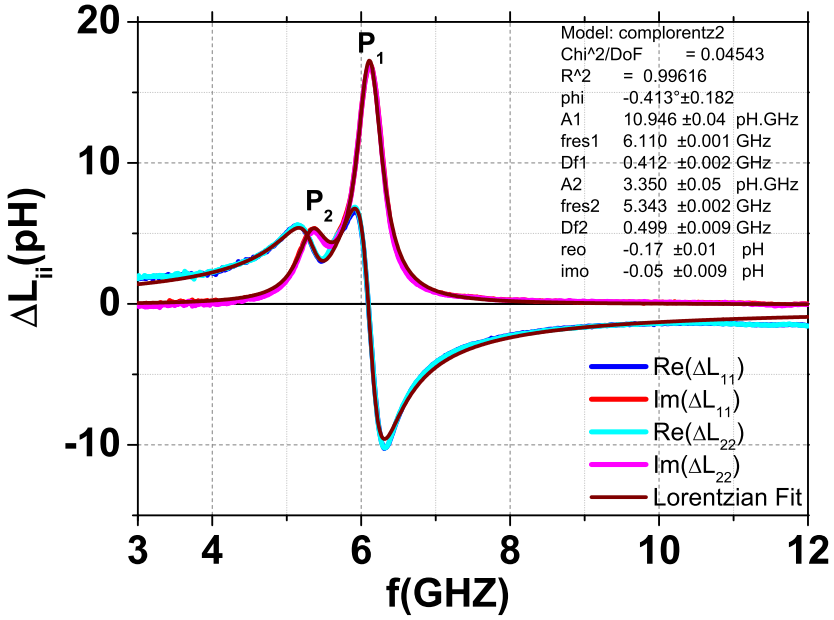

Figure 4.8: An example of the measured self inductance signals showing the real and the imaginary parts of the self inductance ΔL_{11} and ΔL_{22}. The real and imaginary parts of the spectra are well reproduced with a lorentzian fit. The parameter for each peak are noted in the table. The signals are taken for a 10 nm thick film with a width of 8 μm and the wavevectors k_1= 3.86 μm^{-1} and k_2= 1.55 μm^{-1} with an external applied field of 28 mT. The measurements were done at a power -10 dB and with a band width of 100 Hz.

and the imaginary components of the self inductance are shown. The imaginary part shows a clear absorption peak, and the real part passes through zero and change its sign at the maximum frequency of this peak. In the given example, a main resonance peak is observed at a frequency $f_1 = 6.11$ GHz and a secondary, lower amplitude, resonance peak is observed at a frequency $f_2 = 5.343$ GHz. The two resonance peaks are attributed to the excitation of spin waves with two different wavevectors k_1 and k_2. The Fourier transform of the current density of the antennas in this geometry shows a main peak at a wavevector k_1 and a secondary peak at a lower wavevector $k_2 < k_1$ as shown in the figure-4.3. Consequently, the antenna couples to the spin waves with a wavevector k_1 at a higher frequency f_1 and with a wavevector k_2 at a lower frequency f_2.
We also remark that the 2 self inductance ΔL_{11} and ΔL_{22} are identical. It indicates that the two antennas have the same excitation characteristics. We note also that the base line for the 2 signals is almost zero.
A Lorentzian fit reproduces well the form and the amplitude of the self inductance spectra as represented by the wine lines in the figure-4.8. We extract the resonance frequency, the area and the full width at half maximum for each peak from the parameter of the Lorentzian fit as indicated in the figure-4.8.

The self-inductance measurements have been repeated for different values of the applied magnetic field up to 0.3 T. Figure-4.9 shows the self inductance spectra obtained at different applied fields for two devices of the 10 nm film. The left column corresponds to the 8 μm device (k= 3.86 μm^{-1}) and the right column corresponds to the $2\mu m$ device (k= 7.8 μm^{-1}). As we increase the field, we observe an upward shift in the resonance frequency as expected from the Kittel formula, in addition to a noticeable decrease of the amplitude of the signal. The amplitude of the signal for the 8 μm stripe is roughly 4 times greater than the amplitude of the signal for the 2 μm stripe. We notice the main and the secondary resonance peaks are well separated at lower frequency and they summed up into one peak at higher frequencies: at higher frequencies the separation distance between the two peaks vanishes and they collapse to form one single peak as shown in the panel of the measurement at 257 mT.
We perform a Lorentzian fit for each spectrum as discussed in the previous section. Figure-4.10 shows the field dependence of the resonance frequencies extracted from such fits for the main peak ($f_{res}(k_1)$) and for the secondary peak ($f_{res}(k_2)$) for six different devices. For all the devices the frequency clearly increases with the field. However, the zero field extrapolations are significantly higher for thicker films and higher wavevectors. This is easily explained considering the zero field term of the dispersion relation for the magnetostatic surface waves 1.47 which writes as $\frac{M_s^2}{4}(1 - e^{-2kt})$. Following a standard procedure for FMR measurements, we fit the obtained $f_{res}(H)$ to a Kittel formula:

$$f^2 = A(\mu_0 H)^2 + B(\mu_0 H) + C, \tag{4.3}$$

where A, B, and C are constant parameters. The procedure is illustrated in figure-4.11 which shows the fits for two devices of the 10 nm film. We will now relate these three parameters to the magnetic properties of the films.

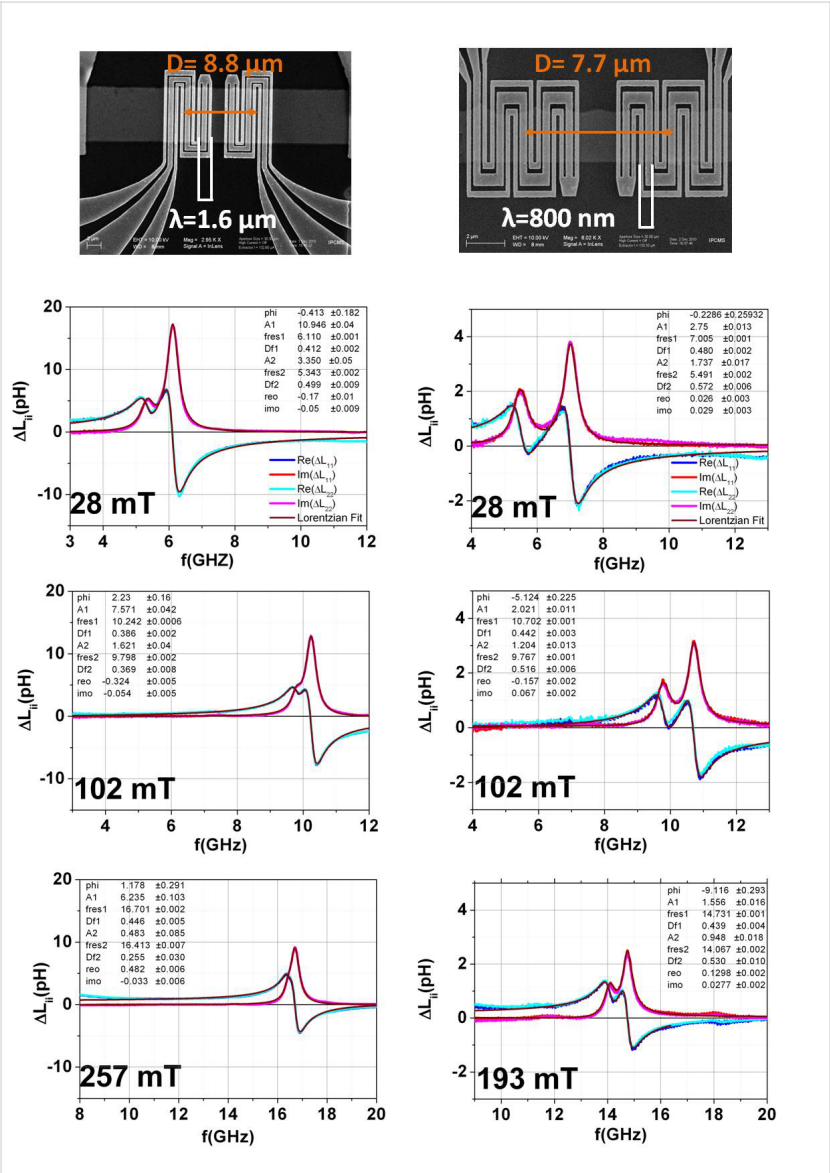

Figure 4.9: The self inductance signals measured for 2 devices of the 10 nm film with a width of 8 μm (left column) and 2 μm (right column). The SEM images in the top panel show the antennas used for the excitation and the detection of the spin waves. In each panel the applied field and the parameters of the lorentzian fit are indicated. The measurements were performed with a power of -10 dB and a 100 Hz bandwidth.

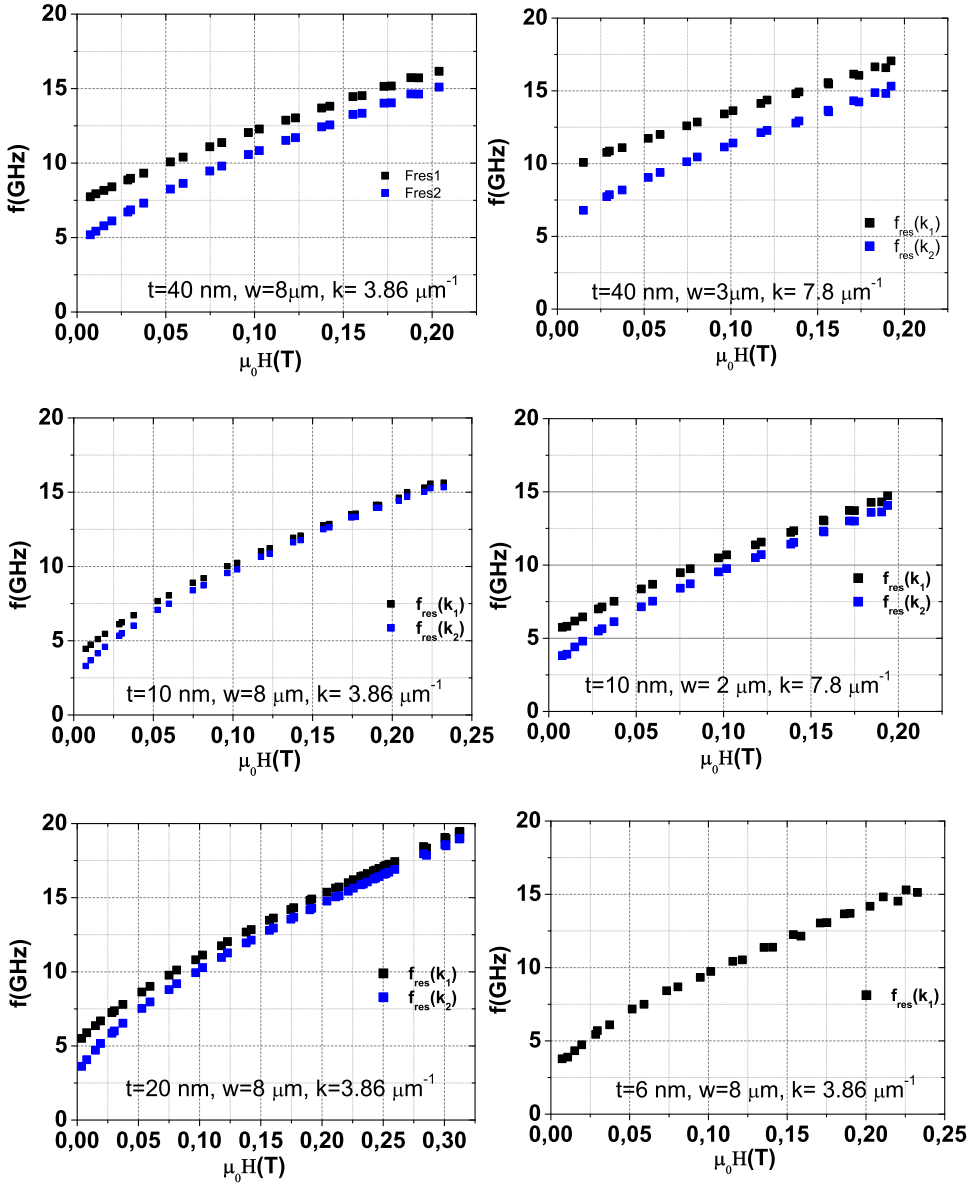

Figure 4.10: The variation of the resonance frequency as a function of the applied field for different devices.

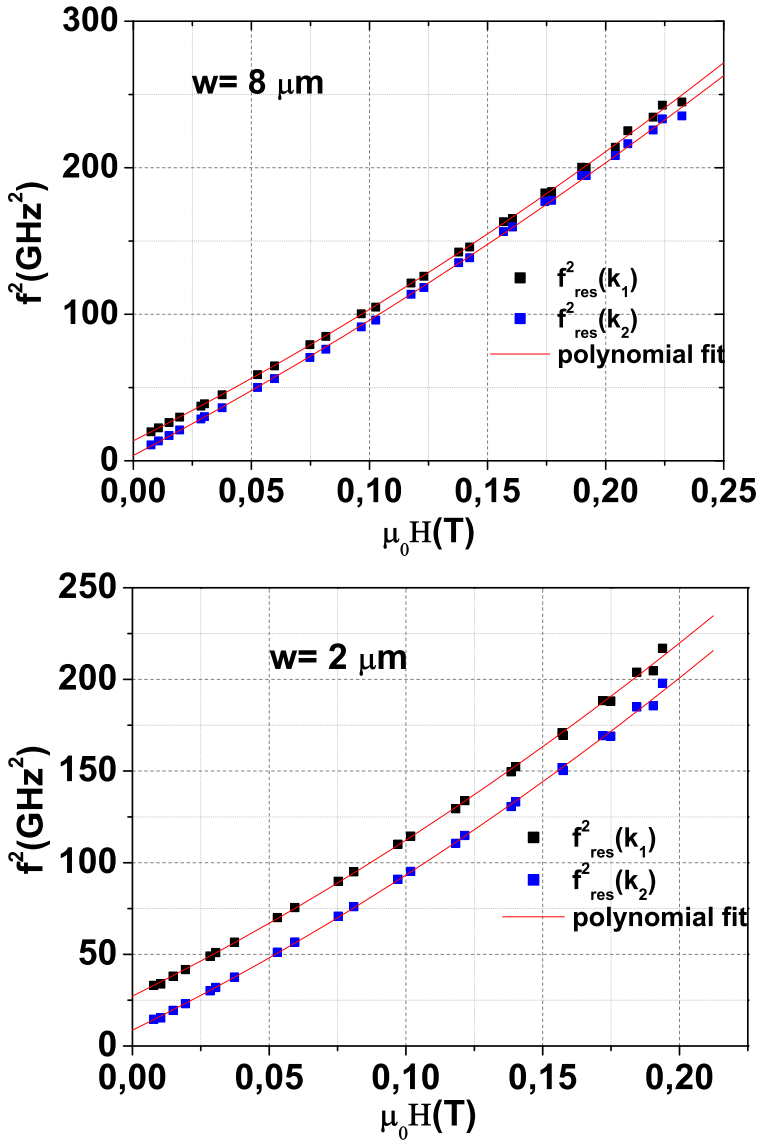

Figure 4.11: Kittel-like fits of the magnetic field dependence of the resonance frequency for two devices of the 10 nm films.

4.2.3 Extraction of the magnetic parameters

From the magnetostatic theory the dispersion relation of the magnetostatic surface waves is derived as:

$$f^2 = (\frac{\mu_0\gamma}{2\pi})^2[H^2 + HM_s + \frac{M_s^2}{4}(1 - e^{-2kt})], \tag{4.4}$$

where H is the applied field and M_s is the saturation magnetization. To account for the effect of an anisotropy field H_K perpendicular to the film and for the effect of the in-plane demagnetizing field H_d, we write an approximate formula of the dispersion relation:

$$f^2 = (\frac{\mu_0\gamma}{2\pi})^2[H_{tot}^2 + H_{tot}M_{eff} + \frac{M_{eff}M_s}{4}(1 - e^{-2kt})], \tag{4.5}$$

where $H_{tot} = H - H_d$, $H_d = \frac{2}{\pi}\frac{t}{w}M_s$, and M_{eff} is the effective magnetization $M_{eff} = M_s - H_K$. (see section 1.2.2.2 and Appendix A).
Equation-4.5 predicts a quadratic field dependence of the square of the resonance frequency similar to what we observe in figure-4.11. We will now compare the A, B, C coefficients extracted for the fits to the values expected from equation-4.5 using the magnetic parameters derived from the FMR study of chapter 3.

The gyromagnetic ratio $\frac{\gamma}{2\pi}$:
From equation-4.5, it is clear that the square root of the parameter A of the quadratic fits can be identified to the square of the gyromagnetic ratio $\frac{\gamma}{2\pi}$. The obtained values are shown in figure-4.12. The measured values are in the range of the value deduced from the broadband FMR measurements on similar films $\frac{\gamma}{2\pi} = 30GHz/T \pm 1$. The dispersion of the values is mainly due to some uncertainty of the values of the magnetic field in the high field limit which has a large influence on the determination of this parameter.

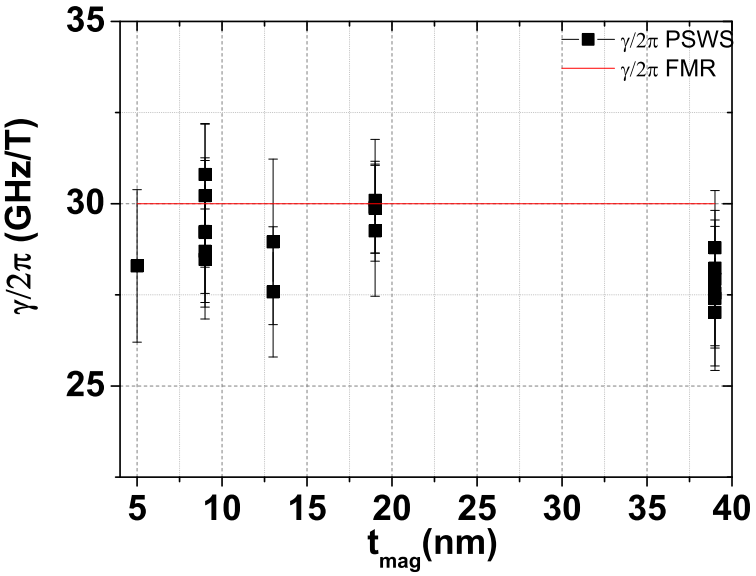

Figure 4.12: $\sqrt{A}$ parameter deduced from the quadratic fits described by equation 4.3 and figure 4.11. The horizontal bars shows the estimate deduced from the broadband FMR measurements: $\sqrt{A}_{theo} = \frac{\gamma}{2\pi}$ where $\frac{\gamma}{2\pi}$ =30 GHz/T.

The effective magnetization M_{eff}:
From equation 4.5, it can be deduced that the theoretical B coefficient is given by $B_{theo} = (\frac{\gamma}{2\pi})^2(\mu_0 M_{eff} - 2\mu_0 H_d)$ where H_d values are relatively small. Figure-4.13 shows the measured B values, together with the theoretical estimate B_{theo} calculated with the parameters deduced from the FMR study ($\frac{\gamma}{2\pi} = 30GHz/T$, $H_K = \frac{2K_s}{\mu_0 M_s t}$ with $K_s = 0.24mJ/m^2$, $\mu_0 M_s = 0.96T$) for each film. In spite of some dispersion for the 10 nm and 40 nm devices, we notice that the measured values follow the trend expected from the theory, i.e a clear decrease for small thickness. This trend is due to the surface anisotropy which reduces significantly the effective magnetization at a small thickness.

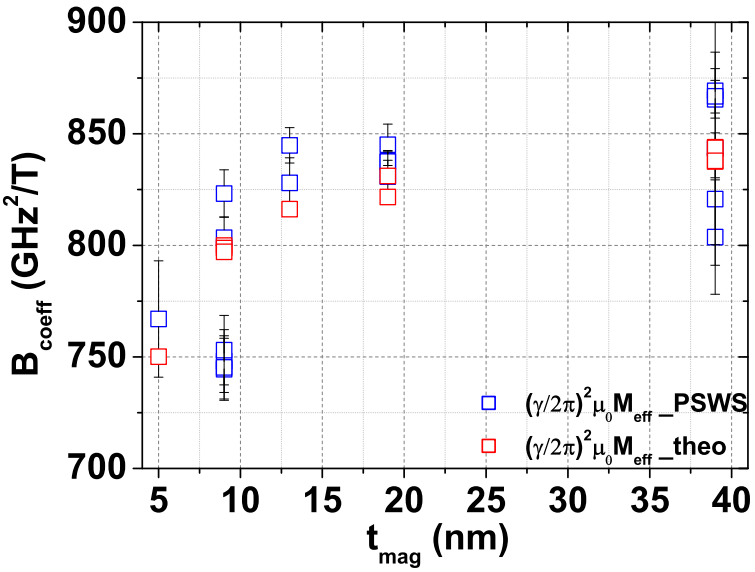

Figure 4.13: A comparison between the $(\frac{\gamma}{2\pi})^2 M_{eff}$ values obtained from the propagating spin wave spectroscopy technique (the blue square) and the theoretical expected values (the red squares).

The zero field frequency

From equation 4.5, it is clear that the parameter C, i.e the square of the frequency extrapolated to zero field is influenced by the wave vector (k) of the spin wave. Accounting for the out of plane anisotropy and the in-plane demagnetizing field, the theoretical estimate writes:

$$C_{theo} = (\frac{\mu_0 \gamma}{2\pi})^2 (\frac{M_{eff} M_s}{4}(1 - e^{-2kt}) - \frac{2}{\pi}\frac{t}{w} M_s M_{eff}). \tag{4.6}$$

The main panel of figure-4.14 shows the variation of the measured C coefficient as a function of the product between the wavevector k and the thickness t for all measured devices. The (kt) product represents a characteristic parameter in the magnetostatic theory. The inset of the figure-4.14 shows the percentage difference of the measured values from the theoretical calculated value of the C-parameters for the main and the secondary peak. We notice a full agreement between the 2 values to within an error bar of about 3%, for the main peak (the red rectangle) and the difference becomes larger for the values obtained from the secondary peak (15%).

As we have seen, the magnetic parameters of the thin films obtained using the propagating spin wave spectroscopy technique are consistent with the parameters obtained from the standard FMR measurements to within an acceptable experimental error. It indicates also that the magnetic properties of our films are not altered significantly during the lithographical processes and the propagating spin wave spectroscopy technique can be regarded as a suitable inductive broadband technique to study the magnetization oscillation modes with $k \neq 0$.

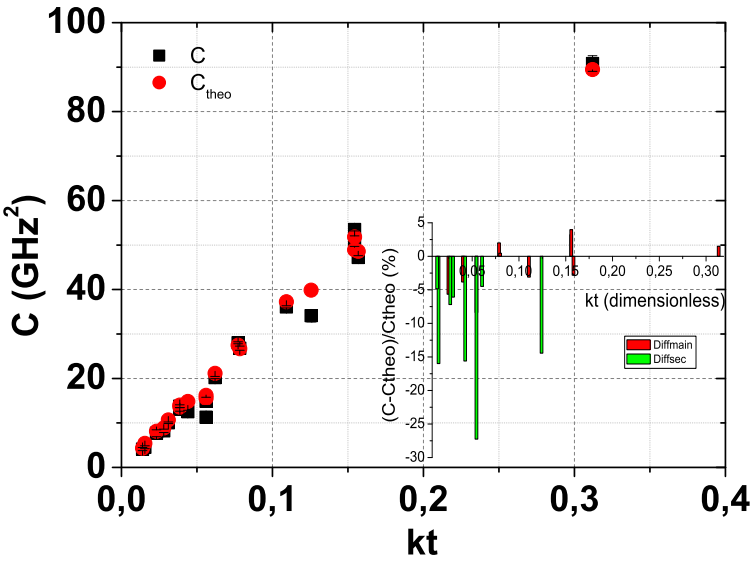

Figure 4.14: The measured and the calculated field independent parameter as a function of the product of the wavevector and the thickness. The inset shows the percentage difference between the measured and the expected values of the main and the secondary peak.

4.2.4 Interpretation of the measured linewidth

In FMR measurements, the linewidth is related to the relaxation process of the oscillations of the magnetization. However, when the excitation of the magnetization is performed using an antenna with a finite extension, an additional contribution to the linewidth is due to a non-monochromatic excitation of the spin waves. This extrinsic contribution to the line width is equal to $\Delta\omega_{ext} = v_g \Delta k$, where v_g is the group velocity and Δk is the width of the distribution of the wave-vector. In the magnetostatic surface wave configuration the intrinsic contribution $\Delta\omega_{int}$ and the extrinsic contribution to the line width $\Delta\omega_{ext}$ are obtained writing the products equation $\frac{\partial\omega}{\partial H}\Delta H$ and $\frac{\partial\omega}{\partial k}\Delta k$ respectively, they write:

$$\begin{aligned} \Delta\omega_{int} &= \alpha(\omega_H + \tfrac{1}{2}\omega_M), \\ \Delta\omega_{ext} &= \tfrac{\omega_M^2}{4\omega} t\Delta k. \end{aligned} \tag{4.7}$$

The total linewidth is a combination of the intrinsic and the extrinsic linewidth. If the 2 contributions give rise to Lorentzian peaks then the overall peak is also Lorentzian and its linewidth is written as:

$$\Delta\omega_{tot} = \Delta\omega_{int} + \Delta\omega_{ext}.$$

If the two contribution give rise to Gaussian peaks then the overall peak is Gaussian and its linewidth is written as:

$$\Delta\omega_{tot} = (\Delta\omega_{int}^2 + \Delta\omega_{ext}^2)^{\frac{1}{2}}.$$

An example of the measured linewidth is plotted in figure-4.15 for the w= 8 μm-t=10 nm device. Figure-4.15 shows the intrinsic and the extrinsic contribution, and their Lorentzian and Gaussian combination. We notice that the

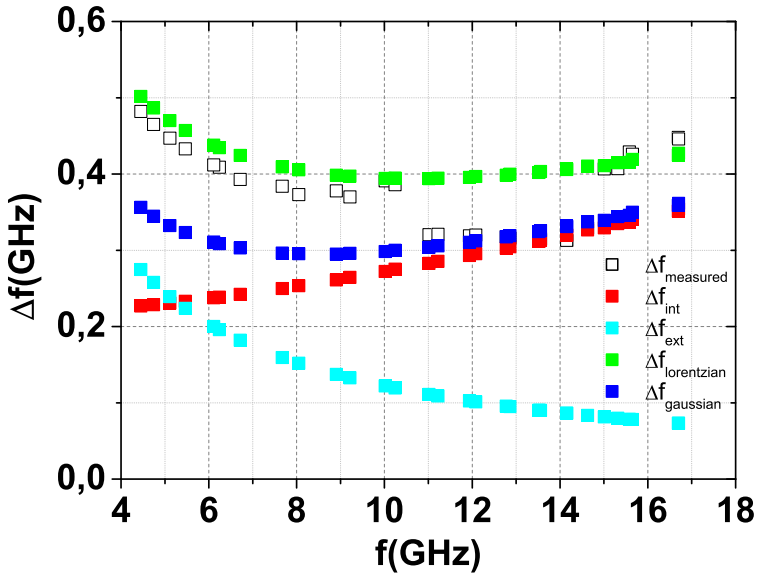

Figure 4.15: The variation of the linewidth as a function of the frequency. The measured linewidth is for the device (t=10 nm, w= 8μm). We use the damping coefficient α =0.0084 and the Δk= 0.75 μm^{-1}.

measured values fall between the two convolutions. The measured linewidth is therefore consistent with the damping value chosen here ($\alpha = 0.0084$ as deduced from the FMR study). However, it would not be possible to extract precisely the damping coefficient from the measured linewidth since the extrinsic contribution is large and varies significantly with the frequency. This is in contrast with the magnetostatic forward volume wave configuration, where the group velocity does not vary significantly with the frequency and one can follow the variation of the linewidth with the frequency to extract the damping coefficient as in [112].

4.3 Transmission measurements

In this section, we will analyze the transmission signal of the spin wave propagation in the magnetostatic surface wave configuration. This is not a trivial task because of the relatively high attenuation of the wave signal in a metallic film such as permalloy. A good understanding of the propagating characteristics of the spin wave in a Permalloy stripe will be essential for extracting accurately the Doppler shift in the next chapter.

4.3.1 Mutual inductance spectra

One of the advantages of the propagating spin wave spectroscopy technique is that one can measure the propagation characteristics of the spin waves in the magnetic material between the 2 antennas. The signals carrying this information are the two mutual inductance signals ΔL_{ij}. We perform 2 successive measurements: in the first measurement the spin waves are excited with the antenna connected to the port 1 of the VNA and the propagating waves are detected with the antenna connected to the port 2 of the VNA, this measurement corresponds to the mutual inductance signal ΔL_{21}. The second subsequent measurement corresponds to the reverse measurements where the excitation is done by the antenna connected to port 2 and the detection is done by the antenna connected to port 1 of the vector network analyzer which corresponds to the mutual inductance signal ΔL_{12}.
Figure-4.16 shows a typical measurement of the mutual inductance signals ΔL_{12} and the ΔL_{21} for the device (w=8 μm, t=10 nm). The top panel shows the real and the imaginary parts of the ΔL_{12}. We observe two distinct wavepackets centered on different frequencies (f_1 and f_2). The real and the imaginary parts show an oscillation behavior with a 90° phase shift. The blue line on the bottom panel shows the amplitude of the ΔL_{12}. One recognizes two peaks. Those two peaks are centered on the absorption peaks apparent on the ΔL_{11} signals (green lines). The two wavepackets are due to the excitation of the spin wave with different wavevectors (k_1 and k_2) corresponding to the main and the secondary excitation peaks. The middle panel shows the real and the imaginary parts of the ΔL_{21}, the signal is quite similar to the ΔL_{12}, except a global decrease in the amplitude, which is also apparent on the bottom panel. The difference in the amplitude of the 2 signals reflects the non-reciprocity character of the magnetostatic surface wave, which will be discussed in the next section.
The oscillations seen on both ΔL_{12} and ΔL_{21} are attributed to the accumulation of the phase delay by the spin waves during their propagation. The phase delay accumulated between the two antennas is given by $\Phi = kD$ where D is the separation distance between the two antennas and k is the wavevector of the wave. Since the excitation by the antennas is not monochromatic with a finite width Δk, the phase accumulation between the two antennae varies slightly as a function of the frequency.

In figure-4.17, we compare the measured spectra for two devices (w=8 μm, t=10 nm and w=2 μm, t=10 nm) under different applied fields. We notice that the wavepackets corresponding to k_1 and k_2 are well separated at low field and they interfere with each other to form one single wavepacket at a higher field. We observe that the amplitude of the main peak is higher than the amplitude of the secondary peak at low field, and they are of comparable amplitude at

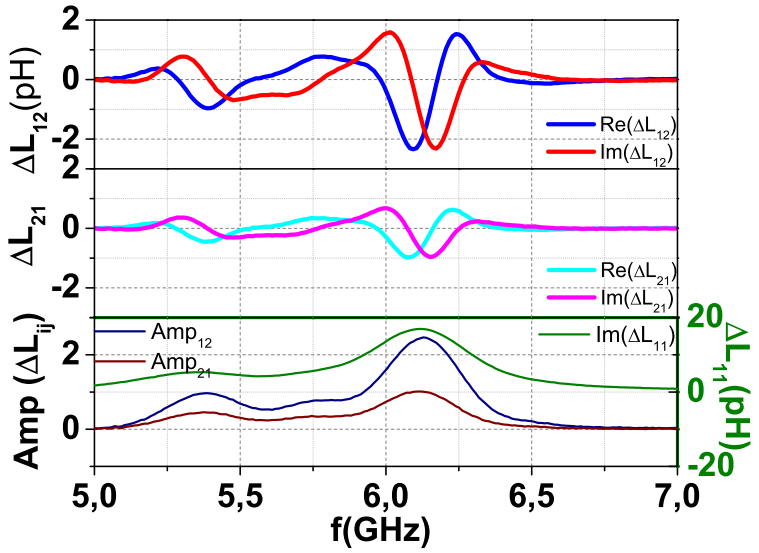

Figure 4.16: The typical mutual inductance signals for a device with the dimensions (t=10 nm, w=8 μm). We plot the real and the imaginary parts of the mutual inductance signals ΔL_{12} (top panel) and ΔL_{21} (middle panel) and also the amplitude of the 2 signals (bottom panel), in addition to the imaginary part of the ΔL_{ii} (bottom panel). The measurements were performed under an external field of 28 mT with the microwave power of -10 dB. The signals are obtained after 10 average with a bandwidth of 100 Hz.

a higher field. This is justified since at higher frequency the amplitude of the signal is more damped compared to the signal oscillating at the lower frequency. Now let us see how the information on the propagation of the spin waves can be extracted from the measured waveforms.

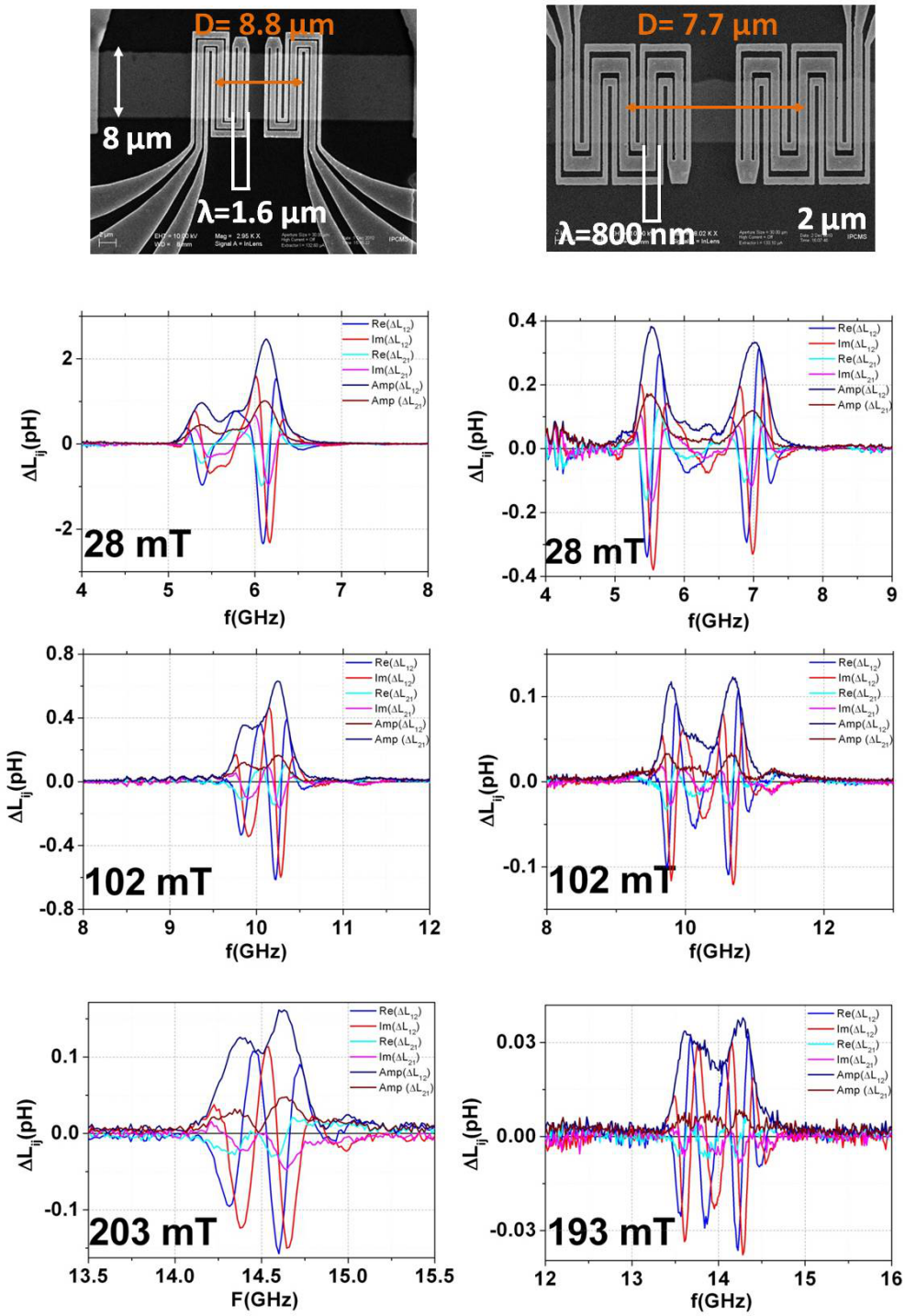

Figure 4.17: The mutual inductance signals for two devices: (w=8 μm, t=10 nm) and (w=2 μm, t=10 nm). In each panel we plot the real and the imaginary parts of the mutual inductance signals ΔL_{12} and ΔL_{21} and their amplitude. We also indicate the applied field on each panel. The measurements were performed at a power of -10 dB and with a bandwidth of 100 Hz. We average the signals 10 times.

4.3.2 Extraction and interpretation of the group velocity

The group velocity describes the transmission velocity of the envelop for a group of propagating waves at different frequencies. As an example, let us consider 2 spin waves having the same amplitude and oscillating with very close frequencies and phase constants:

$$\begin{array}{l} m_1 = m_0[e^{i(\omega_0+\Delta\omega)t-(k_0+\Delta k)x}] \\ m_2 = m_0[e^{i(\omega_0-\Delta\omega)t-(k_0-\Delta k)x}] \end{array} \tag{4.8}$$

We write the sum of the two oscillations $m = m_1 + m_2$ as:

$$m = 2m_0 e^{i(\omega_0 t - k_0 x)} \cos(\Delta\omega t - \Delta k x), \tag{4.9}$$

The factor $e^{i(\omega_0 t - k_0 x)}$ describes the propagation of the wave group along the x-axis, and the factor $\cos(\Delta\omega t - \Delta k x)$ describes a change of the amplitude along the x-axis. The envelop moves along the x-axis such as

$$(\Delta\omega t - \Delta k x) = constant. \tag{4.10}$$

The group velocity v_g is then:

$$v_g = \frac{\partial x}{\partial t} = \frac{\partial \omega}{\partial k}. \tag{4.11}$$

We deduce the group velocity of the magnetostatic surface waves by differentiating the MSSW dispersion 1.47 relation with respect to the wavevector and we obtain:

$$v_g = \frac{\omega_M^2 t}{4\omega} e^{-2kt}. \tag{4.12}$$

Experimentally, we measure the period of the oscillations f_p which is related to the time delay t_d as $t_d = \frac{1}{f_p}$. We deduce the group velocity using $v_g = D f_p$. For a given propagation direction, we measure the difference in frequency between the maximum of the real and the maximum of the imaginary part as shown in the inset of the figure-4.18. The measured frequency difference Δf corresponds to a quarter of the period f_p ($f_p = 4\Delta f$). At each field we measure Δf and we deduce the group velocity. In the main panel of the figure-4.18 we display the experimental and the theoretical values of the group velocity for a device (w=8 μm, t=10 nm). The group velocity decreases with the frequency, however one can notice a significant difference between the measured and the theoretical values. Such difference was observed for all devices as explained in the appendix B.

The difference originates from the determination of the distance traveled by the wave between the first and the second antenna. We assume the distance D to be from the center to the center of the antennas, which is certainly overestimated. Indeed, since the spin wave propagating below the antenna are attenuated, the propagation signals might be dominated by the signals generated near the edge of the first antenna and detected near the edge of the second antenna. The uncertainty on the propagating distance of the wave reflects also on an uncertainty over the attenuation length as we will see in the next section.

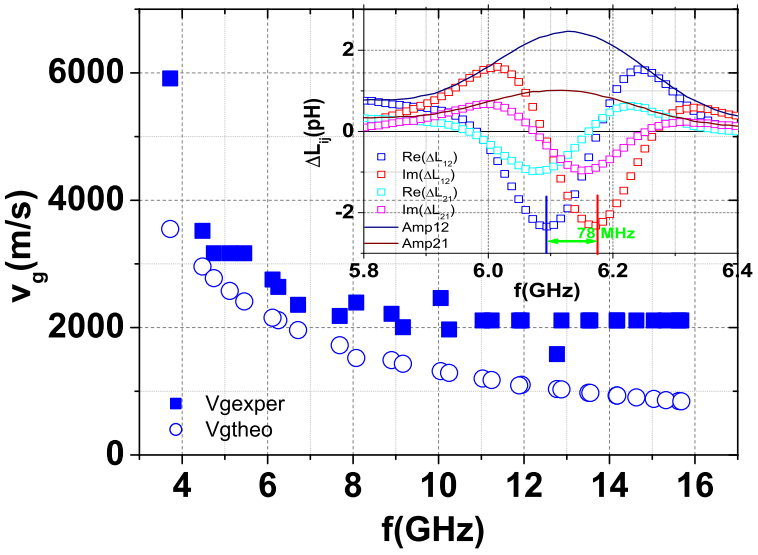

Figure 4.18: The inset shows the frequency difference between the real and the imaginary part at a field of 28 mT. The main panel displays the variation of the group velocity with the frequency for the measured and the theoretical value.

4.3.3 Extraction and interpretation of the attenuation length

In a dissipative medium the amplitude of an oscillating wave spatially decays with the distance. In a metallic ferromagnet with a significant damping coefficient the amplitude of the propagating spin wave between the 2 antennas will decrease with the distance due to the attenuation of the wave. The decay can be written as: $m = m_0 e^{-x/L_{att}} e^{i(\omega t - kx)}$ where L_{att} is the attenuation length over which the amplitude of the precession decays as 1/e. Experimentally, we determine the attenuation length by comparing the transmitted (ΔL_{12} or ΔL_{21}) signals to the reflected signal (ΔL_{11} or ΔL_{22}). The $\Delta L'_{ii}s$ are related to the power pumped from the excitation signal to the spin waves, and the $\Delta L'_{ij}s$ are related to the power transmitted via the spin waves. In a non reciprocal configuration, the transfer of power into spin waves propagation in the positive and the negative directions is different. Therefore, we define a ratio of the sum of the amplitudes of the two transmission signals to the amplitude of the reflection signal. This ratio is related to the attenuation length L_{att} and the antenna distance D:

$$\frac{\mid \Delta L_{ij} \mid + \mid \Delta L_{ji} \mid}{\mid \Delta L_{ii} \mid} = e^{-D/L_{att}}. \tag{4.13}$$

Theoretically, we determine the attenuation length from the group velocity (equation 4.12) and the relaxation time of the magnetization T_2 as:

$$L_{att} = v_g T_2 = \frac{\omega_M^2 t}{4\omega} e^{-2kt} \frac{1}{\alpha(\omega_0 + \frac{\omega_M}{2})}, \tag{4.14}$$

Figure-4.19 shows the variation of the attenuation length with the applied field for the the device (w=8 μm, t=10 nm). We notice the attenuation length

decreases as we increase the applied field. We notice a significant discrepancy between measured and theoretical values of the L_{att}. As explained in the 4.3.2, we attribute this discrepancy to the inaccurate determination of the effective distance between the two antennas. The measured attenuation length is roughly $< 5\ \mu m$ which is comparable to the lateral extension of the antenna and smaller than the center to center distance. This observation suggests that the effective distance is close to the distance between the extremity edges of the antennas.

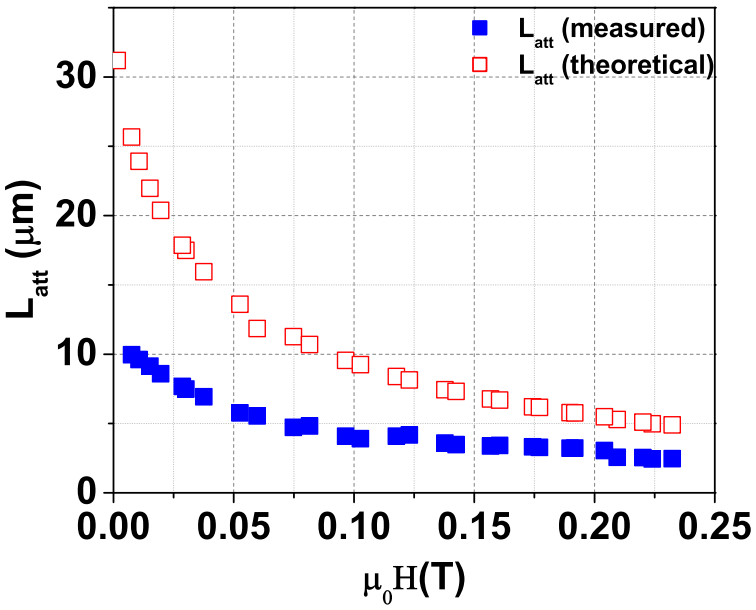

Figure 4.19: The variation of the attenuation length with the applied magnetic field. The measured L_{att} is calculated using equation 4.13. The theoretical L_{att} is calculated from 4.14

4.4 Non-reciprocity

For wave propagation, reciprocity means that the waves propagating in opposite directions have the same properties. In specific cases, non-reciprocity may happen i.e the propagation in the 2 opposite directions occurs with a different amplitude and at a different frequency. As we have seen in the first chapter, the magnetostatic surface wave MSSW has such non-reciprocity properties. The non-reciprocity character of the magnetostatic surface waves was reported first in the yttrium iron garnet (YIG) films [17] and discussed by Mills in semi-finite ferromagnets [76] . Recently, the non-reciprocity in amplitude [28] [93][94] and in frequency [2] were reported in ferromagnetic metal thin films.
In the following we describe the amplitude and frequency non reciprocity in our devices. To address this issue we perform 2 successive measurements of the propagating spin waves. In the first measurement the spin waves are excited by the antenna (1) and detected by the antenna (2), this wave corresponds to the mutual inductance signal ΔL_{21} which define the positive propagation ($k > 0$) and in the second measurement the spin waves are excited by the antenna (2) and detected by the antenna (1), which corresponds to the mutual inductance signal ΔL_{12} which defines the negative propagation ($k < 0$).

4.4.1 Amplitude non-reciprocity

As already noticed when comparing the mutual inductance signals ΔL_{12} and ΔL_{21}, the amplitude of the spin wave propagating in one of the direction is strongly decreased. We notice that the negative propagation ΔL_{12} has a higher signal amplitude than the positive propagation ΔL_{21} for the measurements performed with a positive direction of the magnetization. For the example given in the top panel of figure-4.20, the ratio of the amplitude of the negative propagation $A(-k)$ to the amplitude of the positive propagation $A(+k)$ is roughly 2.5. As we reverse the direction of the static magnetization from $+M$ to the $-M$ direction, we observe the $+k$ propagation direction has the higher amplitude instead of the $-k$ direction with the same factor of the amplitude between the 2 signals (bottom panel of figure-4.20). This behavior is confirmed in figure-4.21, where we plot the variation in the amplitude of the ΔL_{12} and ΔL_{21} signals measured as a function of the field.

The amplitude non-reciprocity is due to the coupling of the excitation with the oscillating spin waves. The microwave current creates the oscillating magnetic field **h** which couples to the magnetization modes in the permalloy film. The excitation field **h** lies in the xy plane perpendicular to the direction of the static field. Both the x and the y components contribute to the excitation of the precessional motion of the magnetization. The coupling of the excitation field with the dynamical magnetization will be stronger for one propagation direction than the other. Figure-4.22 shows the coupling of the excitation field with the spin waves propagating in the $k > 0$ and $k < 0$ direction at the same direction of the applied field $H < 0$. In both cases the x-component of the excitation field is in phase with the x component of the magnetization oscillation, however the y component of the excitation field is in-phase with that of the magnetization oscillation only in the $k < 0$ case. Hence, the signal amplitude will be higher for the $k < 0$ than the $k > 0$ direction. Consequently, the amplitude depends

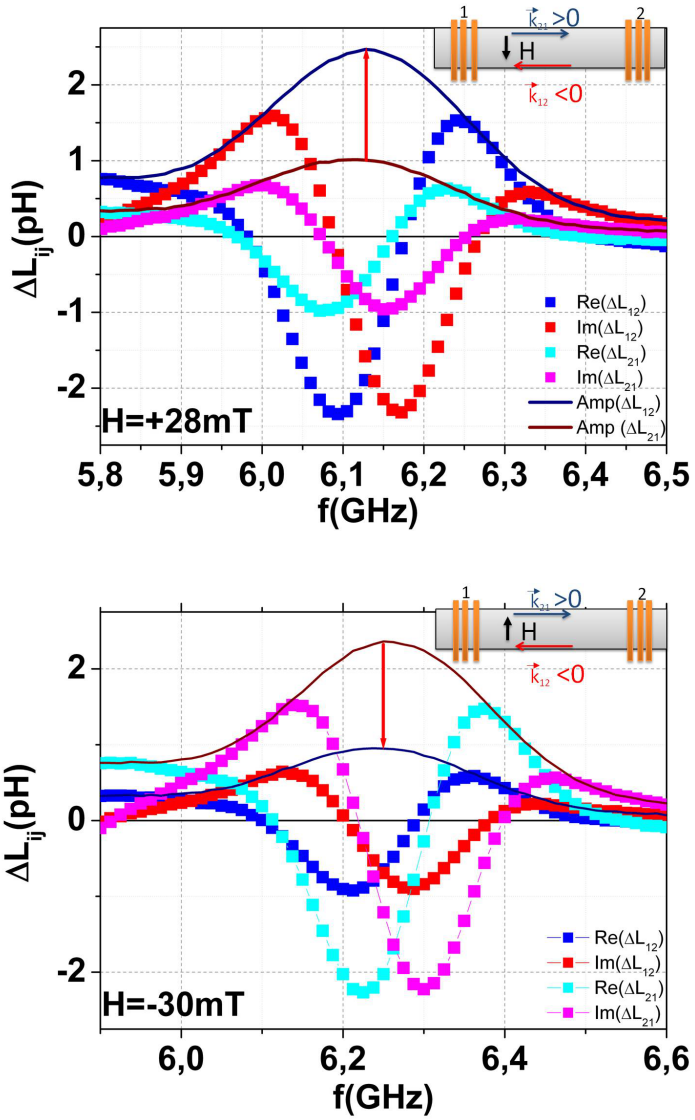

Figure 4.20: The mutual inductance signals for the device (w=8 μm, t=10 nm). The amplitude difference of the ΔL_{12} and the ΔL_{21} signals indicate a strong amplitude non reciprocity character of the MSSW. The measurements were performed under an applied field of (+28 mT) and (-30 mT).

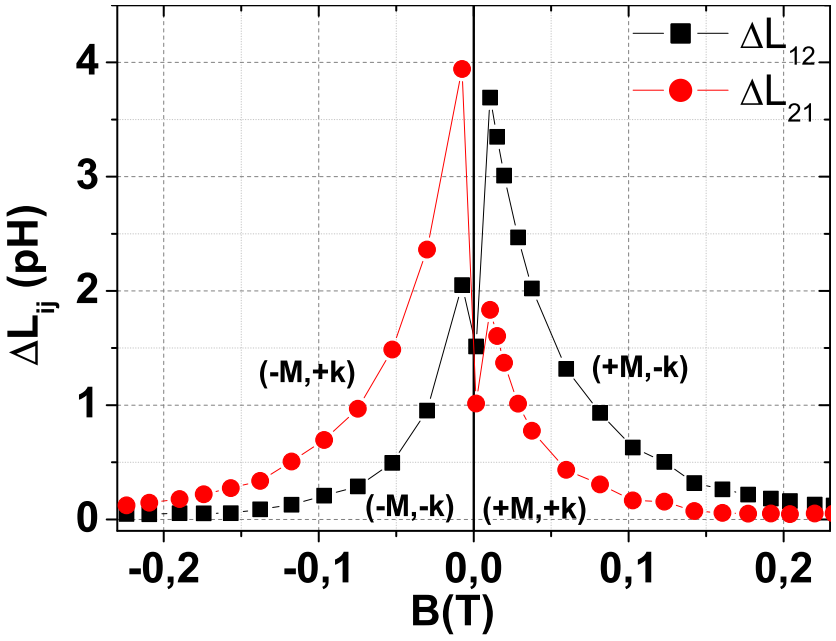

Figure 4.21: The variation of the amplitude for the ΔL_{12} and the ΔL_{21} signals with the four combination of the magnetization and the wavevector directions.

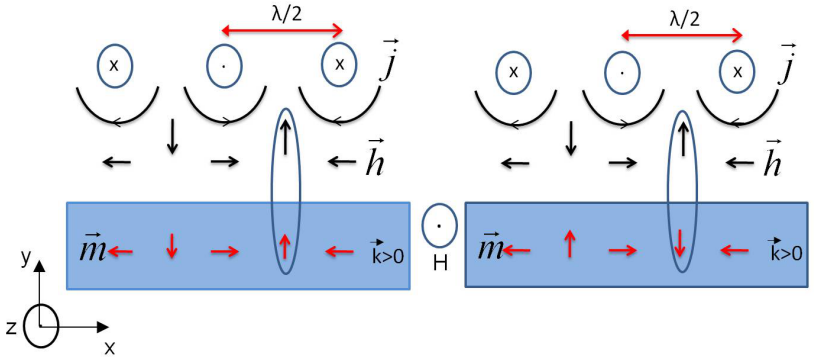

Figure 4.22: An illustration cartoon for the coupling between the excitation field and the dynamical magnetization for the $k > 0$ and $k < 0$ propagation, the static is oriented in a negative field.

on the relative polarity of the dynamical magnetization and the excitation field. The polarity of the dynamical magnetization is influenced both by the propagation or by the magnetization directions, which explains the dependence of the amplitude on the (k) and (M) directions.

4.4.2 Frequency non-reciprocity

According to the dispersion relation of the magnetostatic surface wave we expect that the two opposite propagation should have the same resonance frequency. However, under certain conditions the dispersion relation depends on the propagation direction of the spin wave. Such case was reported already in the YIG film [103], in the ferrite films [73], and recently in permalloy thin films [2]. In these studies a metallic ground close to the ferromagnetic films causes the dispersion relation to depend on the propagation direction. In the measured devices the ferromagnetic films are capped with a dielectric (Al_2O_3) on the 2 surfaces.
We compare the frequencies of the mutual inductance signals ΔL_{12} and ΔL_{21} and we notice a frequency shift of the order of ten MHz. For the measurements shown in the figure 4.23, we observe the $k > 0$ propagation lags behind the $k < 0$ propagation for the positive field. Again, the lag is reversed as we reverse the direction of the static magnetization. In this example, the frequency shift between the 2 signals is about 17 MHz.

Device	k μm^{-1}	40 nm	20 nm	14 nm	10 nm	6 nm
8 μm	3.86	29	29	X	15	11
8 μm	1.55	X	11	X	6	X
3 μm down	3.87	31	X	X	13	X
3 μm down	1.4	12	X	X	6	X
3 μm up	7.8	36	X	32	X	X
3 μm up	3.14	27	X	10	X	X
2 μm	7.84	X	X	X	21	X
2 μm	2.8	X	X	X	11	X

Table 4.4: The frequency non reciprocity (in MHz) measured for different devices for the main and the secondary peak at a field of 28 mT.

A magnetostatic surface wave is more localized near one surface (top or bottom, depending on its propagation direction), and hence it is sensitive to any difference between the the upper and the lower surface. We might assume that in our samples, the top and the bottom interfaces have different surface anisotropy K_{s1} and K_{s2}. Consequently, the wave having more amplitude on the top surface is expected to oscillate at a slightly different frequency compared to the wave propagating on the bottom surface. The frequency shifts between the 2 signals is given in the table 4.4 for different devices. The quantitative understanding of this frequency shift is left for future work.

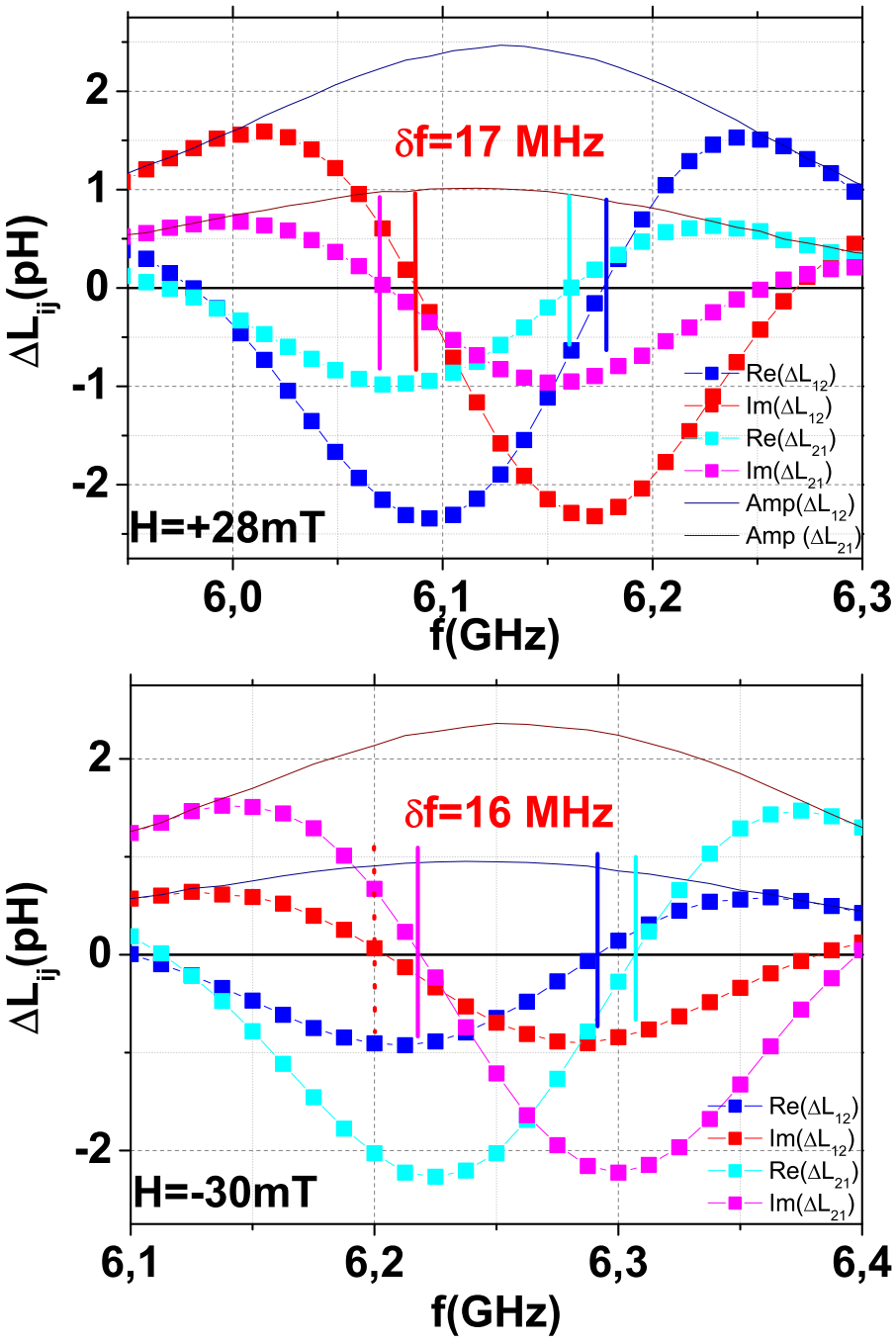

Figure 4.23: The frequency non-reciprocity measured between the k>0 and k<0 signals for the film (t=10 nm, w= 8 μm).

Conclusion

In the first part of this chapter, we have used the propagating spin wave spectroscopy to extract the magnetic properties of the thin film as if it were a FMR technique with $k \neq 0$. The extracted magnetic parameters are in reasonable agreement with the ones measured by standard FMR given in the previous chapter 3. It indicates that the magnetic characteristics of the films are not altered after the fabrication processes.
In the second part, we have analyzed the propagation characteristics of the spin wave, and a qualitative picture of the propagating wave characteristics is drawn (velocity, attenuation length). However, a more quantitive extraction of these parameters would require an extra work. The analysis of the transmission signal (oscillation, period,..) provides us with sufficient background to extract the current induced Doppler shift when the DC current is turned on.
In the last part, we have discussed a crucial property of the magnetostatic surface waves which is the non reciprocity character. A non-reciprocity in amplitude and in frequency is observed in our thin films. Understanding the propagation characteristics and the non reciprocity peculiarity is a prerequisite for analyzing the current induced spin wave Doppler shift when the DC current is injected through the ferromagnetic stripe as we will see in the next chapter.

Chapter 5

Film thickness dependence of the current-induced spin wave Doppler shift

The electrical transport properties of the transition metals (Fe, Co, Ni) and their alloys are conveniently described within the two-current model [43]. The spin-dependent resistivity associated to the impurities and to the phonons could be extracted using binary and ternary alloys measurements. Recently, a new method based on the current induced spin wave Doppler shift [111], has been proposed by our group to measure directly the degree of the spin polarization of the electrical current in ferromagnetic thin films. A thickness dependence study was performed in the frame of this thesis work in order to understand the role of the surface in the spin dependent transport and to identify the contribution of the surface scattering to the spin up and spin down resistivities.

The remaining of this chapter explains how we have extracted this information. It is divided in four sections. In the section-§5.1, the current induced spin wave Doppler shift technique is presented. In the section-§5.2, a complete analysis of the mutual inductance signal in the presence of an electrical current is given together with the exact procedure used for extracting the current induced spin wave Doppler shift. Section-§5.3 presents the main result of this manuscript, i.e the film thickness dependence of the degree of the spin polarization extracted from the Doppler shift measurements. In the last section-§5.4 we try to interpret the results in the frame of the two current model with and without spin-flip scattering.

5.1 The current-induced spin wave Doppler shift experiment

The current induced spin wave Doppler shift (CISWDS) experiment is a recent technique allowing one to measure directly spin current or equivalently the degree of the spin polarization of the electrical current (see §2.4.3).
It can be measured using a modified version of the propagating spin wave spectroscopy in which a DC current is allowed to flow along the ferromagnetic stripe. In this section we will present the experimental setup of the current induced spin wave Doppler shift technique and we will discuss the expected Doppler symmetry.

5.1.1 The experimental setup

To observe the Doppler effect, the ferromagnetic stripe is connected to four DC pads for the electrical current, in addition to the antennas for the propagating spin wave spectroscopy as we already mentioned in the sample fabrication section (§4.1). Four needle-like tungsten probes are in contact with the DC pads and are connected to a sourcemeter (Keithley 2600). Two of the probes are used to source the DC current along the ferromagnetic stripe and the other two are used to measure the voltage as we perform four point resistivity measurements. The probes are mounted on micropositioners and the alignment of the probers over the DC pads is done using a microscope. A scheme of the setup is shown in the figure 5.1.
The effect of the DC current is to induce a Doppler shift in the frequency of the propagating spin wave. For example as shown in the figure-5.1, the frequency of a spin wave propagating from the antenna 1 to the antenna 2 decreases as the dc current passes in the same sense as the wave and it increases for the wave propagating from the antenna 2 to the antenna 1.

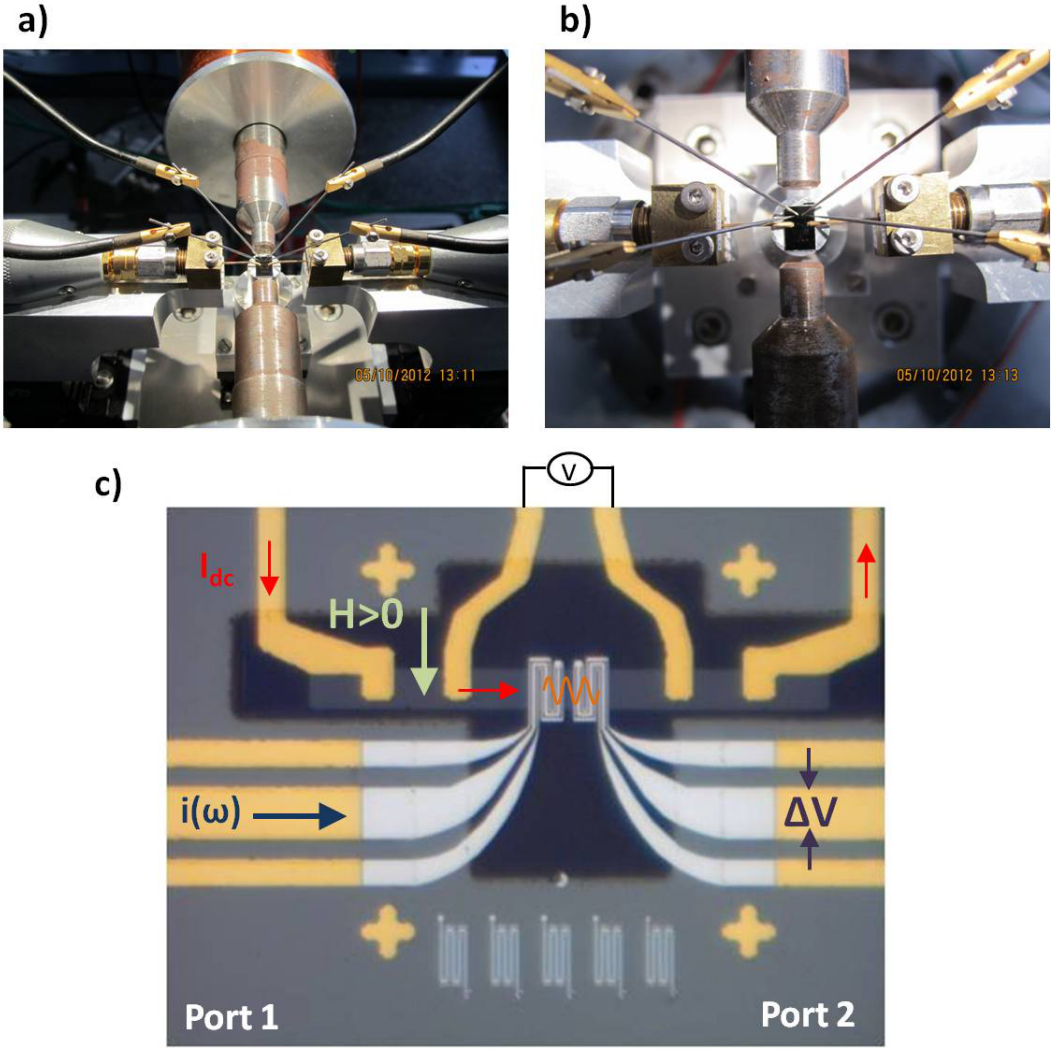

Figure 5.1: a) Picture of the experimental setup for the CISWDS, b) a zoom in to show the needles, c) image of a fabricated device used in the current induced spin wave Doppler shift measurements. It shows the direction of the current flowing through the magnetic stripe.

5.1.2 The expected Doppler symmetry

As we have seen before, the DC current exerts a torque on the spin waves leading to a Doppler frequency shift. To illustrate how the Doppler shift shows up, we show in figure-5.2 examples of a propagating spin wave spectra under a DC current. In panel (a) ($k > 0$) we see that a positive current +I (blue curve) decreases the spin wave frequency compared to the same wave with an opposite current polarity (red curve). The effect is reversed for $k < 0$ (panel b): i.e the negative current polarity -I (red curve) decreases the spin wave frequency compared to the same wave with +I current polarity (blue curve).
As we reverse the direction of the magnetic field from +H to -H as shown in the figure 5.2 c and d the symmetry of the effect is the same.
These observations are consistent with the symmetry expected for the Doppler shift. We will now discuss in more details the magnitude of the observed shifts.

5.2 The mutual inductance measurements in presence of a DC current

In the original work of the current induced spin wave Doppler shift the measurements were done using the magnetostatic forward volume wave. In this configuration it was sufficient to take the frequency difference between two opposite propagating wave at the same current to extract the CISWDS frequency [111]. In the present work the spin waves are excited with the so-called magnetostatic surface wave configuration. The advantage is that the signals are bigger and easier to measure. However, due to the non-reciprocity the simple extraction procedure of the CISWDS becomes invalid. In this section, we will show how we extract the current induced spin wave Doppler shift from the measured mutual inductance signals.

5.2.1 Current induced frequency shift and frequency non-reciprocity

In the magnetostatic surface wave configuration, we measure a frequency non-reciprocity between ΔL_{21} ($k > 0$) and ΔL_{12} ($k < 0$) propagations even in the absence of a dc current ($I = 0$) as we have seen in section 4.4. As we introduce a dc current $\pm I$ through the permalloy stripe, the Doppler shift effect will add a frequency shift $\mp\Delta f_{doppler}$ for the frequency of the ΔL_{21} signal and $\pm\Delta f_{doppler}$ for the frequency of the ΔL_{12} signal. The frequency difference between the ΔL_{12} and ΔL_{21} signals at a given current will be a combination of the frequency non reciprocity and the current induced spin wave Doppler shift. Figure-5.3 shows the data of figure 5.2-a, b plotted on the same graph and zoomed in. To estimate the frequency shift we measure the frequencies at which the curves cross the x-axis. The frequency difference between the $\Delta L_{12}(+I)$ and $\Delta L_{21}(+I)$ is about 20.4 MHz, whereas it is about 11 MHz between the $\Delta L_{12}(-I)$ and $\Delta L_{21}(-I)$. The explanation of this difference is related to how the frequency non reciprocity and the Doppler shift are combined together. The frequency shift between $\Delta L_{12}(\pm I)$ and $\Delta L_{21}(\pm I)$ are given as:

$$\begin{aligned} \Delta f(+I) &= f_{12}(+H,+I) - f_{21}(+H,+I) = \delta f_{NR} + 2\delta f_{dop} \\ \Delta f(-I) &= f_{12}(+H,-I) - f_{21}(+H,-I) = \delta f_{NR} - 2\delta f_{dop}, \end{aligned} \tag{5.1}$$

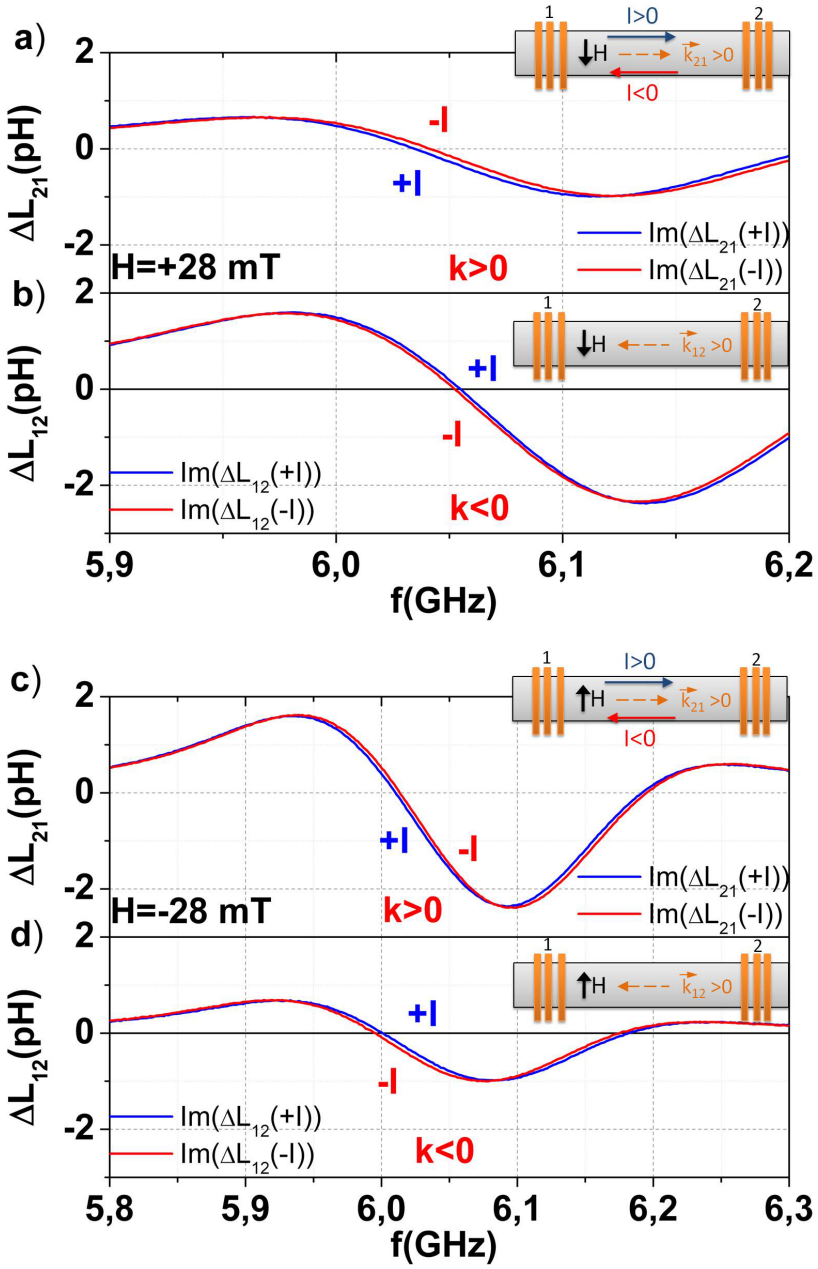

Figure 5.2: The imaginary parts of the mutual inductance signals measured for different directions of I, k, H. The measurements were done under a DC current of 7.5 mA, for the device with t= 10 nm, and w= 8 μm.(a) ΔL_{21} signals measured for I=+7.5 mA and I=-7.5 mA (blue and red curve respectively) under a field of +28 mT. (b) same for ΔL_{12} signals. (c)-(d) same as (a) and (b) for a field of -28 mT.

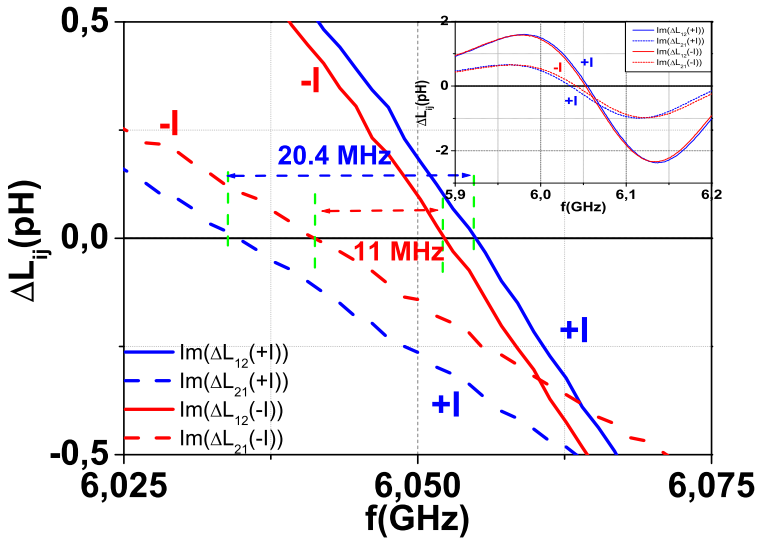

Figure 5.3: The inset panel display the imaginary parts of the mutual inductance signals. The main panel is a zoom in to show the frequency shift measured between the imaginary parts of the mutual inductance signals for ΔL_{21} and ΔL_{12}. We perform 2 measurement: the first measurement is performed with a positive dc current and the second measurement with a negative current through the ferromagnetic stripe. The measurements were done with an applied field of 28 mT and a dc current of 7.5 mA, for the device of t= 10 nm, and w= 8 μm.

where $f_{ij}(\pm H, \pm I)$ is the frequency for which the imaginary part of the signal ΔL_{ij} crosses zero.

5.2.2 The symmetry analysis

To avoid the complication of the frequency non reciprocity, we measure the Doppler shift for a given propagating direction, by comparing the two directions of the dc current $\pm I$.
The top and bottom panels of the figure-5.4 show a zoom of the spectra $Im(\Delta L_{21})$ and $Im(\Delta L_{12})$ respectively. Clearly, one could notice that the +I and -I signals are shifted according to the expected symmetry of the Doppler effect as discussed earlier (see §5.1.2). However the magnitude of the frequency shift is not

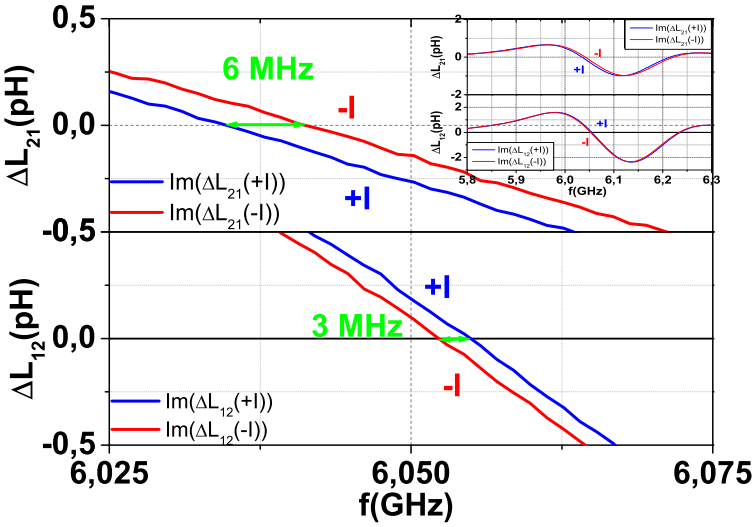

Figure 5.4: Estimate of the frequency shift between the imaginary part of the mutual inductance signals at + I and -I current for ΔL_{21} and ΔL_{12} in the top and bottom panel respectively. The measurements were done with an applied field of 28 mT and a dc current of 7.5 mA, for the device of t= 10 nm, and w= 8 μm.

the same for the two directions, it is 6 MHz for $k < 0$ and 3 MHz for $k > 0$. Basically, if the frequency shift were only due to the current induced spin wave Doppler shift, it should be the same for the two directions of the current. Consequently, we expect the measured frequency shift is not only due to the CISWDS. Apparently, the Doppler shift is combined with another current induced effect.

To investigate the nature of this additional frequency shift, we perform a symmetry analysis by measuring the frequency shifts $\Delta f_{ij} = f_{ij}(+I) - f_{ij}(-I)$ for the two direction of the field +H and -H. In the figure-5.5 the results of

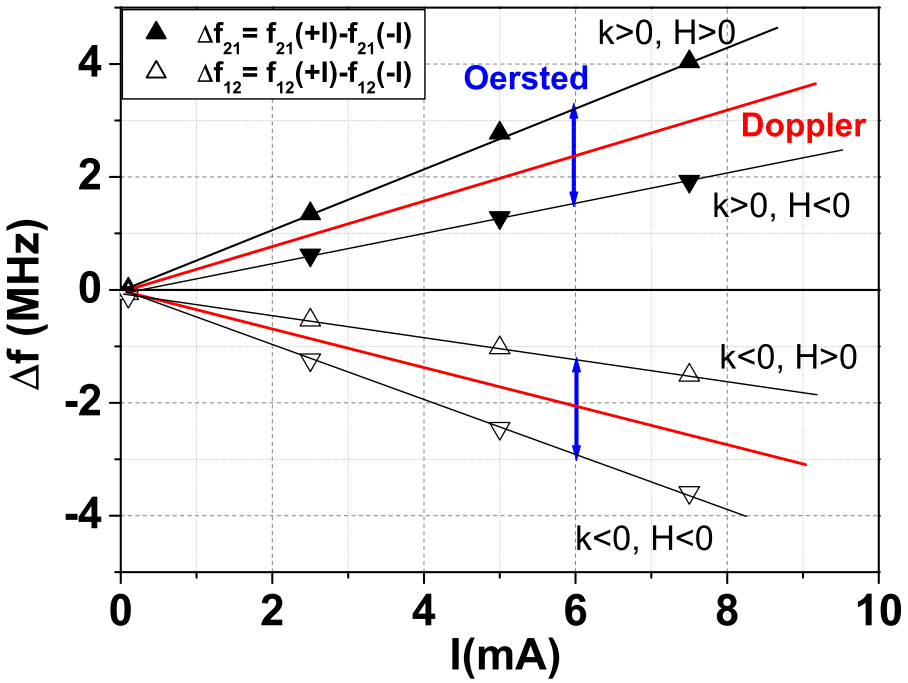

Figure 5.5: The frequency shift measured between the imaginary part of the $\Delta L_{ij}(+I) - \Delta L_{ij}(-I)$ as a function of the dc current for $H > 0$ and $H < 0$ for +k and -k propagations. The measurements were done with an applied field of ±28 mT for the device of t= 10 nm, and w= 8 μm.

the symmetry analysis are presented. One can clearly notice that for a given propagation direction k the frequency shift for the positive field +H is different than the frequency shift of the negative field -H. Moreover, one can notice that the frequency difference between $H > 0$ and $H < 0$ is the same for $k > 0$ and for the $k < 0$ directions. Apparently, the additional frequency shift coupled with the Doppler effect changes sign as we change the field direction from +H to -H. We attribute the additional frequency shift to be due to the Oersted field contribution as described below.

5.2.3 Oersted field contribution to the CISWDS

When a DC current flows across a conductor it generates a magnetic field named the Oersted field. This field modifies slightly the applied field. The combination of the Oersted field and the applied field depends on the relative sign between the direction of the field and the direction of the current. It depends on the location with respect to the axis of the stripe. In a perfectly symmetric conductor, the contributions of the Oersted field of the top and bottom halves of the

films cancel out, and hence no additional frequency shift should be observed. However, if the top and the bottom parts of the ferromagnetic stripe are not equivalent, the Oersted field could contribute to the frequency shift, with the symmetry observed in figure-5.5. The difference between the top and the bot-

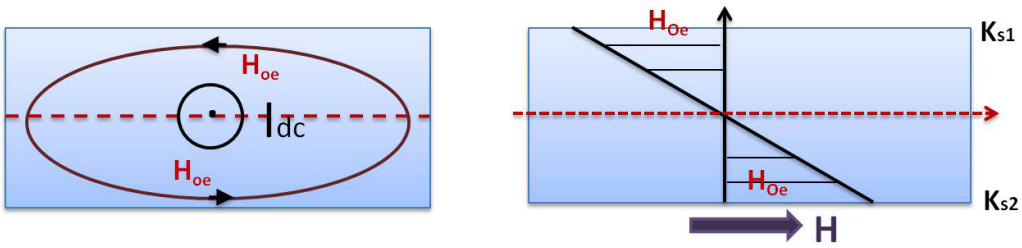

Figure 5.6: A schematic drawing illustrating a possible origin of the current induced frequency shift due to the Oersted field contribution. In a medium where the top and the bottom surfaces have different surface anisotropy the Oe field contribute to the an additional shift of the applied field and hence to the frequency shift.

tom parts of the films may be attributed to different surface anisotropies of each surface (K_{s1} and K_{s2}) as shown in the figure-5.6. Another origin may be some inhomogeneity in the films properties over the thickness.
At this point we differentiate between three sources for the frequency shift in the presence of a dc current and one can determine the contribution of each by following the corresponding symmetry. We summarize the symmetry of each frequency contribution in the table 5.1. The way those three contributions combine together is sketched on the level diagram shown in figure-5.7.

frequency	H	k	I
f_{NR}	odd	odd	X
f_{dop}	X	odd	odd
f_{Oe}	odd	X	odd

Table 5.1: The symmetry for the different sources of the frequency shift contributions in the thin films.

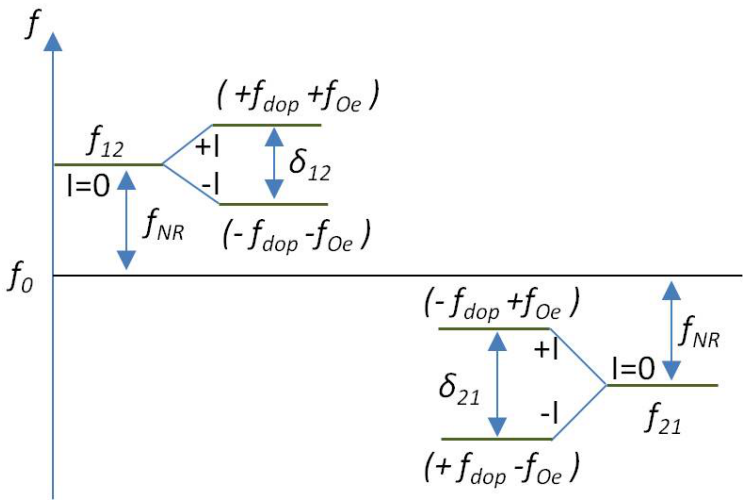

Figure 5.7: Combined effects of the frequency non-reciprocity, Oersted field and the Doppler shift.

5.2.4 A way to extract the Doppler shift

After we identify the different frequency shifts which contribute in the experiment, a reproducible and accurate enough process is needed to extract the current induced spin wave Doppler shift. The process we have chosen consists in extracting the phase change from the mutual inductance signals.
To understand this process, let us first define a function accounting for the shape of the observed oscillatory mutual inductance signals. A good fit is obtained by taking the product between an oscillatory function and a Gaussian peak. The form of the signal (S) can be reproduced with the function:

$$S = \frac{A}{w\sqrt{\frac{\pi}{2}}} \exp(\frac{-2(f-f_c)^2}{w^2}) \exp(j2\pi(f-f_{ref})/f_{per}), \tag{5.2}$$

where A, w, f_c are the area, linewidth at half maximum, and the center frequency of the gaussian envelop and f_{ref}, f_{per} are the parameters of the oscillatory function. (f_{ref} is the reference frequency for which the imaginary part is zero and the real part is maximum, and f_{per} is the period of the oscillation).
Figure-5.8 displays an example of a fit for the real and the imaginary parts of the mutual inductance signals ΔL_{ij} with the proposed form of the signals. One can notice the congruence between the measured data and the proposed function.

Let us now examine how the function S is expected to change in the presence of a current. Two effects are expected: a frequency shift δ and a relative change in the amplitude ε. The function S is slightly modified to the form S^+ and S^-

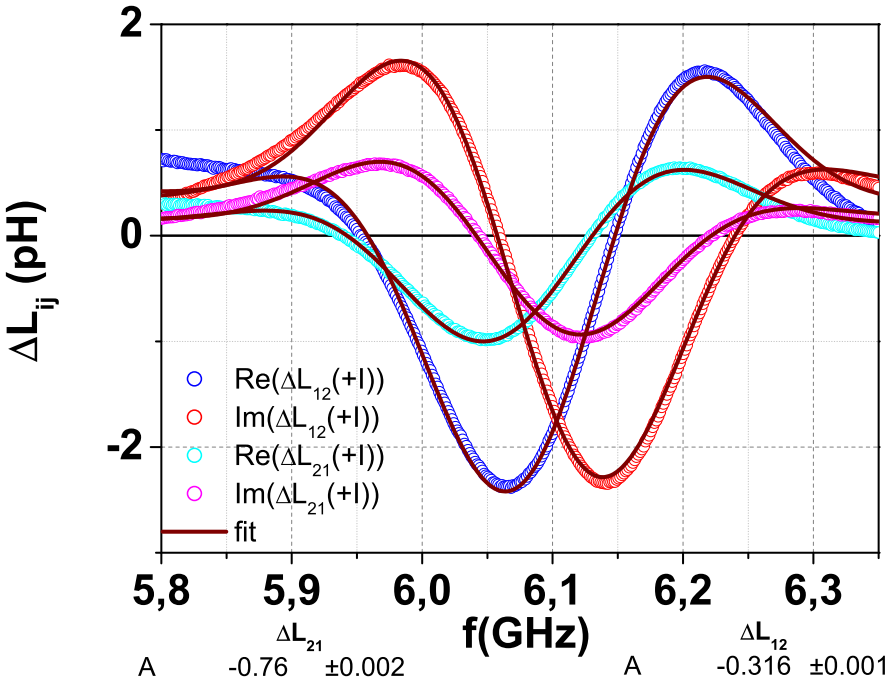

	ΔL_{21}			ΔL_{12}	
A	-0.76	±0.002		-0.316	±0.001
fc	6.099	±0.0005	GHz	6.081	±0.0005
w	0.201	±0.001	GHz	0.204	±0.001
fref	6.046	±0.0003	GHz	6.031	±0.0003
fper	0.441	±0.002	GHz	0.430	±0.002
re0	0.347	±0.01	pH	0.133	±0.004
im0	0.433	±0.01	pH	0.170	±0.0038

Figure 5.8: The form of the mutual inductance signal is perfectly reproduced with the function S defined in equation 5.2. The parameter of the signals are shown in the table for the +k and -k directions. The measurements were done with an applied field of 28 mT and a dc current of 2.5 mA, for the device of t= 10 nm, and w= 8 μm.

for the positive and the negative current direction as:

$$\begin{aligned} S^{+} &= (1+\varepsilon)\frac{A}{w\sqrt{\frac{\pi}{2}}}\exp(\tfrac{-2(f-f_c-\delta)^2}{w^2})\exp(j2\pi(jk(f-f_{ref}-\delta)/f_{per})) \\ S^{-} &= (1-\varepsilon)\frac{A}{w\sqrt{\frac{\pi}{2}}}\exp(\tfrac{-2(f-f_c+\delta)^2}{w^2})\exp(j2\pi(jk(f-f_{ref}+\delta)/f_{per})). \end{aligned} \tag{5.3}$$

Developing equation-5.3 at first order in ε and δ one gets

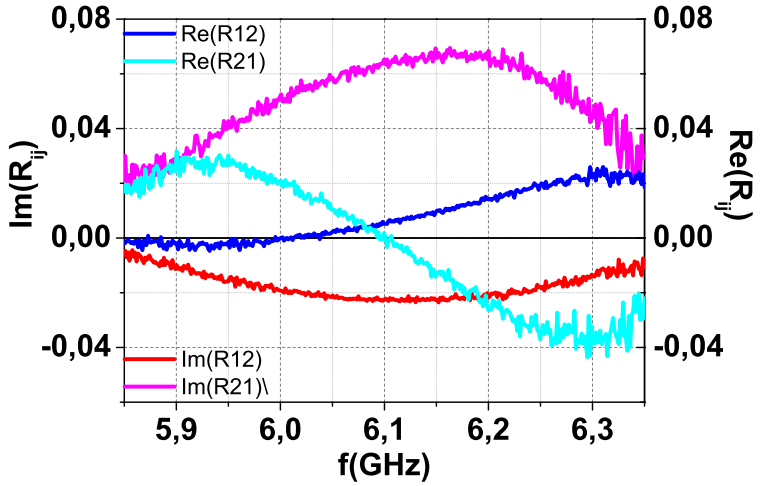

Figure 5.9: The real and the imaginary parts of the R_{ij} function for the +k and -k propagation. The measurements were done with an applied field of 28 mT and a dc current of 7.5 mA, for the device of t= 10 nm, and w= 8 μm.

$$\begin{aligned} Re(\tfrac{S^{+}-S^{-}}{S^{+}+S^{-}}) &= \varepsilon - 4\delta\tfrac{f-f_c}{w^2}, \\ Im(\tfrac{S^{+}-S^{-}}{S^{+}+S^{-}}) &= -\tfrac{2\pi\delta}{f_p} \end{aligned} \tag{5.4}$$

This suggests how to combine the $\Delta L_{ij}(+I)$ and $\Delta L_{ij}(-I)$ signals to extract a quantity directly proportional to the CISWDS. We define the function R_{ij} as:

$$R_{ij} = \frac{\Delta L_{ij}(+I) - \Delta L_{ij}(-I)}{\Delta L_{ij}(+I) + \Delta L_{ij}(-I)}, \tag{5.5}$$

The real and the imaginary parts of the R_{ij} signals are shown in the figure 5.9. As indicated by equation-5.4 the imaginary part of the R_{ij} signals is proportional to the δ_{ij}:

$$Im(R_{ij}) = \frac{-2\pi\delta_{ij}}{f_p}, \tag{5.6}$$

The f_p is obtained from the fit of the ΔL_{ij} signals. Using this method, one has a direct access to the current induced frequency shift.
In a similar way the real part of the R_{ij} depends on the relative change of the amplitude ε_{ij}:

$$Re(R_{ij}) = \varepsilon_{ij} - 4\delta_{ij}\frac{f-f_c}{w^2}, \tag{5.7}$$

In the coming discussion we deal mainly with the imaginary parts of the signals since in this manuscript we focus on measuring the current induced frequency shift.

How do we proceed with the data?

First, the frequency at the maximum amplitude of mutual inductance as shown in the inset of the figure-5.10 is noted, then we read the magnitude of the $Im(R_{ij})$ signal at that position as indicated in the main panel of the figure-5.10. And, from equation-5.6 the shift in the frequency δ_{ij} is extracted.

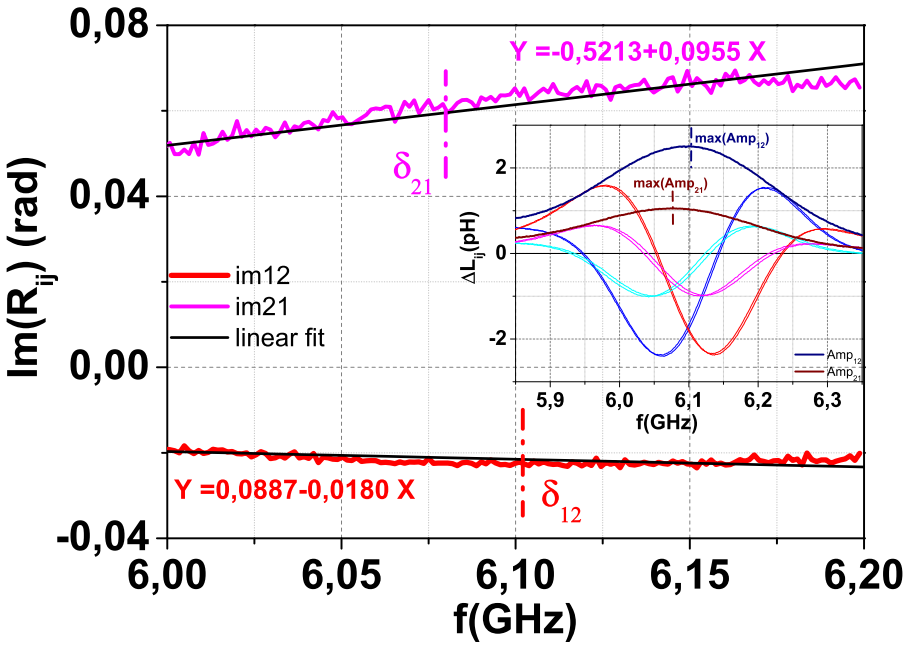

Figure 5.10: The inset shows the frequency position of the maximum of the amplitude of the ΔL_{ij} spectra. The main panel shows that the corresponding frequency shift δ_{ij} are extracted from the imaginary parts of the R_{ij} signals (same condition as figure-5.10).

Once the δ_{ij} are determined one can extract the Doppler shift and Oersted field contributions as follows:

$$\begin{aligned} f_{dop} &= (\delta_{21} - \delta_{12})/2, \\ f_{Oe} &= (\delta_{21} + \delta_{12})/2 \end{aligned} \tag{5.8}$$

5.3 Spin polarization in permalloy thin films

The major idea of this research work is to study the spin dependent surface scattering and to specify its contribution to the spin dependent resistivities of the conduction electrons in an itinerant ferromagnet such as the permalloy thin films. This study requires essentially the determination of the spin polarization for a series of thin films with different thicknesses. This section is dedicated to explain how we extract the spin polarization from the measured Doppler shift

frequency and to present the results of the degree of the spin polarization of the electrical current for a series of permalloy thin films.

5.3.1 The variation of the frequency shift with the DC current

As explained earlier in (§2.4.3) the current induced spin wave Doppler shift is a direct consequence of the adiabatic spin transfer torque exerted by the current. The corresponding expression of this frequency shift is:

$$\frac{\delta f_{dop}}{k} = \frac{\mu_0 \mu_B}{2e\pi} \frac{P}{\mu_0 M_s t} \frac{I}{w} \tag{5.9}$$

where $\frac{\mu_0 \mu_B}{e\pi}$ is a constant equal to 23×10^{-12} $m^3.T.A^{-1}.s^{-1}$, M_s is the saturation magnetization, δf_{dop} is the current induced Doppler shift frequency, k is the wave vector of the spin wave w and t are the width and the thickness of the ferromagnetic metal strip. Now, following the variation of the Doppler shift as a function of the dc current will provide us with the degree of the spin polarization (P).

We carry out the CISWDS measurements for several current values and at

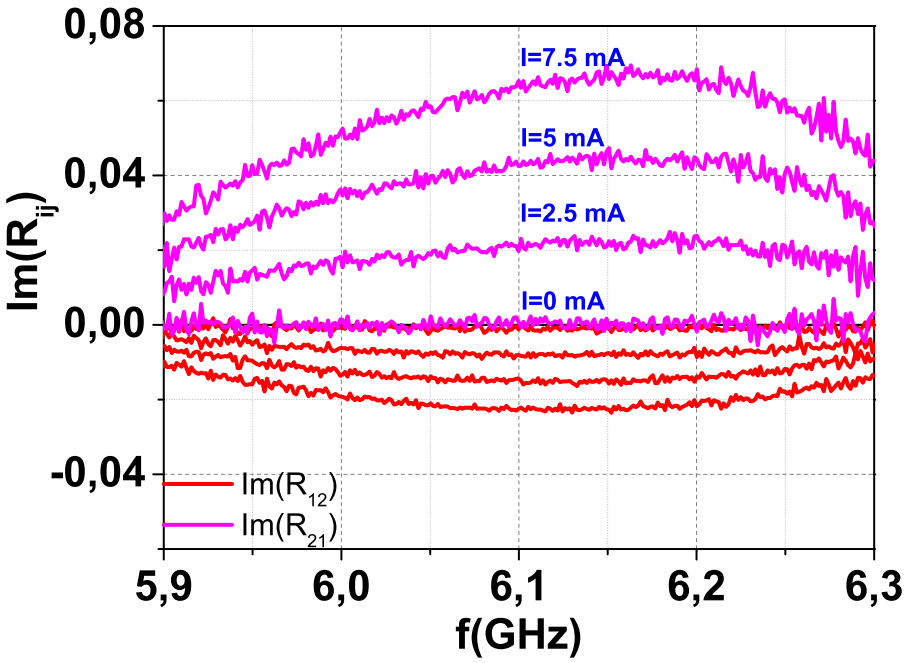

Figure 5.11: The variation of the imaginary part of the R_{ij} signals with the applied current. The measurements are done for a device of 10 nm thickness and a width of 8 μm under a applied field H=28 mT.

different applied magnetic fields. Normally we perform four measurements for the CISWDS at a low field ($\pm$ H_1) and at a high field ($\pm$ H_2) values. We follow the extraction procedure which is mentioned in the section 5.2.4 to deduce the

absolute current induced spin wave Doppler shift frequency, that is only related to the spin polarization of the electrical current.
As an example, the imaginary parts of the R_{ij} signals for different values of the current are shown in the figure-5.11 for a field of 28 mT. As expected at a zero dc current $Im(R_{ij})$ is zero for the two directions. As we increase the dc current $Im(R_{21})$ increases in the positive direction and $Im(R_{12})$ increases in the negative sense. One can extract the Doppler and the Oersted field contributions using the equation-5.8 already mentioned in the section-(5.2.4).
Before showing the results of the Doppler shift, we will briefly describe the frequency shift contribution arising from the Oersted field effect. The frequency shift due to the Oersted field as a function of the dc current is shown in the figure-5.12 for a positive and negative magnetic field. One can notice that the

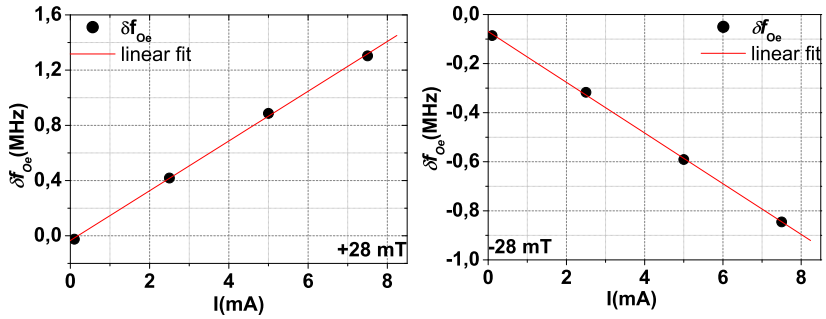

Figure 5.12: The Oersted field contribution to the frequency shift as a function of the dc current for $\pm H$.

slope of the Oersted field frequency shift is positive for a positive field (+H) and negative for a negative field (-H). The change of sign is expected from the symmetry analysis discussed in 5.2.3. This observation is the signature of the Oersted field effect.

Let us now focus on the current induced spin wave Doppler shift. Figure-5.13 shows the current dependence of the Doppler shift extracted from the $Im(R_{ij})$ using the method described in §5.2.4. As expected the frequency shift varies linearly with the DC current. The slope of the line will be used to extract the degree of spin polarization using equation-(5.9).

To extract the degree of the spin polarization the parameters entering equation-5.9 are needed, mainly the width and the thickness of the stripe and the saturation magnetization of each device. The width of the ferromagnetic stripe is determined precisely from the SEM images for each device, and the product $\mu_0 M_s t$ is deduced from the SQUID measurements. The measurements condition and the stability of the experiments allow us to measure precisely the δ_{ij} with an error less than 2%. The larger uncertainty we have is over the product of $\mu_0 M_s t$.

In figure-5.13 an example of the experimental data is shown for two devices of (w= 8μm- t= 10 nm) and (w= 2μm- t=10 nm) the data was taken both

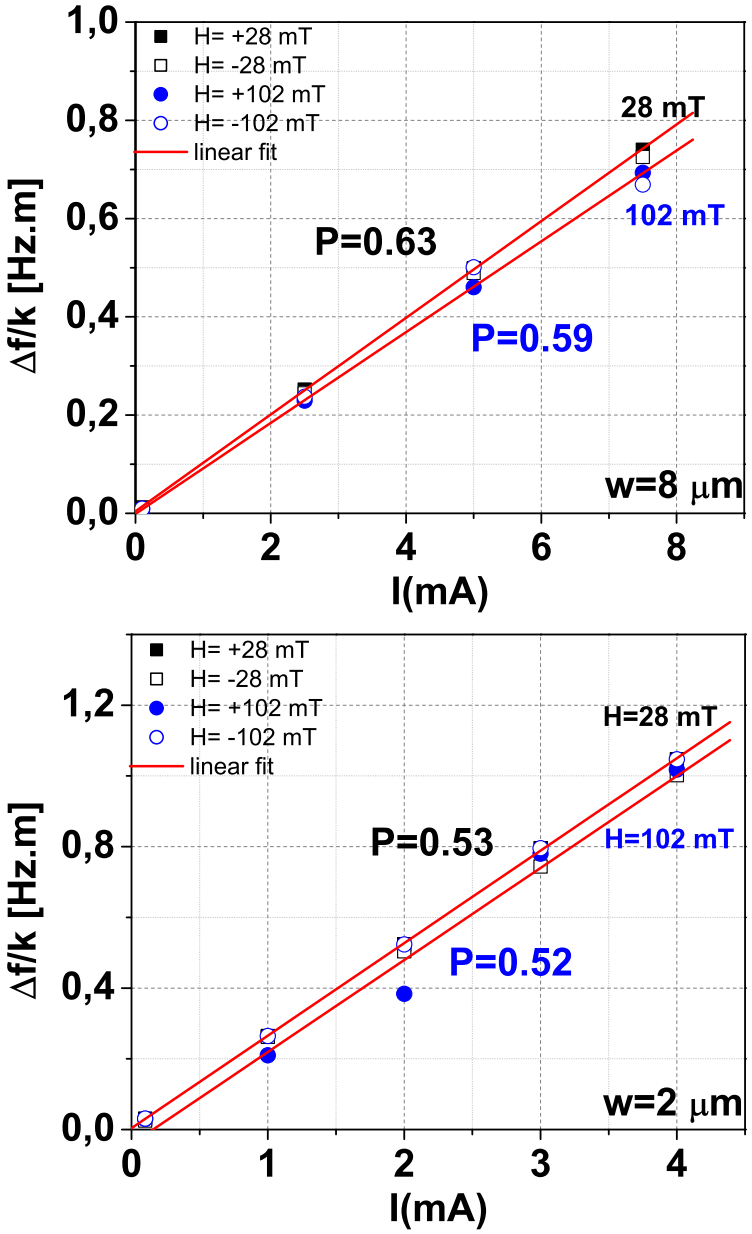

Figure 5.13: The variation of the $\frac{\Delta f}{k}$ as a function of the dc current for the devices (w=8 μm-t= 10nm) and (w=2 μm-t= 10nm) at $\pm$ 28 mT and $\pm$ 102 mT.

for a low and a high field as noted on the graphs. We measure different values of the polarization for the low field and for the high field (P=0.63 and P=0.59 respectively for the 8 μm device with k=3.86 μm^{-1}). This slight difference in the values of the measured polarization between a high and a low field value is systematically observed for different devices. The polarization is always higher for the lower field values. This could be due to inhomogeneity across the cross section of the strip (width/ thickness): as the field is modified the transverse profile of the spin-wave could be modified, resulting in a change of the coupling of the spin wave to the spin current. In the next section 5.3.2 we will use the low field values of the polarization which are easier to measure and more reproducible. Indeed one could notice on figure-5.13 that the measured value of the polarization at positive and negative low field are almost equal, which is a strong indication of the reproducibility of the measurements.
Surprisingly, as the wavevector increases to 7.8 μm^{-1}, the polarization decreases to (P= 0.53) as one notices for the 2 μm stripe. This difference in the polarization value is larger than the error bar expected from the measurements, which indicates that the degree of the spin polarization depends also on the wavevector. It might also be explained by the presence of the magnetic inhomogeneity, because the transverse profile of the spin wave might also depend on the wavevector.

5.3.2 Thickness dependence of the degree of the spin polarization

We carry out the current induced spin wave Doppler shift measurement for the devices of different thicknesses. For each device, the measurements of the degree of the spin polarization are performed with the same procedure and the same analysis as mentioned in the paragraph-5.3.1. A summary of the results is given in the table-5.2. Several comments can be made on the results:

Device	k μm^{-1}	40 nm	20 nm	14 nm	10 nm	6 nm
8 μm	3.86	0.48	0.71	X	0.63	0.46
8 μm	1.55	X	X	X	X	X
3 μm down	3.87	0.45	X	X	0.63	X
3 μm down	1.4	0.79	X	X	0.75	X
3 μm up	7.8	-0.25	X	0.62	X	X
3 μm up	3.14	0.57	X	X	X	X
2 μm	7.84	X	0.59	X	0.53	X
2 μm	2.8	X	X	X	0.58	X

Table 5.2: The measured values of the polarization for different samples. The measurements were done at $\mu_0 H_0$ =28 mT. The second line for each device refers to the measurements performed on the secondary peak of the spin-wave spectra.

- **Reproducibility / stripe width dependence**
  Comparing two devices having same thickness and same k, we find very similar values (0.63 for 8 μm- 10nm vs 0.63 for 3 μm-10 nm, 0.48 for 8 μm- 40 nm vs 0.45 for 3 μm-40 nm). Apparently, the measurement is reproducible and there is no dependence of the effect on the stripe width.

- **Primary vs secondary wavevectors**
  The measurement of the polarization for the same device done at the wavevector of the primary and the secondary peaks show that the measured polarization is slightly higher for the secondary peak such as the results of the measurement of the devices (3 μm down and 2 μm) of the 10 nm. This difference is explained due to an uncertainty over the wavevector of the secondary peaks. On the Fourier transformation displayed on figure 4.3 it is apparent that the secondary peak is broad and it has a lower amplitude, so that a small contribution from other excitations with a different wavevector could shift the effective wavevector of the secondary peaks toward a higher values.

- **High vs Low k**
  As we already pointed in the section 5.3.1, the polarization of the devices with a different wavevector of the primary peaks as the devices 8 μm and 3 μm down of the 10 nm film are different. In the following, to study the thickness dependence of the polarization, we have chosen to compare the

polarization of the devices having the same wavevector (k=3.86 μm^{-1}).

- **40 nm film**
  One could also remark that very different values of the spin polarization are measured for the 40 nm film devices. The polarization takes very different values from device to device and changes even sign for one measurement (3 μm up, main peak). The peculiarity of these measurements are discussed in the next section 5.3.3. They are related to the interplay between the Oersted field and the localization non-reciprocity of the MSSW which results in an apparent Doppler effect in the thick film limit. This is currently under investigation in collaboration with M. Kostylev (UWA). Then one could forget the results of the 40 nm for the moment in the discussion of the spin polarization versus the thickness of the film.

The variation of the degree of the spin polarization as a function of the inverse of the thickness is displayed in the figure-5.14. The values of the polarization are obtained for the devices of a wavevector k= 3.86 μm^{-1}. The degree of the spin polarization decreases from 0.71 for the 20 nm film to 0.46 for the 6 nm film. The strong reduction of the spin polarization with the film thickness which is observed indicates there is an influence of the surfaces on the spin polarized flow. It seems that the surfaces contribute to an additional scattering of the spin polarized current which depolarizes the current.
One could notice a similar trend of the polarization with the thickness on the result of V. Vlaminck [110] although our measurements indicate higher value of the spin polarization. He measured a polarization of the permalloy thin film of 0.43 and 0.51 for the 10 and 20 nm thin films respectively using the current induced spin wave Doppler shift in the MSFVW configuration.
Other studies measured the degree of the spin polarization in permalloy films using the CISWDS in the MSSW configuration: Zhu et al. [118] have measured P= 0.75 at low temperature and P= 0.58 at room temperature for a 20 nm film. Sekiguchi et al.[92] measured P=0.6 for a 35 nm thin film. Thomas et al. [106] have measured P= 0.71 for a 30 nm film. The difference between the measured values in this study and the values found in the literature could be attributed to a difference in the quality of the films and in the extraction of the current induced spin wave Doppler shift.
By extrapolating the result to the bulk, we obtain a degree of spin polarization of 0.80. The deviation of the bulk resistivity of the binary and ternary alloys from the Mathiessen rule suggests the asymmetry coefficient $\alpha = \frac{\rho_\downarrow}{\rho_\uparrow}$ is between 10 and 20 for the iron impurities in a bulk Ni which indicates a polarization $P = \frac{\alpha-1}{\alpha+1}$ between 0.8-0.9 [19]. A value $P = 0.65 \pm 0.1$ was extracted from CPP-GMR measurements [47] [102]. These values are comparable to the value we deduce from the extrapolation.

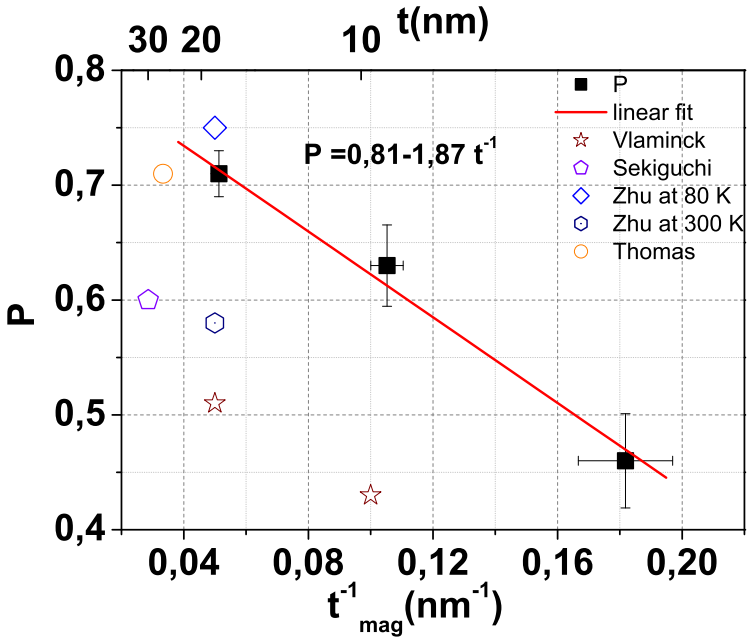

Figure 5.14: The variation of the polarization as a function of the thickness for the measured devices having k=3.86 μm^{-1} (black squares). The open symbols are obtained from other studies as indicated in the text.

5.3.3 Problem of the 40 nm thin film

In section §5.2.3, we have seen that an asymmetry across the film might lead to a current-induced frequency shift associated with the Oersted field. Another source of asymmetry across the film thickness is the magnetization profile of the spin wave itself, which is more localized on the top or bottom surfaces depending on the sign of k and M (see 1.3.4.2). This might couple to the Oersted field to generate a current induced frequency shift. This shift is expected to have the same symmetry as the Doppler shift, which makes it impossible to differentiate between the two contributions from the experiments. To account for this effect, a simulation was performed by M. Kostylev (UWA).
The simulations calculate the magnetization profile and the eigenfrequency of the magnetostatic surface wave in the presence of the DC current. The results support the contribution of such an effect to the measured frequency shift. The effect is calculated to be negligible for thinner films (20 and 10 nm). On the other hand its value becomes critical for the devices of the 40 nm film. M. Kostylev has calculated a frequency shift about 9 MHz for the 40 nm device with w=3.75 μm^{-1} and $k = 7.8\mu m^{-1}$ under an applied field of 28 mT and a DC current of 10 mA. The frequency shift has a sign opposite to the expected Doppler shift. By combining this simulated value with the measured frequency shift one can estimate the degree of the spin polarization for the 40 nm film to be about 0.8. This effect is explained due to interplay between the Oersted field and the localization of the MSSW profile. Importantly, when the exchange interaction is considered the fundamental mode is localized at the surface opposite to the

surface of localization of the magnetostatic surface wave in the pure dipolar regime [61].

5.4 Spin polarized transport in Permalloy thin films

This section is devoted to the interpretation of the thickness dependence of the polarization within the two current model.

5.4.1 The two current model

In the frame of the two current model in its basic form (without spin flip), the spin dependent resistivities can be extracted for the total resistivity (ρ) and to the degree of the spin polarization P. The spin-up $\rho_\uparrow$ and the spin-down $\rho_\downarrow$ resistivities are written as [Equ. 2.1-2.2]:

$$\begin{aligned} \rho_\uparrow &= \frac{2\rho}{1+P}, \\ \rho_\downarrow &= \frac{2\rho}{1-P}. \end{aligned} \tag{5.10}$$

During the measurements of the polarization for each film thickness P(t),simultaneous

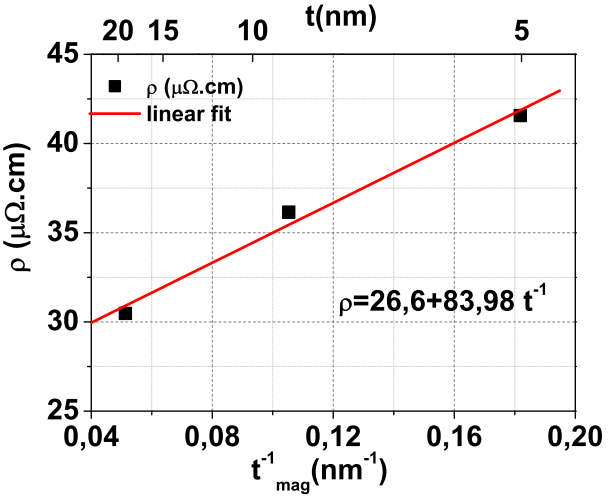

Figure 5.15: The variation of the resistivity as a function of the thickness for the some of devices having k=3.86 μm^{-1}.

four point measurements for the resistivity of the film were done. The results $\rho(t)$ are shown in the figure-5.15. The measured resistivity increases as the film decreases as already noted in section 3.3. The values of the $\rho_\uparrow$ and $\rho_\downarrow$ calculated for each film thickness using equation 5.10 and the data of figures 5.14 and 5.15 are shown in the figure-5.16.

The resistivity of the spin-up channel increases as the film thickness decreases, whereas the resistivity of the spin-down channel decreases with the thickness. The variation of the resistivity of the spin-up channel is consistent

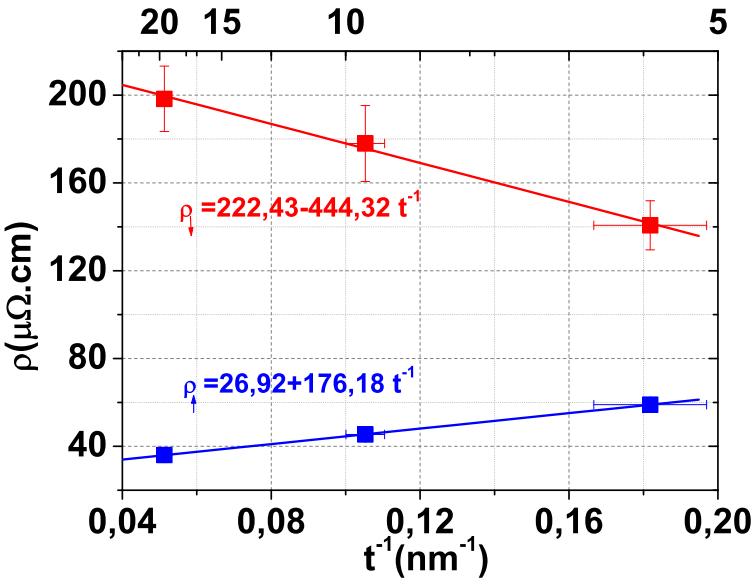

Figure 5.16: The variation of the spin dependent resistivities for the majority and the minority electrons as a function of the inverse of the thickness.

with the Fuchs-Sondheimer description of the surface electron scattering. However, the behavior of the spin-down channel appears unphysical. Consequently, one may suspect the basic two current model is oversimplified as already mentioned in section 2.1, and one should account for spin flip scattering events in the two current model as discussed in the following section.

5.4.2 The two current model with spin flip scattering

If spin flip scattering mechanisms are considered to be active in the permalloy thin films, the simple two current model is not valid any more. In the presence of the spin flip scattering the total resistivity and the degree of the polarization can be calculated by solving the Boltzmann equation in the relaxation time approximation [36]. The results of P and ρ are written as:

$$\begin{aligned} \rho &= \frac{\rho_\uparrow\rho_\downarrow+\rho_{\uparrow\downarrow}(\rho_\uparrow+\rho\downarrow)}{\rho_\uparrow+\rho\downarrow+4\rho_{\uparrow\downarrow}} \\ P &= \frac{(\rho_\downarrow-\rho_\uparrow)}{\rho_\uparrow+\rho\downarrow+4\rho_{\uparrow\downarrow}} \end{aligned} \tag{5.11}$$

where $\rho_\uparrow$ and $\rho_\downarrow$ are the spin dependent resistivity and $\rho_{\uparrow\downarrow}$ is the spin flip effective resistivity. To account for a probable surface scattering contribution, we

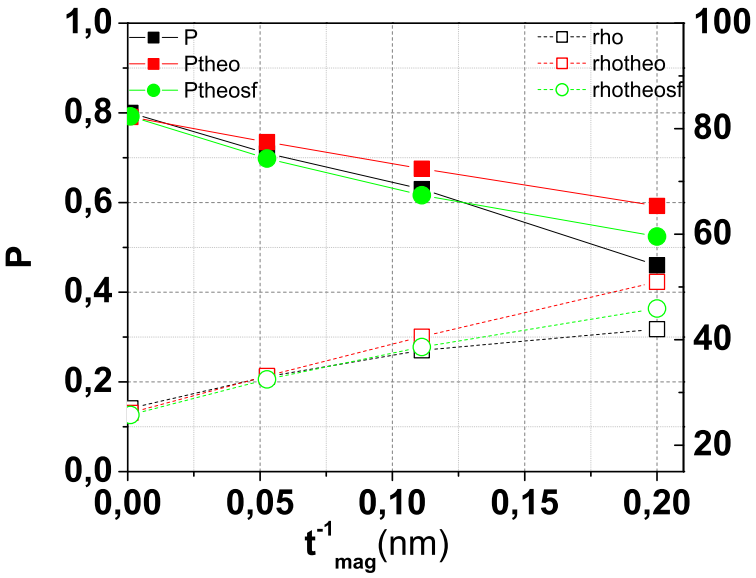

Figure 5.17: The spin polarization (left axis) and the resistivity (right axis) as a function of the film thickness obtained from of the experimental results, and the theoretical values from the two current model with and without spin-flip scattering.

assume that the three spin dependent resistivities ($\rho_\uparrow$, $\rho_\downarrow$, $\rho_{\uparrow\downarrow}$) have a thickness dependence behavior of the form $\rho_i = A_i + B_i/t$. We adjust the parameters of each resistivity channel A_i and B_i to reproduce the measured ρ and P using the equations-5.11. After many trials the most convenient parameters are noted in the table-5.3.
The black symbol on figure-5.17 show the measured values of P and ρ (including an extrapolate to infinite thickness). The red symbol show the best fit for P and ρ in the absence of the spin-flip scattering. And the green symbols show the best fit for P and ρ accounting for spin-flip scattering. With this set of parameters one could notice the impact of the spin-flip scattering. It is obvious that the results from the two current model without spin flip is far from the experimental

resistivity	A_i	B_i
$\rho_{\uparrow}$	25	25
$\rho_{\downarrow}$	200	50
$\rho_{\uparrow\downarrow}$	4	200

Table 5.3: The best fit of the A_i and B_i parameters of the 3 scattering resistivities.

data, however when the spin flip scattering is included it approaches better the measurements. Figure-5.18 displays the spin dependent resistivities from the two current model including spin-flip scattering.

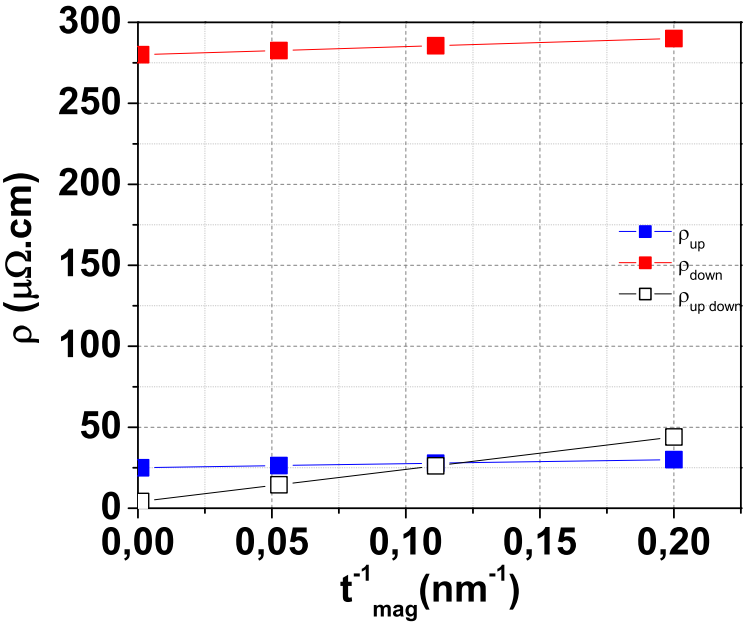

Figure 5.18: The spin dependent resistivity obtained from the two current model including spin-flip scattering.

We could justify the thickness dependence of the spin-flip scattering due to one of the following possible mechanisms. First, since the measurements are performed at room temperature, one expects spin-flip scattering due to the collision of the electrons with thermal magnons as was indicated in the analysis of the temperature dependence of the spin dependent resistivity [118]. This contribution to the spin-flip resistivity might be enhanced at small thickness, for example if surface thermal magnons are present. Second, one could expect an enhanced spin orbit coupling of the atoms located near to the interfaces, which will lead to an enhanced mixing between the two spin population.Third, the spin flip scattering could be due to the presence of magnetic impurities close to the interfaces (for example the impurities responsible of the slow relaxers behavior discussed in chapter 3).

Conclusion

The film thickness dependence of the current induced spin wave Doppler shift was measured in order to study the effect of surface electron scattering on the spin polarized transport. Combining propagating spin wave spectroscopy signals taken for different polarities of H, k and I, we could separate the Doppler contribution from other current induced effects. Our results show that the surfaces depolarize the electrical current. The extrapolated bulk value of the spin polarization (0.8) is found to be comparable to the values deduced from the residual resistivity of bulk alloys [19] and from CPP-GMR [47] [102]. The strong decrease of the spin-polarization measured at small thickness could be explained by surface induced spin-flip scattering.

Conclusion

The main aim of this thesis was to study the effects of the surfaces on the spin dependent transport. The technique of the current induced spin wave Doppler shift was used to measure the degree of spin-polarization of the electrical current. In order to extract the contribution of surface electron scattering, the degree of spin-polarization was measured for different film thicknesses.

To carry out this study a precise knowledge of the film characteristics is required. Accordingly, standard characterization techniques have been used to investigate the magnetic and electrical properties of the permalloy thin films as described in the third chapter. The main result of this study is the following:

- A 1/t dependence law was measured both for the resistivity, the effective magnetization and the damping coefficient. This dependence was attributed to the influence of the surfaces (surface electron scattering, surface anisotropy, and surface relaxation processes respectively).

At the end of this step, we had a better knowledge of the characteristics of our films.
In a second step, propagating spin wave spectroscopy measurements have been performed in the absence of the electrical current. The spin waves have been measured in the magnetostatic surface wave configuration (MSSW). The characteristics of this wave are quite special and one has to identify them carefully to be able to extract the Doppler frequency shift accurately enough in the presence of the DC current. This work is presented in the fourth chapter. Its main results are:

- The reflection signals have been used to extract the magnetic properties of the film which are found to be in good agreement with those deduced from standard FMR measurements.

- A qualitative understanding of the transmission signals (amplitude and phase) is provided.

- The peculiarities of the magnetostatic surface waves were investigated. The non-reciprocity in amplitude and in frequency of these waves were discussed.

At this point, we were ready to perform an accurate film thickness dependence study using the current induced spin wave Doppler shift experiment. The results of this study are presented in the fifth chapter:

- The current induced frequency shifts observed in the magnetostatic surface wave configuration were described and interpreted, which allows one to extract accurately the Doppler shift.
- The spin polarization extracted from the CISWDS was found to decrease strongly as the film thickness decreases. This observation is the main finding of this study.
- These results were discussed in the context of the two current model. It was necessary to include a spin-flip effective resistivity with a sizeable surface contribution to account for the measurements.

This work addressed the question of the variation of the degree of spin polarization of the electrical current as a function of the thickness. It is therefore of direct interest for a fundamental understanding of the effects of surfaces on the spin polarized transport. In addition the results of this study might be useful for technological developments. First, some spin transfer devices, such as racetrack memories, rely on spin current flowing along very thin nanowires [86]. To optimize these devices, it is necessary to understand the degree of the spin polarization of the electrical current (P), the non-adiabatic spin transfer torque coefficient (β) and the magnetization relaxation parameter described by the Gilbert damping coefficient (α). Our study shows the importance of the size effect (surface electron scattering) for P and α. Propagating spin wave spectroscopy under DC current might also be used to extract the information on β [92]. Second, the study of the propagating characteristics of the spin wave is crucial for the development of logical circuits using spin waves as described by [45], [58], and in magnonic crystal on the nanoscale [83]. Our study shows how surface effects influence these propagation characteristics. It also shows the strengths and the limitation of the PSWS technique in the form used up to now.

Perspectives

During this study many fundamental and experimental questions arose which should be addressed in future works. Among the challenges to address, one can mention:

- The extraction of the propagation characteristics of the spin waves from the propagating spin wave spectroscopy signals could be made quantitative.
- The origin of the frequency non reciprocity in our magnetostatic surface wave measurement could be further studied.
- In this work, we assume the magnetic film is a homogeneous single layer model. However, we have some indications of inhomogeneities over the thickness (preliminary neutron measurements). The system would probably be better described as a composite film. Although the single layer model probably capture most of the thickness dependance, both experimental and theoretical investigations would be required to understand the spin polarized transport and the propagation of the spin waves in such composite films.
- The measurements of the degree of the spin polarization could be extended also to low temperature, in order to extract the phonon contribution.
- Measuring precisely the current induced changes in the amplitude of the signals should allow one to extract the non adiabatic spin transfer torque.

Appendix A

Magnetostatic surface waves in the presence of an out of plane uniaxial anisotropy

To account for the effect of a uniaxial out of plane anisotropy on the dispersion relation of the magnetostatic surface wave, we have adapted the formalism described in section 1.3.4. Consider the direction of the uniaxial anisotropy (K_u) to be along the film thickness (y-axis). The dynamical component of the anisotropy field is written as:

$$h_{ku} = \frac{2K_u m_y(t)}{\mu_0 M_s^2}\hat{e}_y. \tag{A.1}$$

In the presence of the uniaxial anisotropy, the Polder susceptibility tensor is written as:

$$\chi = \frac{\omega_M}{D}\begin{pmatrix} \omega_0 - \omega_k & -i\omega \\ i\omega & \omega_0 \end{pmatrix} \tag{A.2}$$

where $\omega_k = \gamma\frac{2K_u}{\mu_0 M_s^2}$. D is defined as:

$$D = \frac{[(\omega_0)(\omega_0 - \omega_k) - \omega^2]}{\omega_M}$$

Notice that the diagonal components of the susceptibility tensor are not equal. Consequently, the permeability tensor equation writes:

$$\bar{\mu} = \mu_0(\bar{I} + \chi) = \mu_0\begin{pmatrix} 1+\chi_{xx} & -\frac{i\omega}{D} & 0 \\ \frac{i\omega}{D} & 1+\chi_{yy} & 0 \\ 0 & 0 & 1 \end{pmatrix} \tag{A.3}$$

Now, solving the equation (1.28) of the scalar potential in the magnetic layer by writing the trial solution as:

$$\Psi_{II} = e^{i\nu k_x x}[\Psi_{0+}e^{k_y y} + \Psi_{0-}e^{-k_y y}],$$

One obtains k_x and k_y as:

$$\begin{array}{ccc} k_y^2 & = & -(\frac{1+\chi_{xx}}{1+\chi_{yy}})k_x^2 \\ k_y & = & i\alpha k_x \\ \text{where} & & \\ \alpha & = & \sqrt{(\frac{1+\chi_{xx}}{1+\chi_{yy}})} \end{array} \tag{A.4}$$

The scalar potential has a propagation characteristic across the x-axis, and it is decaying exponential along the film thickness. In contrary to the section 1.3.4.2, k_x and k_y have a different magnitude. The scalar potential in the magnetic film is written as:

$$\Psi = e^{ikx}[\Psi_{0+}e^{\alpha ky} + \Psi_{0-}e^{-\alpha ky}]. \tag{A.5}$$

Applying the boundary condition between the dielectric and the magnetic layer, and solving the system of equation for Ψ_{0+} and Ψ_{0-} we derive an implicit formula for dispersion relation written as:

$$e^{2\alpha kd} = \frac{[\omega + \sqrt{(D+\omega_0-\omega_k)(D+\omega_0)} - D][-\omega + \sqrt{(D+\omega_0-\omega_k)(D+\omega_0)} - D]}{[\omega - \sqrt{(D+\omega_0-\omega_k)(D+\omega_0)} - D][-\omega - \sqrt{(D+\omega_0-\omega_k)(D+\omega_0)} - D]}, \tag{A.6}$$

Performing an expansion of the implicit equation-A.6 to the second order in (kd) we obtain a simpler analytical formula for the dispersion relation:

$$\omega = \sqrt{[\omega_0(\omega_0-\omega_k) + \omega_0\omega_M + \frac{1}{2}\omega_M^2(kd-(kd)^2) - \frac{1}{2}\omega_k\omega_M(kd+(kd)^2)]} \tag{A.7}$$

Another approximate formula is obtained by replacing the saturation magnetization M_s by the effective magnetization M_{eff} and M_s^2 by M_sM_{eff} in formula 1.47:

$$\omega^2 = (\gamma\mu_0)^2(H_0(H_0+M_{eff}) + M_sM_{eff}(\frac{1-e^{-2kd}}{4})) \tag{A.8}$$

Figure-A.1 shows a comparison between the exact solution of equation A.6 (black curve), the analytical equation A.7 (red curve), and the equation A.8 (blue curve). The three formulas are in agreement for low wavevector k. Formula A.8 appears to be a very good approximation of the exact solution also at higher wave-vectors.

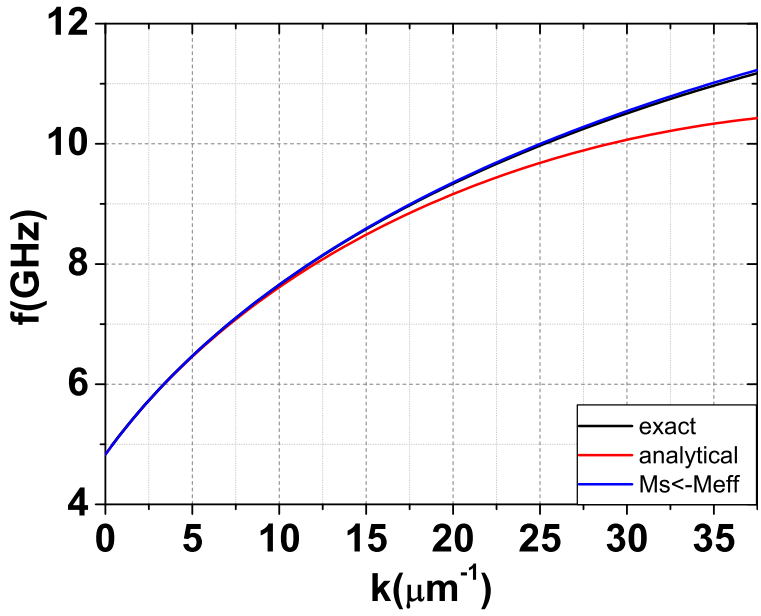

Figure A.1: Plot of the dipersion relations for the exact and the analytical equtions mentioned above. The parameters are t =10 nm, and $\mu_0 H_0$=30 mT, $\mu_0 M_s$=0.9 T, $\mu_0 H_k$=50 mT and $\gamma/2\pi$ =29.2 GHz/T.

Appendix B

Propagating spin wave spectroscopy parameters for reflection and transmission signals

This appendix gives in tabular form all the parameters extracted from the analysis of the propagating spin wave spectroscopy signals.

B.1 Reflection signals: A, B, C parameters

Device	k μm^{-1}	40 nm	20 nm	14 nm	10 nm	6 nm
7 μm	3.86	27.4 ± 1.8	29.9 ± 0.59	X	30.2 ± 1.39	30.4 ± 4.2
3 μm down	3.87	29.5 ± 4.6	X	X	32.45 ± 2.42	X
3 μm up	7.8	28.7 ± 7.2	X	27.5 ± 1.5	X	X
2 μm	7.84	X	29.25 ± 1.2	X	32.3 ± 2.6	X

Table B.1: A summary of the gyromagnetic ratio $\frac{\gamma}{2\pi}$ (in GHz/T) of all measured devices extracted from the reflection signals of the propagating spin wave spectroscopy (PSWS) experiment. As we have seen in the 4.2.3 the gyromagnetic $\frac{\gamma}{2\pi}$ is obtained from the correspondence of the quadratic term from the fit and the quadratic term of the dispersion relation of the magnetostatic surface wave.

Device	k μm^{-1}	40 nm	20 nm	14 nm	10 nm	6 nm
7 μm	3.86	869.2 ± 9.9	837 ± 4.8	X	803.4 ± 9.3	767 ± 26.06
3 μmdown	3.87	820.7 ± 29.6	X	X	748.1 ± 14.07	X
3 μmup	7.8	843.4 ± 43	X	844.8 ± 7.9	X	X
2 μm	7.84	X	845.8 ± 9.2	X	753.02 ± 15.5	X

Table B.2: The $(\frac{\gamma}{2\pi})^2 M_{eff}$ (in GHz^2/T) values of all the measured devices extracted from the reflection signals parameters of the propagating spin wave spectroscopy experiment. As we have seen in the 4.2.3 $(\frac{\gamma}{2\pi})^2 M_{eff}$ is obtained from the correspondence of the linear term (B) from the fit and the linear term of the expected dispersion relation of the magnetostatic surface wave.

Device	k μm^{-1}	40 nm	20 nm	14 nm	10 nm	6 nm
7 μm	3.86	53.5 ± 0.33	28.02 ± 0.22	X	13.8 ± 0.32	7.68 ± 0.78
3μmdown	3.87	50.8 ± 1.2	X	X	13.04 ± 0.39	X
3 μmup	7.8	90 ± 1.75	X	36.1 ± 0.25	X	X
2μm	7.84	X	47.2 ± 0.42	X	26.8 ± 0.4	X

Table B.3: The obtained values of the zero field frequency parameter (in GHz^2) for the measured devices by the propagating spin wave spectroscopy. These values are the constant terms (C) of the fits of the square of the resonance frequency as a function of the applied field.

B.2 Transmission signals: group velocity and the attenuation length

The group velocity

In the table-B.4 and in the table-B.5 we note the measured and the theoretical value for the 3 devices of the 10 nm and the 40 nm films respectively. The propagating spin waves in the 8 μm and in the 3 μm devices for the 10

Sample	8 μm	3 μm-down	2 μm
$\mu_0 H_{ext}[mT]$	28	28	28
D [μm]	8.8	14.5	7.7
$\delta f_{\phi=\frac{\pi}{2}}[MHz]$	79 ± 1.8	70± 1.4	79 ± 1.8
$v_g)_{measure}[m.s^{-1}]$	2780.8 ± 63.36	4060 ± 81.2	2433.2 ± 55.4
f [GHz]	6.12	5.95	7.01
k [μm^{-1}]	3.86	3.87	7.84
$v_g)_{theo}[m.s^{-1}]$	1970.7	2027.03	1720.5

Table B.4: The measured and the calculated values of the group velocity for the 10 nm film of different devices. The theoretical group velocity were obtained from the formula 4.12 with the parameter ($\mu_0 M_s = 0.96T, \frac{\gamma}{2\pi} = 30GHz/T$). The measured values were obtained from the main peak of the antennas.

Sample	8 μm	3 μm-down	3 μm-up
$\mu_0 H_{ext}[mT]$	28	28	28
D [μm]	8.8	14.5	5.5
$\delta f_{\phi=\frac{\pi}{2}}[MHz]$	130 ± 1.04	100.5±1.2	150 ± 2.25
$v_g)_{measure}[m.s^{-1}]$	4576 ± 36.6	5829 ±69.6	3300 ± 49.5
f [GHz]	8.917	8.637	10.81
k [μm^{-1}]	3.86	3.87	7.8
$v_g)_{theo}[m.s^{-1}]$	4291.7	4427.3	2583.1

Table B.5: The measured and the calculated values of the group velocity for different devices of the 40 nm film. The theoretical group velocity were obtained from the formula 4.12 with the parameter ($\mu_0 M_s = 0.96T$, $\frac{\gamma}{2\pi} = 30GHz/T$). The measured values were obtained from the main peak of the excitation.

nm and the 40 nm film theoretically have the same propagation characteristics. Experimentally, they are excited with the same antenna and they are oscillating at the same frequency. However, we measure different group velocity for these devices.

In table-B.6, we compare the group velocity measured at the same frequency in the 10 and the 40 nm films. Theoretically, we expect the group velocity to be 3 times faster in the 40 nm than in the 10 nm films. We measure the group velocity in the 40 nm higher than that of the 10 nm by a factor of 2. This indicates that the spin wave propagating in the 40 nm are propagating over a larger distance compared to the 10 nm. This is mainly due to the larger amplitude of the signal in the 40 nm film and the smaller damping compared with the 10 nm film.

Sample	40nm 8 μm	40nm 3 μm-down	10 nm 8 μm-down	10 nm 3 μm-down
$\mu_0 H_{ext}[mT]$	28	28	60	80
D [μm]	8.8	14.5	8.8	14.5
$\delta f_{\phi=\frac{\pi}{2}}[MHz]$	130 ± 1.04	100.5±1.2	68 ± 1.5	60 ±1.2
$v_g)_{measure}[m.s^{-1}]$	4576 ± 36.6	5829 ±69.6	2396.6 ±52.8	3480 ± 69.6
f [GHz]	8.917	8.637	8.673	9.02
k [μm^{-1}]	3.86	3.87	3.86	3.87
$v_g)_{theo}[m.s^{-1}]$	4291.7	4427.3	1390.6	1336.8

Table B.6: A comparison of the group velocity for spin waves oscillating at similar frequencies in the 10 and 40 nm film devices. The theoretical group velocity were obtained from the formula 4.12 with the parameter ($\mu_0 M_s = 0.96T$, $\frac{\gamma}{2\pi} = 30GHz/T$). The measured vales were obtained from the main peak of the excitation.

Attenuation length

Sample	8 μm			
$\mu_0 H_{ext}[mT]$	28	60	80	160
D [μm]	8.8	8.8	8.8	8.8
$\Delta L_{ii}[pH]$	16.9	15.02	13.7	11.1
$\Delta L_{12}[pH]$	2.46	1.31	0.93	0.26
$\Delta L_{21}[pH]$	1.013	0.43	0.307	0.057
$L_{att})_{mea}[\mu m]$	5.56	4.08	3.66	2.47
f [GHz]	6.127	8.673	9.21	12.815
k [μm^{-1}]	3.86	3.86	3.86	3.86
$v_g)_{theo}[m.s^{-1}]$	1968.4	1390.6	1309.5	941.14
$L_{att})_{theo}[\mu m]$	15.3	10.2	9.2	5.8

Table B.7: The variation of the attenuation length with the applied field for the device of (t= 10 nm, w =8 μm). The theoretical values of the attenuation length were obtained from the formula 4.14 with the parameters ($\mu_0 M_s$=0.96 T, α =0.0084, $\frac{\gamma}{2\pi}$=30 GHz/T). The measured values were obtained for the main peak of the excitation.

In the tables B.8 and B.9 we show the attenuation length for different devices of the 10 and 40 nm films at a given applied field. The similar devices 8 μm and 3 μm down have similar attenuation length of the L_{att} about 5.5 μm in the 10 nm, and about 17.1 μm in the 40 nm film.

Sample	8 μm	3 μmdown	2 μm
$\mu_0 H_{ext}[mT]$	28	28	28
D [μm]	8.8	14.5	7.7
$\Delta L_{ii}[pH]$	16.9	14.9	3.82
$L_{att})_{mea}[\mu m]$	5.55	5.54	3.6
f [GHz]	6.127	5.94	7.015
k [μm^{-1}]	3.86	3.87	7.84
$v_g)_{theo}[m.s^{-1}]$	1968.4	2030	1587.7
$L_{att})_{theo}[\mu m]$	15.3	15.8	12.3

Table B.8: The attenuation length for different devices of the t= 10 nm film. The theoretical values of the attenuation length were obtained from the formula 4.14 with the parameter ($\mu_0 M_s$=0.96 T, α =0.0084, $\frac{\gamma}{2\pi}$=30 GHz/T). The measured values were obtained for the main peak of the excitation.

In the table B.10 we compare the attenuation length for the 10 and 40 nm films for similar devices at similar frequencies. We notice that the attenuation length is longer in the 40 nm ($\sim$ 17 μm) than the 10 nm ($\sim$ 5.5 μm) film.

Sample	8 μm	3 μmdown	3 μm up
$\mu_0 H_{ext}[mT]$	28	28	28
D [μm]	8.8	14.5	5.5
$\Delta L_{ii}[pH]$	18.16	17.92	2.4
$\Delta L_{12}[pH]$	8.48	6.58	0.996
$\Delta L_{21}[pH]$	2.38	2.04	0.19
$L_{att})_{mea}[\mu m]$	17.11	19.8	7.8
f [GHz]	8.891	8.6	10.81
k [μm^{-1}]	3.86	3.87	7.8
$v_g)_{theo}[m.s^{-1}]$	4304.3	4446.4	2583.1
$L_{att})_{theo}[\mu m]$	37.6	38.9	22.5

Table B.9: The attenuation length for different devices of the t=40 nm film. The theoretical values of the attenuation length were obtained from the formula 4.14 with the parameter ($\mu_0 M_s$=0.96 T, α =0.0075, $\frac{\gamma}{2\pi}$=30 GHz/T). The measured values were obtained for the main peak of the excitation.

thickness	40	40	10	10
device	8 μm	3 μmdown	8 μm	3 μm down
$\mu_0 H_{ext}[mT]$	28	28	60	80
D [μm]	8.8	14.5	8.8	14.5
$\Delta L_{ii}[pH]$	18.16	17.92	15.03	11.53
$\Delta L_{12}[pH]$	8.48	6.58	1.32	0.271
$\Delta L_{21}[pH]$	2.38	2.04	0.43	0.14
$L_{att})_{mea}[\mu m]$	17.11	19.8	4.09	4.35
f [GHz]	8.891	8.6	8.673	9.02
k [μm^{-1}]	3.86	3.87	3.86	3.87
$v_g)_{theo}[m.s^{-1}]$	4304.3	4446.4	1390.6	1336.8
$L_{att})_{theo}[\mu m]$	37.6	38.9	10.1	9.4

Table B.10: The attenuation length for different devices of the t=40 nm and t= 10 nm film. The theoretical values of the attenuation length were obtained from the formula 4.14 with the parameters mentioned in the previous tables B.9 and B.8. The measured vales were obtained for the main peak of the excitation.

Appendix C

Rôle des surfaces dans la dynamique d'aimantation et le transport polarisé en spin: une étude d'ondes de spin

Résumé en français

Introduction

L'émergence de l'électronique de spin dans les technologies de stockage des données a ouvert la voie à une nouvelle génération de dispositifs. Bien que le spin de l'électron soit connu depuis longtemps, il n'avait pas été utilisé de façon intensive pour transporter l'information, jusqu'à la découverte de la magnétorésistance géante (GMR pour giant magnetoresistance) en 1988. L'effet de GMR montre l'interdépendance entre le courant électrique et la configuration de l'aimantation dans des empilements de couches ferromagnétiques. L'intérêt de l'industrie pour l'électronique de spin a émergé quand des hétérostructures GMR sont apparues dans les têtes de lecture des disques durs [20].

En parallèle, le phénomène du couple de transfert de spin (STT pour spin transfer torque) a été découvert comme un outil prometteur pour manipuler l'orientation de l'aimantation d'une couche magnétique avec un courant électrique. Le couple de transfert de spin a été observé dans une série d'expériences : renversement d'aimantation induit par un courant[1] [66], oscillation d'aimantation entretenue par transfert de spin [48][107], déplacement de parois de domaine induit par un courant [116] et, plus récemment, décalage Doppler d'ondes de spin induit par un courant [111]. J. Katine de Hitachi et E. Fullerton du centre de recherche sur l'enregistrement magnétique [91] ont déclaré que la nouvelle génération de mémoires magnétiques sera basée sur les dispositifs de transfert de spin dans un avenir proche. Avec cette multiplication très rapide des dispositifs d'électronique de spin,une compréhension fondamentale du transport polarisé en spin est nécessaire.

La physique de base de l'électronique de spin est connue depuis le début du siècle dernier. Sa pierre angulaire est le modèle à deux courants proposé par Mott [79] pour décrire le transport électrique dans les métaux ferromagnétiques (Fe, Co, Ni). Dans ce modèle, on distingue deux populations d'électrons selon que leur moment magnétique de spin est aligné parallèlement (spins majoritaires) ou antiparallèlement (spins minoritaires) à l'aimantation du matériau. Ces deux populations d'électrons forment deux canaux de conduction avec des conductivité différentes.

Différentes sources de diffusion des électrons (phonons, impuretés [19], surfaces, joints de grains [68]) sont susceptibles de contribuer à la résistivité de chacun des deux canaux. Un certain nombre d'études ont été réalisées dans les années 1970 pour évaluer certaines de ces contributions. Ainsi, des mesures de résistivité dans des alliages binaires et ternaires réalisées à différentes températures, ont donné indirectement accès aux résistivités dépendantes du spin associées aux impuretés et aux phonons. A l'échelle du nanomètre on s'attend à ce que les surfaces jouent un rôle déterminant [85]. Jusqu'à présent, l'impact de la diffusion des électrons par les surfaces n'a pas pu être abordé, sauf pour certaines études GMR où la présence de plusieurs couches de métal rend l'interprétation particulièrement compliquée. La principale difficulté est l'absence d'une expérience appropriée pour accéder directement au degré de polarisation en spin qui mesure l'asymétrie entre les courant transportés par les électrons majoritaires et minoritaires.

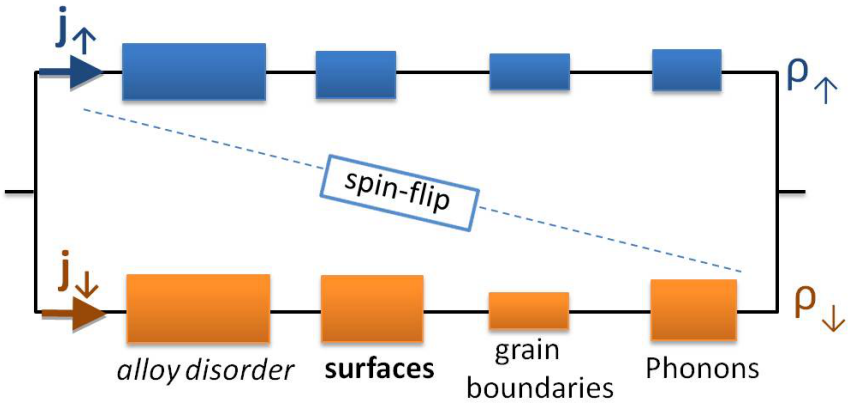

Figure C.1: Un scénario possible pour rendre compte du transport polarisé en spin dans un film mince fait d'un alliage ferromagnétique métallique

Récemment, une nouvelle méthode fondée sur le décalage Doppler d'ondes de spin induit par un courant [111], a été proposée par notre groupe pour mesurer directement le degré de la polarisation en spin du courant électrique dans un film de métal ferromagnétique.

A l'aide de cette nouvelle technique, nous avons décidé de sonder les propriétés de transport polarisé en spin dans des films minces de permalloy ($Ni_{80}Fe_{20}$).

Un modèle de circuit électrique représentant le transport polarisé en spin dans ce type de films est esquissé dans la figure-C.1. Ce scénario est basé sur le modèle à deux courants et il considère que les électrons de chaque canal sont diffusés par plusieurs sources : le désordre d'alliage, les phonons, les surfaces et les joints de grain. Dans ce scénario, des diffusions avec retournement de spin (spin-flip) sont également possibles (influence des magnons thermiques ou de l'interaction spin-orbite). Dans une première étape pour valider/invalider ce scénario, une étude de la dépendance en épaisseur de film du décalage Doppler d'ondes de spin induit par un courant a été effectuée dans le cadre de cette thèse afin de comprendre le rôle des diffusions par les surfaces dans le transport polarisé en spin.

Contenu du manuscrit

Les chapitres 1 et 2 de ce manuscrit présentent les notions de base nécessaires pour comprendre les expériences réalisées.

Dans le premier chapitre, nous présentons les notions de résonance ferromagnétique et d'onde de spin. Nous commençons tout d'abord par écrire l'expression de l'énergie magnétique dans une couche mince ferromagnétique. Nous introduisons ensuite l'équation du mouvement de l'aimantation appelée équation de Landau-Lifschitz. A l'aide de cette dernière, nous obtenons la condition de résonance ferromagnétique pour une couche mince. Cette expression contient des paramètres matériaux importants tels que l'aimantation effective et l'anisotropie de surface. Puis, nous décrivons les propriétés des ondes de spin se propageant dans des couches minces. Les relations de dispersion sont données pour différentes géométries (orientations relatives du vecteur d'onde de propagation, de l'aimantation et de la normale au film). Une attention particulèire est accordée à la configuration d'onde magnétostatique de surface (MSSW pour magnetostatic surface wave) que nous avons utilisée dans les mesures. Ce premier chapitre se termine par une description générale des processus de relaxation de la précession de l'aimantation dans les métaux ferromagnétiques.

Dans le deuxième chapitre, nous introduisons des aspects indispensables à l'analyse des résultats expérimentaux. Tout d'abord, nous décrivons le transport polarisé en spin dans les métaux ferromagnétiques. Après avoir introduit le modéle à deux courants, nous montrons comment il peut être amélioré en introduisant les diffusions avec renversement de spin. La diffusion des électrons par les surfaces est ensuite introduite à partir du modèle de Fuchs-Sondheimer (FS). Finalement, le phénomène de couple de transfert de spin est décrit ainsi que plusieurs de ses manifestations expérimentales, pour des vannes de spin, pour des parois de domaine et enfin pour des ondes de spin (décalage Doppler).

Les chapitres 3, 4, 5 contiennent les résultats experimentaux que nous avons obtenus.

Dans le troisième chapitre, nous décrivons le dépôt et la caractérisation des films minces de permalloy. Plusieurs séries de films de permalloy entourés de deux couches d'Al_2O_3 et/ou de SiO_2 ont été déposés par pulvérisation cathodique. Sur ces films, nous avons effectué une étude de caractérisation struc-

turale, électrique et magnétique. Des images de microscopie électronique à transmission montrent que l'interface entre le permalloy et l'alumine est plate. Des mesures d'aimantation (SQUID) menées en fonction de l'épaisseur montrent une couche magnétiquement morte d'environ 1nm. Ensuite, nous avons utilisé la méthode du Van der Pauw (VdP) pour mesurer la résistivité en fonction de l'épaisseur des films. On constate que la resistivité augmente quand l'épaisseur diminue, ce qui est interprété dans le cadre du modèle de Fuchs-Sondheimer comme une conséquence de la diffusion des électrons par les surfaces. Puis, des mesures de résonance ferromagnetique (FMR pour ferromagnetic resonance) ont été réalisés en utilisant un spectromètre en cavité standard. En suivant l'évolution de la raie de résonance en fonction de l'épaisseur t du film de permalloy, nous avons mesuré une dépendance en $1/t$ pour l'aimantation effective et le coefficient d'amortissement de Gilbert.

Dans le quatrième chapitre, nous présentons une étude expérimentale de la propagation des ondes de spin dans ces films dans la géométrie MSSW. Cette étude est réalisée en utilisant une technique de mesure inductive : l'excitation et la détection des ondes de spin se fait par l'intermédiaire d'une paire d'antennes intégrées au-dessus d'un ruban fabriqué à partir du film ferromagnétique. Tout d'abord, nous décrivons le protocole de nanofabrication utilisé pour fabriquer les rubans, les antennes et les contacts électriques. Ensuite, nous décrivons des mesures d'auto-inductance (obtenues à partir du signal hyperfréquence réfléchi par une antenne) servant à la caractérisation magnétique des rubans. Les caractéristiques obtenues sont en accord avec celles déduites des mesures FMR, ce qui indique que les films ne sont pas altérés par le protocole de nano-fabrication. Nous présentons ensuite des mesures d'inductance mutuelle (obtenues à partir du signal hyperfréquence transmis d'une antenne à l'autre). La forme des signaux observés est interprétée de manière qualitative. Une attention particulière est donnée au phénomène de non-réciprocité, typique de la configuration MSSW : les signaux observés pour des directions de propagation opposés sont différents, à la fois en amplitude et en fréquence.

Une fois que les films étaient caractérisés et que les signaux d'ondes de spin étaient compris, nous avons pu nous intéresser à la modification des signaux d'ondes de spin sous l'effet d'un courant électrique, ce qui est décrit dans le cinquième chapitre. La première conséquence de l'application d'un courant électrique est la génération d'un champ magnétique (le champ d'Oersted) susceptible de modifier la fréquence des ondes de spin. Nous montrons que l'on peut séparer cette contribution du décalage de fréquence associé à l'effet Doppler en combinant des mesures effectuées pour les deux polarités du vecteur d'onde des ondes de spin, du champ magnétique extérieur et du courant. En utilisant l'expression du couple adiabatique de transfert de spin, nous pouvons extraire du décalage Doppler mesuré le degré de la polarisation en spin du courant. En répétant cette mesure pour des échantillons réalisés à partir de films d'épaisseurs différentes, nous obtenons la dépendance en épaisseur du degré de polarisation en spin représentée sur la figure C.2. On constate clairement que la polarisation en spin diminue quand l'épaisseur diminue. Ces résultats sont discutés dans le cadre du modèle à deux courants. Pour en rendre compte, nous pensons qu'il est nécessaire d'introduire une contribution significative liée à des diffusions par les surfaces avec renversement du spin.

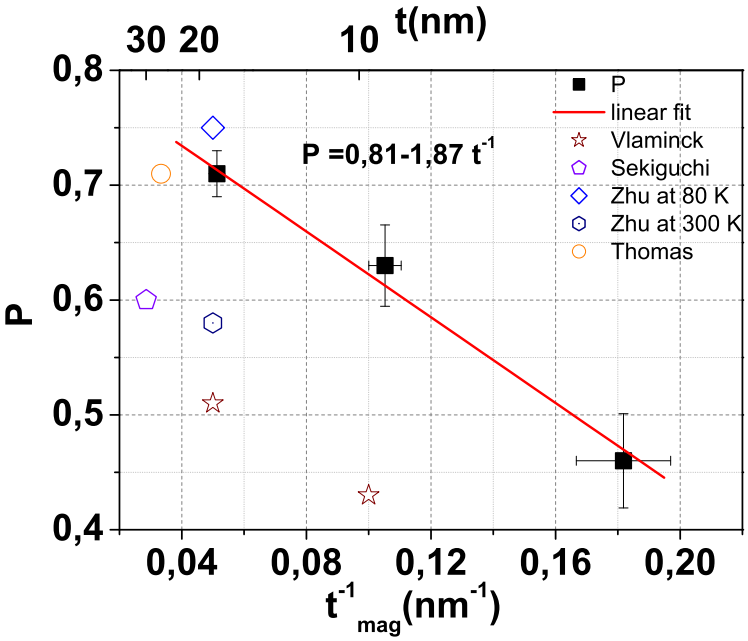

Figure C.2: Variation du degré de polarisation en spin du courant électrique en fonction de l'épaisseur de permalloy.

Conclusion

Ce travail a abordé la question de la variation du degré de polarisation en spin du courant électrique en fonction de l'épaisseur. Il est donc d'un intérêt direct pour une compréhension fondamentale de l'effet des surfaces sur le transport polarisé en spin. En outre, les résultats de cette étude pourraient être utiles pour les développements technologiques.

Premièrement, certains dispositifs fondés sur le transfert de spin, tels que les "racetrack memories" utilisent de très minces nanopistes métalliques [86]. Pour optimiser ces dispositifs, il est nécessaire de comprendre le degré de polarisation en spin du courant électrique (P), le coefficient adiabatique du couple de transfert de spin (β) et le paramètre d'amortissement de Gilbert (α). Notre étude montre l'importance de l'effet de taille (diffusion électronique par les surfaces) pour P et α. Des mesures de propagation d' ondes de spin sous courant électrique pourraient également être utilisées pour extraire β [92]. Deuxièmement, l'étude de la propagation des ondes de spin est cruciale pour le développement de circuits logiques utilisant des ondes de spin ("magnonique"[45, 58, 83]). Notre étude montre comment les surface peuvent influencer ces caractéristiques de propagation. Elle montre également les puissances et les limitations des mesures inductives de propagation d'ondes de spin sous la forme utilisée jusqu'à présent.

Bibliography

[1] F. J. Albert, N. C. Emley, E. B. Myers, D. C. Ralph, and R. A. Buhrman, *Quantitative study of magnetization reversal by spin-polarized current in magnetic multilayer nanopillars*, Phys. Rev. Lett., 89 (2002), p. 226802.

[2] P. Amiri, B. Rejaei, M. Vroubel, and Y. Zhuang, *Nonreciprocal spin wave spectroscopy of thin $nife$ stripes*, Appl. Phys. Lett., 91 (2007), p. 062502.

[3] R. Arias and D. Mills, *Extrinsic contributions to the ferromagnetic resonance response of ultrathin films*, Phys. Rev. B, 60 (1999), pp. No.10, 7395.

[4] N. W. Ashcroft and N. Mermin, *Solid state Physics*, Saunders College Publishing, 1976.

[5] M. N. Baibich, J. M. Broto, A. Fert, F. Nguyen Van Dau, F. Petroff, P. Eitenne, G. Creuzet, A. Friederich, and J. Chazelas, *Giant magnetoresistance of (001)fe/(001)cr magnetic superlattices*, Phys. Rev. Lett., 61 (1988), p. 2472.

[6] M. Bailleul, *Propagation et confinement d'ondes de spin dans les microstructures magnétiques*, Thèse de doctorat de l'Ecole Polytechnique, 2002.

[7] M. Bailleul, D. Olligs, and C. Fermon, *Propagating spin wave spectroscopy in a permalloy film: A quantitative analysis*, Appl. Phys. Lett., 83 (2003), pp. No. 5, 972.

[8] M. Bailleul, D. Olligs, C. Fermon, and S. O. Demokritov, *Spin waves propagation and confinement in conducting films at the micrometer scale*, Europhys. Lett., 56 (2001), pp. 741–747.

[9] J. Banhart, H. Ebert, and A. Vernes, *Applicability of the two-current model for systems with strongly spin dependent disorder*, Phys. Rev. B, 56 (1997), p. 10165.

[10] D. Bastian and B. E., *Damping of ferromagnetic resonance in ni-fe alloys*, Phys. Status Solidi, 35 (1976), p. 113.

[11] Y. B. Bazaliy, B. Jones, and S.-C. Zhang, *Modification of the landau-lifshitz equation in the presence of a spin-polarized current in*

colossal- and giant-magnetoresistive materials, Phys. Rev. B, 57 (1998), p. R3213.

[12] L. Berger, *A simple theory of spin-wave relaxation in ferromagnetic metals*, J. Phys. Chem. Solids, 38 (1977), pp. 1321–1326.

[13] ——, *Emission of spin waves by a magnetic multilayer traversed by a current*, Phys. Rev. B, 54 (1996), p. 9353.

[14] ——, *Spin relaxation in metallic ferromagnets*, Phys. Rev. B, 83 (2011), p. 054410.

[15] S. M. Bhagat and P. Lubitz, *Temperature variation of ferromagnetic relaxation in the 3d transition metals*, Phys. Rev. B, 10 (1974), pp. No.1, 179.

[16] S. Blundell, *Magnetism in Condensed Matter*, Oxford university press, 2001.

[17] W. L. Bongianni, *Magnetostatic propagation in a dielectric layered structure*, J. Appl. Phys., 43 (1972), p. 2541.

[18] L. K. Brundle and N. J. Freedman, *Magnetostatic surface waves on a y.i.g. slab*, Electron. Lett., 4 (1968), pp. 132–134.

[19] I. Campbell and A. Fert, *Transport properties of ferromagnets, in ferromagnetic materials*, vol.3 (1982). E.P. Wohlfarth, Ed.

[20] C. Chappert, A. Fert, and F. Nguyen Van Dau, *The emergence of spin electronics in data storage*, Nature, 6 (2007), p. 813.

[21] J. S. Chawla, X. Y. Zhang, and D. Gall, *Epitaxial tin(001) wetting layer for growth of thin single-crystal cu(001)*, J. Appl. Phys., 110 (2011), p. 043714.

[22] R. Coehoorn, *Handbook of magnetic materials*, vol. vol. 15, North Holland, 2003. K. H. J. Buschow, Ed.

[23] G. Counil, T. Devolder, J.-V. Kim, P. Crozat, C. Chappert, S. Zoll, and R. Fournel, *Temperature dependences of the resistivity and the ferromagnetic resonance linewidth in permalloy thin films*, IEEE Trans. Mag., 42 (2006), p. 3323.

[24] G. Counil, J. Kim, T. Devolder, C. Chappert, K. Shigeto, and Y. Otani, *Spin wave contributions to the high-frequency magnetic response of thin films obtained with inductive methods*, J. Appl. Phys., 95 (2004), pp. No. 10, 5646.

[25] M. Covington, T. Crawford, and G. J. Parker, *Time-resolved measurement of propagating spinwaves in ferromagnetic thin films*, Phys. Rev. Lett., 89 (2002), p. 273202.

[26] R. Damon and J. Eshbach, *Surface magnetostatic modes and surface spin waves*, Phys. Rev., 118 (1960), pp. No.5, 1208.

[27] V. Demidov, S. Demokritov, K. Rott, P. Krzysteczko, and G. Reiss, *Self-focusing of spin waves in permalloy microstripes*, Appl. Phys. Lett., 91 (2007), p. 252504.

[28] V. Demidov, M. P. Kostylev, K. Rott, P. Krzysteczko, G. Reiss, and S. Demokritov, *Excitation of microwaveguide modes by a stripe antenna*, Appl. Phys. Lett., 95 (2009), p. 112509.

[29] J. e. a. Dubowik, *Temperature dependence of ferromagnetic resonance in permalloy/nio exchange-biased films*, Eur. Phys. J. B, 45 (2005), p. 283.

[30] J. Durand and F. Gautier, J. Phys. Chem. Solids, 31 (1970), pp. 2773–2787.

[31] C. Durkan and M. Welland, *Size effects in the electrical resistivity of polycrystalline nanowires*, Phys. Rev. B, 61 (1998), pp. No.20, 14215–14218.

[32] J. Fernández-Rossier, M. Braun, A. S. Núñez, and A. H. MacDonald, *Influence of a uniform current on collective magnetization dynamics in a ferromagnetic metal*, Phys. Rev. B, 69 (2004), p. 174412.

[33] A. Fert, *Two current conduction in ferromagnetic metals and spin wave-electron collisions nickel and iron based alloys*, J.Phys C: Solid state physics, 2 (1969), p. 1784.

[34] A. Fert and I. Campbell, *Electrical resistivity of ferromagnetic nickel and iron based alloys*, J. Phys. Chem. Solids, 6 (1976), pp. No. 5, 849–871.

[35] M. R. Fitzsimmons, T. J. Silva, and T. M. Crawford1, *Surface oxidation of permalloy thin films*, Phys. Rev. B, 73 (2006), p. 014420.

[36] F. GAUTIER. private communication.

[37] A. Ghosh, S. Auffret, U. Ebels, and W. E. Bailey, *Penetration depth of transverse spin current in ultrathin ferromagnets*, Phys. Rev. Lett., 109 (2012), pp. No. 10, 127202.

[38] T. L. Gilbert, *A phenomenological theory of damping in ferromagnetic materials*, IEEE Trans. Mag., 40 (2004), pp. No.6, 3443.

[39] K. Gilmore, Y. Idzerda, and M. Stiles, *Spin-orbit precession damping in transition metal ferromagnets*, J. Appl. Phys., 103 (2008), p. 07D303.

[40] e. a. Gloanec, M., *Dynamical effect in measurement of the exchange-bias field: A consequence of the slow-relaxer mechanism*, Phys. Rev. B, 80 (2009), p. 220404(R).

[41] P. Grünberg, R. Schreiber, Y. Pang, M. B. Brodsky, and H. Sowers, *Layered magnetic structures: Evidence for antiferromagnetic coupling of fe layers across cr interlayers*, Phys. Rev. Lett., 57 (1986), p. 2442.

[42] A. Gurevich and G. Melkov, *Magnetization Oscillations and Waves*, CRC Press, 1996.

[43] B. A. Gurney, V. S. Speriosu, J. P. Nozieres, H. Lefakis, W. D. R., and O. U. Need, *Direct measurement of spin-dependent conduction-electron mean free paths in ferromagnetic metals*, Phys. Rev. Lett., 71 (1993), pp. No.24, 4023.

[44] B. Heinrich, D. Fraitova, and V. Kambersky, *The influence of s-d exchange on relaxation of magnons in metals*, Phys. Status Solidi, 23 (1967), p. 501.

[45] R. Hertel, W. Wulfhekel, and J. Kirschner, *Domain-wall induced phase shifts in spinwaves*, Phys. Rev. Lett., 93 (2004), p. 257202.

[46] H. Hoffmann and J. Vancea, *Critical assessment of thickness-dependent conductivity of thin metals films*, Thin Solid Films, 85 (1981), pp. 147–167.

[47] P. Holody, W. C. Chiang, R. Loloee, J. Bass, W. P. Pratt, and P. A. Schroeder, *Giant magnetoresistance of copper/permalloy multilayers*, Phys. Rev. B, 58 (1998), pp. 12230–12236.

[48] D. Houssameddine, U. Ebels, B. Delaet, B. Rodmacq, I. Firastrau, M. Ponthenier, F.and Brunet, C. Thirion, J.-P. Michel, L. Prejbeanu-Buda, M.-C. Cyrille, O. Redon, and B. Dieny, *Spin-torque oscillator using a perpendicular polarizer and a planar free layer*, Nature, 6 (2007), p. 447.

[49] A. Hubert and S. R., *Magnetic domains, The analysis of magntic microstructure*, Springer, 1998.

[50] H. Hurdequint, *Fmr studies of ultrathin permalloy layers sandwiched by al_2o_3*, J. Magn. Magn. Mater., 242 (2002).

[51] ——, *Fmr studies of single permalloy layers sandwiched by au*, J. Magn. Magn. Mater., 310 (2007), pp. 2061–2063.

[52] S. Ingvarsson, *Role of electron scattering in the magnetization relaxation of thin $ni_{81}fe_{19}$ films*, Phys. Rev. B, 66 (2002), p. 214416.

[53] U. Jacob, J. Vancea, and H. Hoffmann, *A new method for determining the electronic mean free path in polycrystalline metals*, J. Phys.: Condens. Matter, 74 (1980), pp. 9867–9873.

[54] B. Kalinikos, *Excitation of propagating spin waves in ferromagnetic films*, (1980).

[55] S. A. Kalinikos, B.A., *Theory of dipole-exchange spin wave spectrum for ferromagnetic films with mixed exchange boundary conditions*, Solid State Phys., 19 (1986), pp. 7013–7033.

[56] V. Kambersky, *On the landau-lifshitz relaxation in ferromagnetic metals*, Can. J. Phys., 48 (1970), p. 2906.

[57] J. Katine, F. J. Albert, R. A. Buhrman, E. B. Myers, and D. C. Ralph, *Current-driven magnetization reversal and spin-wave excitations in co/cu/co pillars*, Phys. Rev. Lett., 84 (2000), p. 3149.

[58] A. Khitun, M. Bao, and K. L. Wang, *Magnonic logic circuits*, J. Phys. D: Appl. Phys., 43 (2010), p. 264005.

[59] M. Kläui, P.-O. Jubert, R. Allenspach, A. Bischof, J. A. C. Bland, G. Faini, U. Rüdiger, C. A. F. Vaz, L. Vila, and C. Vouille, *Direct observation of domain-wall configurations transformed by spin currents*, Phys. Rev. Lett., 95 (2005), p. 026601.

[60] V. Koreman and R. Prange, *Anomalous damping of spin waves in magnetic materials*, Phys. Rev. B, 6 (1970), pp. No.7, 2769.

[61] M. P. Kostylev, *Asymmetry of modal profiles of dipole-exchange spin waves in thin high-magnetic moment metallic ferromagnetic films*, (2012), p. 1209.4153.

[62] P. Lederer and D. Mills, *Possible experimental test of the band theory of magnetism*, Phys. Rev., 148 (1966), p. 542.

[63] B. Loegel and F. Gautier, *Origine de la resistivite dans le cobalt et ses alliages dilues*, J. Phys. Chem. Solids, 32 (1971), pp. 2723–2735.

[64] P. Lubitz, J. Krebs, M. Miller, and S. Cheng, *Temperature dependence of the ferromagnetic resonance as induced by nio pinning layers*, J. Appl. Phys., 83 (1998), p. 6819.

[65] P. Lubitz, M. Rubinstein, M. Miller, and S. Cheng, *Frequency and temperature dependence of the ferromagnetic linewidth in exchange biased permalloy*, J. Appl. Phys., 89 (2001), p. 6901.

[66] S. Mangin, D. Ravelosona, J. Katine, M. J. Carey, B. D. Terris, and E. E. Fullerton, *Current-induced magnetization reversal in nanopillars with perpendicular anisotropy*, Nature Materials, 5 (2006), p. 210.

[67] A. Mayadas, J. Janak, and A. Gangulee, *Resistivity of permalloy thin films*, J. Appl. Phys., 45 (1974), p. 2780.

[68] A. Mayadas and M. Shatzkes, *Electrical-resistivity model for polycrystalline films: the case of arbitrary reflection at external surfaces*, Phys. Rev. B, 1 (1970), pp. No. 4, 1382–1389.

[69] T. R. MCGUIRE and R. I. POTTER, *Anisotropic magnetoresistance in ferromagnetic 3d alloys*, IEEE Trans. Mag., 4 (1975), p. 1018.

[70] R. McMichael, *A mean-field model of extrinsic line broadening in ferromagnetic resonance*, J. Appl. Phys., 103 (2008), p. 07B114.

[71] R. McMichael, D. Twisselmann, and A. Kunz, *Localized ferromagnetic resonance in inhomomegeneous thin films*, Phys. Rev. Lett., 90 (2003), p. 227601.

[72] G. Meier, M. Bolte, R. Eiselt, B. Krüger, D.-H. Kim, and P. Fischer, *Direct imaging of stochastic domain-wall motion driven by nanosecond current pulses*, Phys. Rev. Lett., 98 (2007), p. 187202.

[73] G. Melkov, V. Vasyuchka, V. Lazovskiy, V. S. Tiberkevich, and A. Slavin, *Wave front reversal with frequency conversion in a nonreciprocal medium*, Appl. Phys. Lett., 89 (2006), p. 252510.

[74] I. Mertig, R. Zeller, and P. H. Dederichs, *Ab initio calculations of residual resistivities for dilute ni alloys*, Phys. Rev. B, 47 (1993), p. 16178.

[75] P. Mijnarends, S. Sahrakorpi, and M. Lindroos, *Angle-resolved photoemission spectra, electronic structure, and spin-dependent scattering in $ni_{1-x}fe_x$ permalloys*, Phys. Rev. B, 65 (2002), p. 075106.

[76] D. L. Mills, *SUrface spin waves on magnetic crystals*, Elsevier Science Publishers.

[77] E. Mitchell, *Compositional and thickness dependence of the ferromagnetic anisotropy in resistance of ironnickel films*, J. Appl. Phys., 35 (1974), p. 2604.

[78] S. Mizukami, Y. Ando, and T. Miyazaki, *Ferromagnetic resonance linewidth for nm/80nife/nm "lms (nm"cu, ta, pd and pt)*, J. Magn. Magn. Mater., 226 (2001).

[79] N. Mott, *The electrical conductivity of transition metals*, Proc. R. Soc., 153 (1936), pp. 699–717.

[80] E. Myers, D. Ralph, J. Katine, R. Louie, and R. A. Buhrman, *Current-induced switching of domains in magnetic multilayer devices*, Science, 285 (1999), pp. 867–870.

[81] G. Nahrwold, J. M. Scholtyssek, S. Motl-Ziegler, O. Albrecht, U. Merkt, and G. Meier, *Structural, magnetic, and transport properties of permalloy for spintronic experiments*, J. Appl. Phys., 108 (2010), p. 013907.

[82] S. Neusser, G. Duerr, H. Bauer, S. Tacchi, M. Madami, G. Woltersdorf, G. Gubbiotti, C. H. Back, and D. Grundler, *Anisotropic propagation and damping of spinwaves in a nanopatterned antidot lattice*, Phys. Rev. Lett., 105 (2010), p. 067208.

[83] S. Neusser and D. Grundler, *Magnonics: Spin waves on the nanoscale*, ADVANCED Materials, 21 (2009), pp. 2927–2932.

[84] J. P. Nibarger, R. Lopusnik, and S. T. J. Celinski, Z., *Variation of magnetization and the landeť g factor with thickness in niŨfe films*, Appl. Phys. Lett., 8 (2003), pp. No.1, 93.

[85] S. S. P. Parkin, *Origin of enhanced magnetoresistance of magnetic multilayers: Spin-dependent scattering from magnetic interface states*, Phys. Rev. Lett., 71 (1993), pp. No.10, 1641.

[86] S. S. P. Parkin, M. Hayashi, and L. Thomas, *Magnetic domain-wall racetrack memory*, Science, 320 (2008), p. 19.

[87] C. PATTON and C. WILTS, *Temperature dependence of the ferromagnetic resonance linewidth in thin ni-fe films*, J. Appl. Phys., 38 (1967), p. 3537.

[88] G. Rado and J. Wertmann, *Spin-wave resonance in a ferromagnetic metal*, J. Phys. Chem. Solids, 11 (1959), pp. No.3/4, 315.

[89] E. Rantschlar and et al., *Surface anisotropy of permalloy in nm/ nife/nm multilayers*, J. Appl. Phys., 97 (2005), p. 10J113.

[90] B. Raquet, M. Viret, E. Sondergard, O. Cespedes, and R. Mamy, *Electron-magnon scattering and magnetic resistivity in 3d ferromagnets*, Phys. Rev. B, 66 (2002), p. 024433.

[91] review series on spin transfer torque, (2008).

[92] K. Sekiguchi, Y. Keisuke, S. Seo, K. Lee, D. Chiba, K. K., and T. Ono, *Time-domain measurement of current-induced spinwave dynamics*, Phys. Rev. Lett., 108 (2012), p. 017203.

[93] K. Sekiguchi, K. Vader, T.N. znd Yamada, S. Fukami, N. Ishiwata, S. M. Seo, S. W. Lee, K. J. Lee, and T. Ono, *Attenuation of propagating spin wave induced by layered nanostructures*, Appl. Phys. Lett., 100 (2012), p. 132411.

[94] K. Sekiguchi, K. Yamada, S. M. Seo, K. J. Lee, D. Chiba, and T. Kobayashi, K.and Ono, *Nonreciprocal emission of spin-wave packet in feni film*, Appl. Phys. Lett., 97 (2010), p. 022508.

[95] S. Seo, K. Lee, and T. Yang, H.and Ono, *Current-induced control of spin-wave attenuation*, Phys. Rev. Lett., 102 (2009), p. 147202.

[96] T. J. Silva, C. S. Lee, T. M. Crawford, and C. T. Rogers, *Inductive measurement of ultrafast magnetization dynamics in thin-film permalloy*, J. Appl. Phys., 85 (1999), pp. No. 11, 7849.

[97] J. Slonczewski, *Current-driven excitation of magnetic multilayers*, J. Magn. Magn. Mater., 159 (1996), pp. L1–L7.

[98] E. Sondheimer, *The mean free path of electrons in metals*, ADVANCES IN PHYSICS, 1 (1952), pp. No. 1, 1–42.

[99] R. F. Soohoo, *General exchange boundary condition and surface anisotropy energy in a ferromagnet*, Phys. Rev., 131 (1962), pp. No.2, 594.

[100] D. Stancil and A. Prabhakar, *Spin waves theory and applications*, Springer, 2009.

[101] A. Starikov, P. Kelly, A. Bratass, Y. Tserkovnyak, and G. Bauer, *Unified first-principles study of gilbert damping, spin-flip diffusion, and resistivity in transition metal alloys*, Phys. Rev. Lett., 105 (2010), p. 236601.

[102] S. D. Steenwyk, S. Y. Hsu, R. Loloee, J. Bass, and W. P. J. Pratt, *Perpendicular-current exchange-biased spin-valve evidence for a short spin-diffusion lenght in permalloy*, J. Magn. Magn. Mater., 170 (1997), pp. L1–L6.

[103] T. T. Schneider, A. A. Serga, T. Neumann, B. Hillebrands, and M. P. Kostylev, *Phase reciprocity of spin-wave excitation by a microstrip antenna*, Phys. Rev. B, 77 (2008), p. 214411.

[104] A. Thiaville, Y. Nakatani, J. Miltat, and N. Vernier, *Domain wall motion by spin-polarized current: a micromagnetic study*, J. Appl. Phys., 95 (2004), p. 7049.

[105] A. Thiaville, Y. L. Nakatani, J. Miltat, and Y. Suzuki, *Micromagnetic understanding of current-driven domain wall motion in patterned nanowires*, Europhys. Lett., 69 (2005), pp. 990–996.

[106] R. Thomas, M. Zhu, C. L. Dennis, and R. D. McMichael, *Impact of gd dopants on current polarization and the resulting effect on spin transfer velocity in permalloy wires*, J. Appl. Phys., 110 (20110), p. 033902.

[107] M. Tsoi, A. G. M. Jansen, J. Bass, W.-C. Chiang, M. Seck, V. Tsoi, and P. Wyder, *Excitation of a magnetic multilayer by an electric current*, Phys. Rev. Lett., 80 (1998), p. 4281.

[108] L. J. Van der Pauw, *A method of measuring specific resistivity and hall effect of discs of arbitrary shape*, Philips Research Reports, 13 (1958), pp. No. 1, 1–9.

[109] J. Vancea, H. Hoffmann, and K. Kastner, *Mean free path and effective density of conduction electrons in polycrystalline metals films*, Thin Solid Films, 121 (1984), pp. 201–216.

[110] V. VLaminck, *Décalage Doppler d'onde de spin induit par un courant électrique*, Thèse de doctorat de l'Université Louis Pasteur, 2008.

[111] V. Vlaminck and M. Bailleul, *Current-induced spin wave doppler shift*, Science, 322 (2008), pp. 410–413.

[112] ——, *Spin-wave transduction at the submicrometer scale: Experiment and modeling*, Phys. Rev. B, 81 (2010), p. 014425.

[113] K. Vogt, H. Schultheiss, S. Hermsdoerfer, P. Pirro, A. A. Serga, and B. Hillebrands, *All-optical detection of phase fronts of propagating spin waves in a $ni_{81}fe_{19}$ microstripe*, Appl. Phys. Lett., 95 (2009), p. 182508.

[114] G. Woltersdorf, M. Kiessling, J.-U. Meyer, G. andd Thiele, and C. Back, *Damping by slow relaxing rare earth impurities in $ni_{80}fe_{20}$*, Phys. Rev. Lett., 102 (2009), p. 257602.

[115] J. XIAO, M. D. STILES, and A. ZANGWILL, *Spin-transfer torque for continuously variable magnetization*, Phys. Rev. B, 73 (2006), p. 054428.

[116] A. Yamaguchi, T. Ono, S. Nasu, K. Miyake, K. Mibu, and T. Shinjo, *Real-space observation of current-driven domain wall motion in submicron magnetic wires*, Phys. Rev. Lett., 92 (2004), p. 077205.

[117] S. Zhang and Z. Li, *Roles of nonequilibrium conduction electrons on the magnetization dynamics of ferromagnets*, Phys. Rev. Lett., 93 (2004), p. 127204.

[118] M. Zhu, C. L. Dennis, and R. D. McMichael, *Temperature dependence of magnetization drift velocity and current polarization in ni80fe20 by spin-wave doppler measurements*, Phys. Rev. B(Rapid Comm.), 81 (2010), p. 140407(R).

[119] M. Zhu, B. D. Soe, R. D. McMichael, M. Carey, S. Maat, and J. Childress, *Enhanced magnetization drift velocity and current polarization in* $(cofe)_{1-x}ge_x$ *alloys*, Appl. Phys. Lett., 98 (2011), p. 072510.

[120] J. M. Ziman, *Electrons and Phonons the theory of transport phenomena in solids*, OXFORD AT THE CLARENDON PRESS, 1960.

Résumé

Dans cette thèse, nous proposons d'explorer la relation entre transport électronique et dynamique d'aimantation afin de mieux comprendre certaines propriétés des films minces de métaux ferromagnétiques. Afin d'extraire l'influence de la diffusion des électrons par les surfaces sur les résistivités dépendantes du spin, des séries d'épaisseur de films de permalloy ($Ni_{80}Fe_{20}$) ont été déposées et étudiées. En plus de mesures électriques et magnétiques conventionnelles, nous avons réalisé une étude détaillée de la propagation des ondes de spin dans ces films. La technique du décalage Doppler d'ondes de spin induit par un courant électrique a été utilisée pour extraire le degré de polarisation en spin du courant électrique. Nous avons observé que ce degré de polarisation décroît lorsque l'épaisseur du film décroît, ce qui suggère que les surfaces contribuent aux résistivités dépendantes du spin et qu'elles ont tendance à dépolariser le courant électrique.

Mots-clés : transport polarisé en spin, diffusion des électrons par les surfaces, dynamique de spin, ondes de spin

Abstract

In this thesis, the interplay between electron transport and magnetization dynamics is explored in order to access to fundamental properties of ferromagnetic metal thin films. With the aim of extracting the influence of the electron surface scattering on the spin-dependent resistivities, thickness series of permalloy ($Ni_{80}Fe_{20}$) films were grown and studied. In addition to standard electrical and magnetic measurements, a detailed study of the propagation of spin waves along these films was performed. Resorting to the current-induced spin-wave Doppler shift technique, the degree of spin-polarization of the electrical current was extracted. This degree of spin-polarization was found to decrease when the film thickness decreases, which suggests that the film surfaces contribute to the spin dependent resistivities and tend to depolarize the electrical current.

Keywords: spin polarized transport, surface electron scattering, spin dynamics, spin wave